THE UNIVERSITY OF CHICAGO

STRUCTURE AND FUNCTION OF ASTROGLIA IN LARVAL ZEBRAFISH

A DISSERTATION SUBMITTED TO

THE FACULTY OF THE DIVISION OF THE BIOLOGICAL SCIENCES

AND THE PRITZKER SCHOOL OF MEDICINE

IN CANDIDACY FOR THE DEGREE OF

DOCTOR OF PHILOSOPHY

BIOLOGY

BY

DAVIS VANN BENNETT

CHICAGO, ILLINOIS

AUGUST 2019

Table of Contents

List of figures

List of tables

Acknowledgements

Several individuals set the groundwork for all the work presented in this thesis: Chao-Tsung Yang created the lab's first GFAP-transgenic fish; Nikita Vladimirov designed, assembled, and maintained the light sheet microscope that I used to acquire the first functional imaging data of fish astroglia, and Jeremy Freeman built the software tools for analyzing these datasets at scale. Others directly contributed data shown in this thesis, in particular Chapter 3, which was an extensive collaboration. For that project, Yu Mu designed and executed the vast majority of the imaging and behavioral experiments; Mika Rubinov contributed essential image processing and functional imaging analyses; Sujatha Narayan created and characterized novel transgenic animals, and performed many immunohistochemistry experiments; Andy Lemire, Lihua Wang, and Loren Looger contributed RNA-sequencing data; Paul Tillberg, Amy Hu, and Damien Alcor performed expansion microscopy. Chapter 4 contains zebrafish imaging data provided by Yu Mu, and *Drosophila* imaging data provided by Bill Lemon. I benefited from technical assistance and advice from a number of people, chiefly Nikita Vladimirov, Takashi Kawashima, Minoru Koyama, Igor Negrashov, Jason Wittenbach, John Kirkham, Burkhard Hoekendorf, Raghav Chetri, among others. I am grateful for the guidance I received from my mentors at Janelia: my advisor, Misha Ahrens, as well as Vivek Jayaraman, Jeremy Freeman, Philipp Keller, and Ulrike Heberlein. I am also grateful to my committee at UChicago: Melina Hale, Dan Margoliash, and Brian Popko. Lastly, I thank my partner Hannah Haberkern for her enduring companionship.

Chapter 1: General Introduction

Introduction

The early neuroanatomist Rudolf Virchow was searching for connective tissue in the vertebrate brain when he observed glial cells in histological sections from the central and peripheral nervous system across many species. He postulated that these cells provide static structural support to nervous tissue (Virchow 1856). Believing that the cells he saw “glued” the brain together, Virchow termed them “neuroglia”, and the name stuck. Other neuroanatomists soon postulated more functions for glia: Camillo Golgi observed that glial cells often contact vasculature, while neurons do not, which led him to suggest that glia convey circulating metabolites to hungry neurons; Santiago Ramón y Cajal suggested that glia may electrically insulate neurons; Wilhelm His suggested that radial glial fibers guide the migration of nascent neurons; Ernesto Lugaro proposed that glia regulate the synaptic space (reviewed in Somjen 1988).

Subsequent research confirmed and refined these pathologists’ educated guesses; we have since cataloged many different subtypes of glial cells and assigned to them a range of functions, many of which were accurately intimated by the aforementioned anatomists: during nervous system development, glia are the source of many neurons (Kriegstein and Alvarez-Buylla 2009), and glia enable proper localization of those neurons (Rakic 1972); additionally, glia myelinate axons and enable ordered synapse formation (Tasdemir-Yilmaz and Freeman 2014). After nervous system development reaches steady-state, glia provide metabolic support for neurons (Weber and Barros 2015) and facilitate neuronal function, e.g. by scavenging neurotransmitters around

synapses (Hertz and Zielke 2004) and maintaining ionic homeostasis of the extracellular space (Simard and Nedergaard 2004). Additionally, many glia are excitable cells, much like neurons (and this could not be predicted from histological sections); these glia express receptors for neurotransmitters (Cornell-Bell et al. 1990), and there is mounting evidence that excitable glial cells directly influence neuronal activity on a timescale relevant for sensory processing and behavior (Nedergaard 1994; Parpura et al. 1994; Martín et al. 2015; Morquette et al. 2015; Ma et al. 2016).

Evidence for fast glia-neuron interactions was particularly surprising because *de facto* neuroscience dogma was (and in many circles, still is) that information processing in the brain is exclusively done by neurons. Thus, the discovery of another class of excitable cells in the brain could broaden the scope of neuroscience. But the vast majority of the studies of glia-neuron interaction, and glial excitability in general, have focused on astrocytes, a type of glial cell found abundantly in mice, and exclusively in mammals. So, it is not clear how the evidence from studies of excitable glia in mice can generalize to birds, fish, reptiles, etc. It is of course *possible* that computation in the mammalian nervous system works with a broader cellular palette than that of non-mammalian vertebrates, but it may also be the case that the niche filled by mammalian astrocytes is filled by hitherto-unobserved excitable glia in non-mammalian vertebrates. If the second possibility is true, then functional coupling between excitable glia and neurons may be fundamental to the vertebrate nervous system, and thus it may be possible to productively study this interaction in non-mammalian model organisms. This was our hope when we began studying glia in larval zebrafish.

In this thesis, I present a set of interlocking biological and technological developments: in Chapter 2, I will argue that a class of glial cells in the larval zebrafish is structurally and functionally homologous to astrocytes, which have been intensely-studied in mammals. This finding is of interest because the larval zebrafish is a model organism that enables a uniquely expansive set of high-throughput, high-resolution experiments for probing the vertebrate nervous system, but these advantages have hitherto been leveraged exclusively for studying neuronal cells, with no consideration for glia. Chapter 3 presents evidence that zebrafish glia can participate in behaviorally relevant computation, which builds on and demonstrates the arguments of Chapter 2.

The biological data I present in Chapters 2 and 3 would not be possible without an ecosystem of tools for gathering and analyzing functional imaging data via light microscopy. Chapter 4 presents a sorely-needed addition to the functional imaging toolkit: a simple technique for vastly accelerating data analysis of large functional imaging datasets.

This introductory chapter will introduce key concepts and experimental techniques that will be relevant for the following chapters. First, I will present a reconceptualization of the nervous system that naturally generates the presupposition that glia are fundamental elements of complex nervous systems. Then, in light of this theoretical framework, I will review extant facts about excitable glial cells with an emphasis on their interactions with neurons. Finally, I will introduce larval zebrafish as a model for behavioral neuroscience, and summarily discuss many of the experimental techniques which will be used in subsequent chapters.

A theory of glia-neuron interactions

To the typical systems neuroscientist, i.e. someone concerned with how neurons signal to each other, it is not at first obvious why glial cells would be of interest. Neurons signal to each other with spikes across synapses; this picture seems complete. But how do neurons work? A single spiking neuron propagates signals by leveraging an electrochemical gradient across its membrane; signals between neurons are typically transmitted by release and capture of neurotransmitters in the extracellular space. Neither action potential generation nor synaptic release are sustainable long-term without dynamical processes that maintain homeostasis. Despite their utter reliance on the state of the extracellular space for signaling, neurons cannot effectively regulate this domain without sacrificing their signaling ability. Accordingly, I suggest that any complex nervous system (i.e., a nervous system composed of spiking neurons in close proximity) needs regulation of the extracellular space to obtain optimal signal processing by neurons, and that glia provide this regulation in vertebrates. I argue for this claim via the following thought experiment: consider a hypothetical “nervous system” of two neurons in close apposition inside a compartment. Suppose also that these two neurons are functionally separable, e.g. they each provide excitatory input to different muscle groups, or they respond to visual inputs to distinct regions of the retina. If the first neuron fires a barrage of spikes, the electrochemical state of the extracellular space will be altered (e.g., the extracellular potassium concentration increases, extracellular calcium decreases, etc.), which in turn affects the excitability of the second neuron, and thus its ability to engage in signal processing. By sharing the extracellular space, the

two neurons cannot signal independently, and this problem becomes more severe if more neurons were added to the compartment. This crosstalk problem is inherent to the biophysics of action potential generation. But it can be solved if the neurons are isolated from each other by a non-spiking cell that can sense and regulate the extracellular space, i.e. a paradigmatic glial cell. With such a cell added to our model nervous system, the second neuron is isolated from the externalities of the first neuron's spiking, and the two neurons can engage in signal processing independently and efficiently, albeit at the expense of a more complicated nervous system—we now have two cell types instead of one.

Perhaps the clearest known instantiation of this thought experiment is the critical role for glial cells in potassium homeostasis. Neuronal action potentials cause potassium to accumulate in the extracellular space at concentrations that can affect a neuron's resting membrane potential (Huxley and Stämpfli 1951; Krnjević and Morris 1972); this excess extracellular potassium is rapidly cleared by glia (Orkand et al. 2017), thereby restoring the extracellular space to its baseline state. Given this phenomenon, we can be judicious in how we apply teleological terms to it. Should we label glial control of the extracellular space as provision of "support" for neurons? This is how glial function is typically summarized in the broader neuroscience literature (e.g., glia as "support cells"). But does electrochemically isolating a neuron from its neighbors really "support" that specific neuron? Does facilitating synaptic transmission "support" a neuron? The neuron-centric view here feels strained. It seems more apt to say that glial regulation of extracellular space chiefly supports *neuronal signaling*, or nervous system function as a

whole (and this is the same thing that neuronal action potentials support!); thus, interaction between glia and neurons is cooperative, toward a common goal. I believe this is more than a semantic quibble—as will be discussed later in the thesis, glia have been observed directly modulating neuronal activity, either by altering the extracellular space to push neuronal dynamics into a different state (Morquette et al. 2015), or by releasing a ligand for neuron-bound receptors (Ma et al. 2016). These results are difficult to understand if we believe that glia exist to support neurons. But if we believe that glia support *nervous system function*, then dynamically altering neuronal activity is entirely consistent with that mandate, and we should expect to find many instances of glial dynamics shaping neuronal signaling. Indeed, if our interest is the understanding of brain function, then we should be *motivated* to search for such glia-neuron interactions.

Radial glia, astrocytes, and "astroglia"

In the following sections I will describe the two major classes of glial cells that are relevant for this thesis, radial glia and astrocytes. These two classes are not entirely disjoint, and the intersection of the classes "astrocyte" and "radial glia" might be larger than their difference. That being said, for the purposes of this introduction, I will discuss these cell types as they are presented in the literature, i.e. as distinct. I will first introduce radial glia, which have a valid claim to the title of "*ur-glia*": radial glia have been found in all vertebrate brains studied so far, they are the first glial cells to appear in vertebrate development, and their morphological and functional properties nearly span the space of traits in which more specialized glia reside. Specifically, radial glia are essential elements of a neurogenic nervous system—radial glia directly produce many

neurons, and they form a spatial coordinate system in nervous tissue that enables newborn neurons to integrate with neural circuits in an orderly manner. After describing these fundamental glial cells, I will describe astrocytes, which are specific to certain brain regions in adult mammals. Unlike radial glia, which have been examined almost exclusively in the context of neurogenesis in the developing nervous system, astrocytes have been intensely studied in the context of how they interface with mature neuronal circuits. Astrocytes are unpolarized cells that fill the peri-neuronal space with ramifying processes rich in receptors and channels that allow these cells to sense and regulate neural activity. My focus on radial glia and astrocytes elides other interesting subtypes of glia, chiefly myelinating glia, which unfortunately I cannot discuss here. I focus on radial glia and astrocytes because this thesis describes glial cells in larval zebrafish that resemble both of those cell types, each of which has been largely studied independently.

Radial glia

Radial glia are the first glial cells in the nervous system and their morphology reflects this—radial glial somata reside at the apical (ventricular) surface, and these cells send processes to the basal (pial) surface of the developing neuroepithelium; at both ventricular and pial boundaries these cells form lamellar processes called endfeet that define the extent of the neuroepithelium (Fig. 1.1A). Radial glia are proliferative, giving rise to many neurons and glia during development of the nervous system (Malatesta et al. 2000; Johnson et al. 2016). Neurons born from radial glia migrate from the ventricular zone by climbing radial glial fibers toward to the pial surface; at the

appropriate distance from the ventricular zone, these neurons detach from glial fibers and integrate into neural circuits (Fig. 1.1B). Radial glia have been intensely studied at the structural level, with an emphasis on how neurons use these cells for migration and differentiation, but calcium imaging studies have revealed that neuronal migration in mouse embryos is modulated by extensive calcium signaling within and between radial glia (Weissman et al. 2004; Rash et al. 2016), which indicates that the role of radial glia in neuronal migration goes beyond providing static scaffolding for migrating neurons. Radial glia are initially abundant in the developing mammalian nervous system, but after neurogenesis these cells are confined to a few specialized neural structures (the retina and cerebellum, and neurogenic niches). But in many non-mammalian organisms such as fish (Adolf et al. 2006), birds (Paton and Nottebohm 1984), and reptiles (Lopez-Garcia et al. 1988), extensive neurogenic potential persists into adulthood, and these animals also retain radial glia into adulthood (Alvarez-Buylla and Nottebohm 1988; Yanes et al. 1990; Kroehne et al. 2011). The ubiquity of radial glial fibers in neurogenic brains suggests that neurogenesis requires, or is at least greatly facilitated by, the presence of radial glia (Costa et al. 2010).

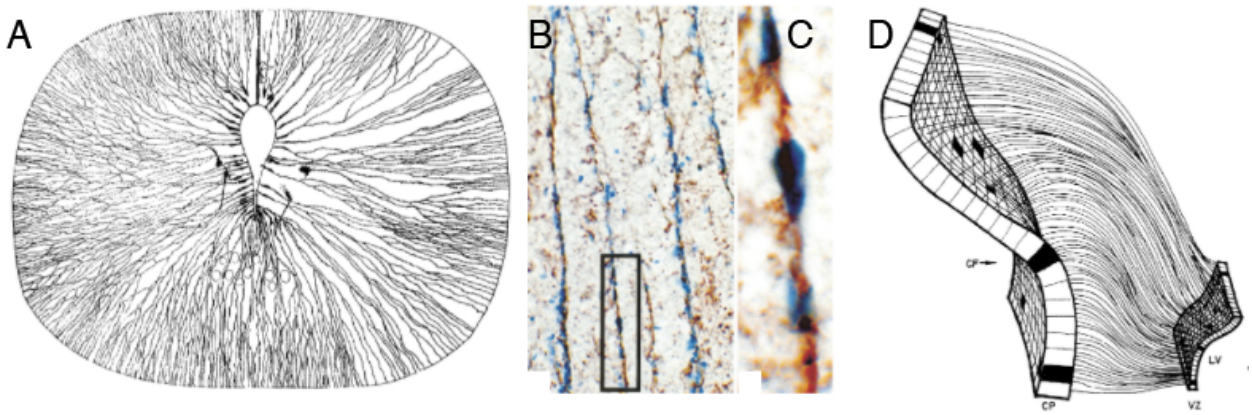

Figure 1.1. The gross morphology of radial glia.
(A) A reproduction of a drawing by Retzius of radial glial fibers from a Golgi-stained section of adult lamprey medulla (modified from Bentivoglio and Mazzarello 1999). In typical fashion, the radial glial somata are near the peri-ventricular space. They send out projections to the pial surface; at both pial and ventricular surfaces, the cells form lamellar endfeet. **(B)** Radial glial fibers immunolabelled against vimentin (brown) and neuronal nuclei with the toluidine blue stain (blue) in the frontal lobe of a human fetus. **(C)** Magnified view of the inset in (B), showing multiple neurons ascending a glial fiber. **(D)** Cartoon of primate cortical development illustrating how radial glial fibers emanating from the ventricular zone (VZ) map in an orderly fashion to the cortical plate (CP).

In addition to endfeet and apical-basal projections that guide neuronal migration, radial glia can form ramifying processes that intermingle with neuronal processes (Fig. 1.2). These glial processes extensively surround neuronal processes and thus give radial glia access to synapses and the broader extracellular space. Besides their morphology, radial glia are distinguished from neuroepithelial cells and neurons by their expression of a variety of proteins, including the intermediate filaments glial fibrillary acidic protein (GFAP) and vimentin (believed to give radial glia increased resistance to mechanical stress); the glutamate transporter GLAST (enabling clearance of perisynaptic glutamate); the enzyme glutamine synthetase (GS) (enabling conversion of glutamate into glutamine); the gap-junction protein connexin 43 (enabling cell-cell communication between glia); the inward-rectifying potassium channel Kir4.1 (enabling buffering of

extracellular potassium); and a host of ion channels and receptors for neurotransmitters. In mammals, radial glia differentiate into a cell type seemingly singularly optimized for filling the extracellular space with ramifying processes: the astrocyte.

Figure 1.2. Morphological variation across a range of individual radial glial cells. Reproduced from Sild and Ruthazer 2011. **(A)** A neuroepithelial stem cell. **(B)** A ventricular radial glial cell from the embryonic rat cortex. **(C)** Radial glial cell from optic tectum of the Xenopus tadpole. **(D)** A Müller glial cell from the rabbit retina. (E) A Bergmann glial cell from the rat cerebellum. **(F)** An infundibular tanycyte. Scale bar: 15 µm.

Astrocytes

In nearly all heavily-studied areas in the mammalian brain, a large fraction of radial glia lose their apical-basal polarity during brain maturation and differentiate into astrocytes, star-shaped cells that ramify heavily in neuropil (Fig. 1.3A-C). Despite their apparently

dissimilar morphology, astrocytes express essentially the same marker genes as radial glia.

The advent of calcium imaging revealed that astrocytes are surprisingly dynamic cells, and specifically that they respond to neuronal activity. Calcium imaging in cultured astrocytes revealed that exposing these cells to glutamate led to elevated intracellular calcium, and that elevated intracellular calcium could propagate within and between cells in spatially-propagating waves (Cornell-Bell et al. 1990). These phenomena were later observed in hippocampal slices, wherein axonal stimulation evoked similar calcium responses within and between astrocytes (Porter and McCarthy 1996), and in the retina, where electrical, mechanical, and chemical (through ATP) stimulation evoked calcium waves through Müller glia and retinal astrocytes (Newman and Zahs 1997). Further studies have revealed additional neurotransmitters that can evoke astrocytic calcium responses, such as GABA (Serrano 2006), acetylcholine (Araque et al. 2002) and norepinephrine (Paukert et al. 2014). All these neurotransmitters activate G protein-coupled receptors on astrocytes, which leads to release of calcium from internal stores via inositol-1,4,5- trisphosphate (IP_3) activation. Elevated intracellular calcium induces astrocytes to release glutamate, ATP, GABA, and D-serine; astrocytes may also respond to elevated intracellular calcium by altering the composition of the astrocytic membrane, e.g. by altering expression of ion channels. Taken together, all of these mechanisms give astrocytes extensive ability to sense and modulate synaptic activity, which has led to an augmented conception of synapses, the “tripartite synapse”, wherein synapses are composed of pre- and post-synaptic neuronal structures as well

as an astrocytic structure, and that dynamics of all three cells are contribute to long-term synaptic function. In addition to their influence on synaptic activity, astrocytes completely surround brain vasculature with endfeet and thereby bridge the nervous system and the circulatory system. Astrocyte responses to neuronal activity and other cues can drive vasoconstriction or vasodilation; these responses are also heralded by an increase in intracellular calcium in astrocytes (Reviewed in Petzold and Murthy 2011). Astrocytes are coupled via gap junctions, which allows calcium activity to spread from across the population of glia in waves (Fig. 1.3D). This phenomenon induced researchers to raise the possibility, still unverified, that astrocytic calcium excitability could represent a novel non-neuronal mechanism for long-range communication in the nervous system (Newman and Zahs 1997). In addition to population-level calcium events, functional imaging of single astrocytes has revealed calcium activity on a range of smaller spatial scales, within and between single cells (Shigetomi et al. 2016). The diversity of calcium signaling events within single astrocytes suggests that calcium-mediated excitability in astrocytes is very different from the all-or-none action-potential-mediated excitability in neurons. Therefore, from a signal processing perspective, astrocytic excitability (slow, more local, integrative) may complement neuronal excitability (fast, long-range) in circuit function. But at the moment this is hopeful speculation—because of the complexity of astrocytic calcium signaling and a relative shortage of tools for perturbing calcium excitability in astrocytes, there is little consensus as to the physiological *effects* of astrocytic calcium activity *in vivo*.

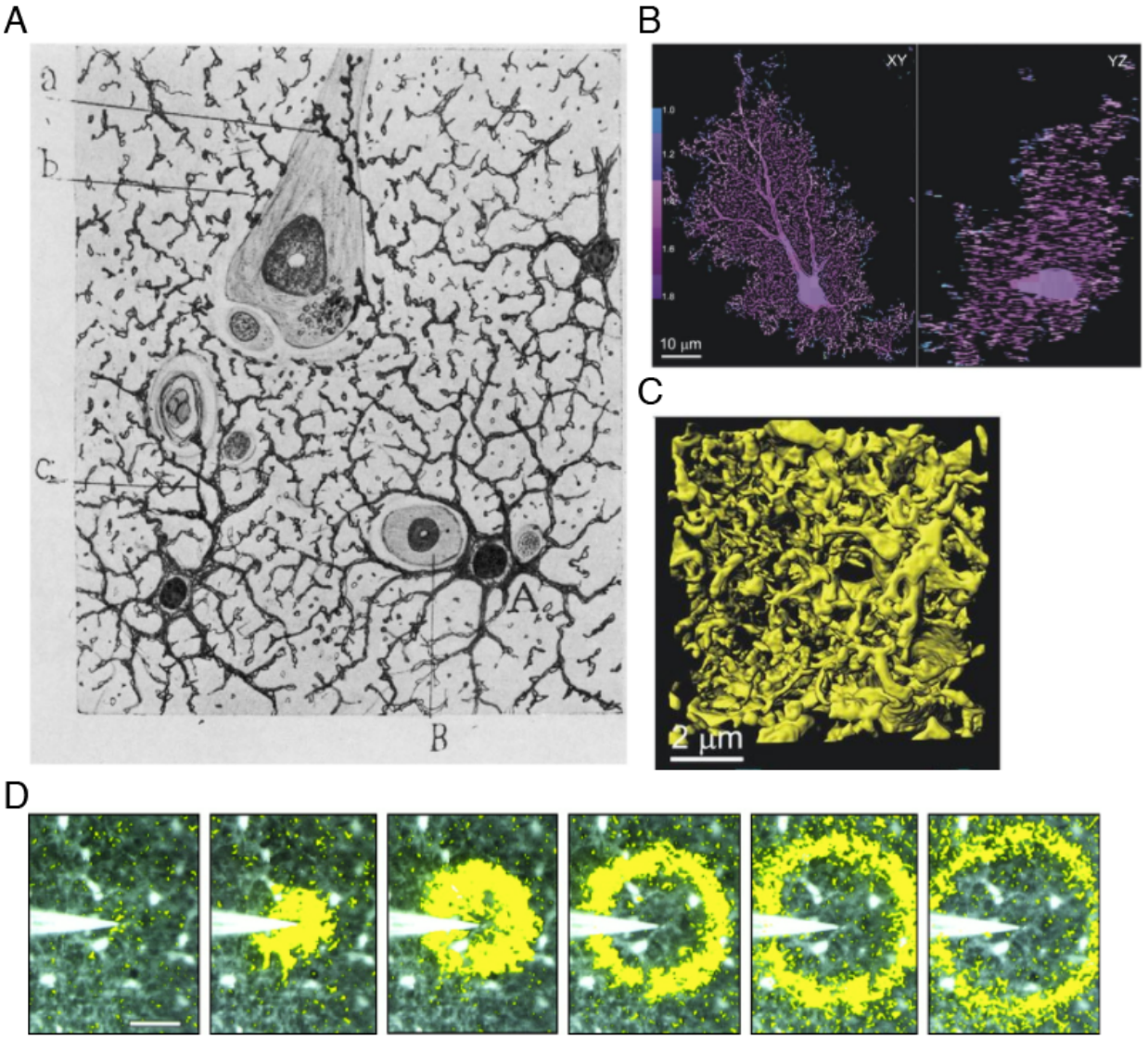

Figure 1.3. Astrocytes are ramifying glia that respond to extracellular events with calcium transients.
(A). A drawing, by Ramón y Cajal, of astrocytes and neurons in the human brain stained with gold chloride. Adapted from Somjen 1988. **(B)** Orthogonal slices through a single dye-filled astrocyte imaged with two-photon microscope. The color bar indicates the spatially-varying fractal dimension of the astrocytic processes, which is ~1.7 across most of the cell, indicating a high level of self-similarity. Adapted from Shigetomi et al. 2013. **(C)** Surface rendering of segmented astrocytic processes from a region of interest in a serial-section electron microscopy dataset. Adapted from Shigetomi et al. 2013. **(D)** Spatially-propagating astrocytic calcium activity in the retina evoked by punctate mechanical stimulation. The yellow rings represent the wavefront of the spatially propagating activity, as estimated by thresholding the discrete temporal derivative of the fluorescence images. The interval between the panels is .93 s. Adapted from Newman and Zahs 1997.

Astrocyte researchers have proposed a variety of theories which purport to link astrocytic calcium transients to effects on neuronal activity. On the more speculative end is the theory of “gliotransmission”, which holds that intracellular calcium transients drive release of neurotransmitters from astrocytes, either via vesicle-mediated release or through transmembrane channels. Evidence for this theory came from observation of putative membrane-anchored vesicles observed in electron micrographs of astrocytes (Bezzi et al. 2004) as well as evidence that exciting astrocytes can cause a variety of effects on neurons and synaptic transmission (Araque et al. 1998; Kang et al. 1998; Ma et al. 2016). An implicit corollary of the gliotransmission hypothesis is that ordinary synaptic activity and plasticity in the brain is heavily influenced by astrocytic conditioning. This claim and the interpretation of the evidence behind it have proven controversial. Experiments using knockout mice deficient in IP3R2-mediated calcium activity in astrocytes showed that, despite reduced astrocytic calcium activity in these animals, they had no apparent deficit in synaptic plasticity (Agulhon et al. 2010). A general criticism of the reports purporting to show gliotransmission is that the standard methods of perturbing astrocytes are unphysiological (Fiacco and McCarthy 2018), but this claim is also contentious (Savtchouk and Volterra 2018). Less controversial is the claim that astrocytes condition the extracellular space in a way that affects neuronal activity, e.g. astrocytes modulating neuronal activity by controlling the extracellular ion concentration (Wang et al. 2012b, 2012a; Morquette et al. 2015; Cui et al. 2018).

“Astroglia”

Although biology is what it is, how we conceptualize biological systems is shaped by how we as humans have chosen to study those systems. I have presented radial glia and astrocytes through the lens of the parochial history of how these cells have been studied: radial glia orchestrate neurogenesis (in vertebrates); astrocytes regulate the extracellular space in mature neuronal circuits (in mammals). Via this history, mouse astrocytes have become *de facto* the “model glial cell” for glia-neuron interactions, which has led to a generalization of the term "astrocyte” to denote “a glial cell that interacts with neurons à la mouse astrocytes”. This terminology is unfortunate; the term “astrocyte” literally means “star cell”, a reference to the unpolarized branching morphology of cells like those shown in Fig. 1.3A, but there are many glial cells that interact with neurons à la mouse astrocytes that are not star-shaped cells—these “astrocytes” (in the functional sense) are not “astrocytes” (in the morphological sense). The term “radial glia” brings additional problems: radial glia have been studied chiefly in mammals, with a focus on how the cells shape brain development (and comparatively scant focus on they interact with functional circuits). Radial glia become astrocytes as the mammalian brain matures; thus, the two cells types are temporally segregated. Because of (a) the temporal segregation between the cell types, (b) the fact that radial glia are studied in the context of brain development, and (c) use of the term “astrocyte” in the functional sense, some researchers conclude from nomenclature that radial glia are functionally distinct from astrocytes and therefore radial glia categorically do not interact with functioning neurons.

To add further confusion, there are specialized glial cells that are named after anatomists—Müller glia and Bergmann glia, which are endemic to the retina and cerebellum, respectively (Fig. 1.2D, E). These cells perfectly illustrate the onerousness of conventional terminology for glia: they are alternately and inconsistently labelled radial glia (in the anatomical sense: because they have a radial morphology) or astrocytes (in the functional sense: because they interact with mature neuronal circuits). For the purposes of this thesis, I would prefer a clearer terminology for glial cells. In later chapters I will be describing how glial cells in larval zebrafish, which are typically labelled “radial glia”, have properties previously described in mammalian astrocytes. In presentations, describing zebrafish radial glia with astrocytic properties confused many people, principally because they assumed that cells called “radial glia” could not be functionally similar to astrocytes, *by definition*. I would like to defuse this confusion. So, for the purposes of this thesis, I have decided to co-opt the term “astroglia” to describe glial cells that fill the extracellular space around neurons with ramifying processes and express some or all of the radial glial marker genes described previously—GFAP, vimentin, GLAST, Kir4.1, to name a few. By this definition, astrocytes are astroglia; cells that are inconsistently labelled astrocytes or radial glia, like Bergmann glia and Müller glia, are astroglia, and likely many radial glia in non-mammalian species are astroglia as well. In the future I anticipate that clearer terminology for glial cells will emerge as more glia are studied across different brain regions and in different organisms, and as glial function becomes understood at higher resolution.

Outlook

We now know that glia are essential for assembling and maintaining the nervous system, and the view that glia are (in some cases) co-equal with neurons for signal processing is gaining traction in the traditionally neuron-centric areas of neuroscience. There are two large gaps in our knowledge of glia that I believe should filled experimentally.

The first gap is the developmental trajectory of mammalian glia, from radial glia to astrocytes. We know from many *ex vivo* studies that the embryonic cortex (and many other brain areas) is populated by radial glia and nascent neurons. We also know that the adult mammalian cortex is populated by astrocytes (descended from radial glia) and mature neurons. At some point in brain development, glia must begin responding to neuronal activity, i.e. radial glia must gain astroglial traits, such as a ramifying morphology (and eventually become astrocytes). How does this happen? Specifically, how does this "astroglialization" influence or depend on the maturation of neuronal circuits in the brain? Experiments for attacking this question might take the form of time-lapse structural and functional imaging in the brains of developing animals, perhaps starting with well-studied circuits like the retina or cerebellum, with an emphasis on tracking how glial cell morphology changes (specifically, how astroglial morphological features emerge) in concert with the development of mature neuronal activity patterns. The study of cell morphology could be complemented by single-cell RNA sequencing or other measures of gene expression.

The second gap is an understanding of the diversity of astroglia (which I attempt to partially address in Chapter 2 by describing astroglia in larval zebrafish). With the exception of a small, but growing, effort to study astroglial cells in the fruit fly *Drosophila melanogaster* (Freeman 2015), nearly all studies of astroglia-neuron interactions have examined rodent astrocytes, Bergmann glia, and Müller glia. This focus on a single organism limits our capacity to generate a competent theory of astroglial function.

At the moment, *in vivo* or *in vitro* calcium imaging is our only tool for studying astroglial activity, especially astroglia-neuron interactions, where the astroglial calcium activity must be conditioned on neuronal activity; as this technique typically requires transgenic animals for imaging an entire cell type (e.g., glia), progress in this area is rate-limited by our ability to produce novel transgenic model organisms.

Zebrafish as model organism for neuroscience

Since its debut nearly 40 years ago as a model organism for studying developmental genetics (Walker and Streisinger 1983), the larval zebrafish (*Danio rerio*) has emerged as a compelling model for behavioral neuroscience research. For neuroscience, larval zebrafish have two large advantages over other vertebrate model organisms: they are nearly transparent, and their brains are small (~1 millimeter in length). Both of these features make larval zebrafish uniquely suited for electrophysiology and optical physiology, e.g., recording neural activity with calcium indicators, and perturbing neural activity with optogenetic actuators. In the following sections I will provide a brief overview of behavioral neuroscience using larval zebrafish, with an emphasis on two main techniques that have leveraged the advantages of larval zebrafish for studying

brain function: virtual reality behavioral experiments, and optical physiology through calcium imaging.

Behavior

Like many larval fish that receive no parental care, survival for wild larval zebrafish is determined by their ability to avoid mortal threats and find prey. Both of these objectives require a high level of motor control, which in normal zebrafish manifests mere hours after hatching. Larval zebrafish swim in a beat-and-glide fashion, with propulsive axial body bends followed by pauses in which the fish adopts a relaxed hydrodynamic posture (Fig. 1.4A). At 5 days past fertilization (dpf), larval zebrafish already exhibit a wide range of distinct locomotor behaviors, including directed escapes in response to visual or tactile stimuli, spontaneous or sensory-evoked forward swims, turns, and specialized motor sequences for prey capture (Easter and Nicola 1996; Borla et al. 2002; Johnson 2005). Broadly, behavioral neuroscience in larval zebrafish has focused on understanding the neural basis of these locomotor behaviors with a heavy use of optical methods for observing and perturbing the nervous system. Early imaging experiments used synthetic (O'Malley et al. 1996), and then genetically-encoded (Higashijima et al. 2006) calcium indicators to record neural activity in the hindbrain and spinal cord during reflexive motor behavior. Imaging during behavior allows experimenters to formulate hypotheses about the functional contribution of specific cells or cell types to behavior; these hypotheses can then be tested directly by optically ablating (Liu and Fetcho 1999), or optogenetically inhibiting or exciting these cells (Portugues et al. 2013).

Evoking zebrafish behavior using virtual reality

There is a tension inherent in using optical methods at cellular resolution to study motor behaviors—imaging or perturbation are easiest when the animal is restrained, but larval zebrafish engage in many interesting locomotor behaviors where sensory feedback is important for the behavior, such as prey capture and free swimming. Under this constraint, experimenters who wished to study the neurophysiological mechanisms of these behaviors developed behavioral assays where restrained fish could perform an action and receive naturalistic visual feedback from that action, all while under conditions suitable for microscopy (Bianco et al. 2011; Portugues and Engert 2011; Ahrens et al. 2012). These techniques, which were inspired by assays designed for studying insect optomotor behavior (Strauss et al. 1997) and rodent navigation (Holscher 2005), involve creating a virtual environment that is presented to the fish as a visual stimulus, dynamically recording the actions of the fish, and using those recorded actions to update the virtual environment (Fig. 1.4B). These paradigms work for restrained or paralyzed fish. If the fish are restrained, their tail movements can be recorded with a camera and used as input to the experiment control software (Fig 1.4C); if the fish are paralyzed, one can attach suction electrodes to the muscle of the fish and record impotent action potential volleys from motor neurons (Fig 1.5D); this “fictive swim” signal can be used as a proxy for a visual recording of the animal’s actual tail movements (Masino and Fetcho 2005).

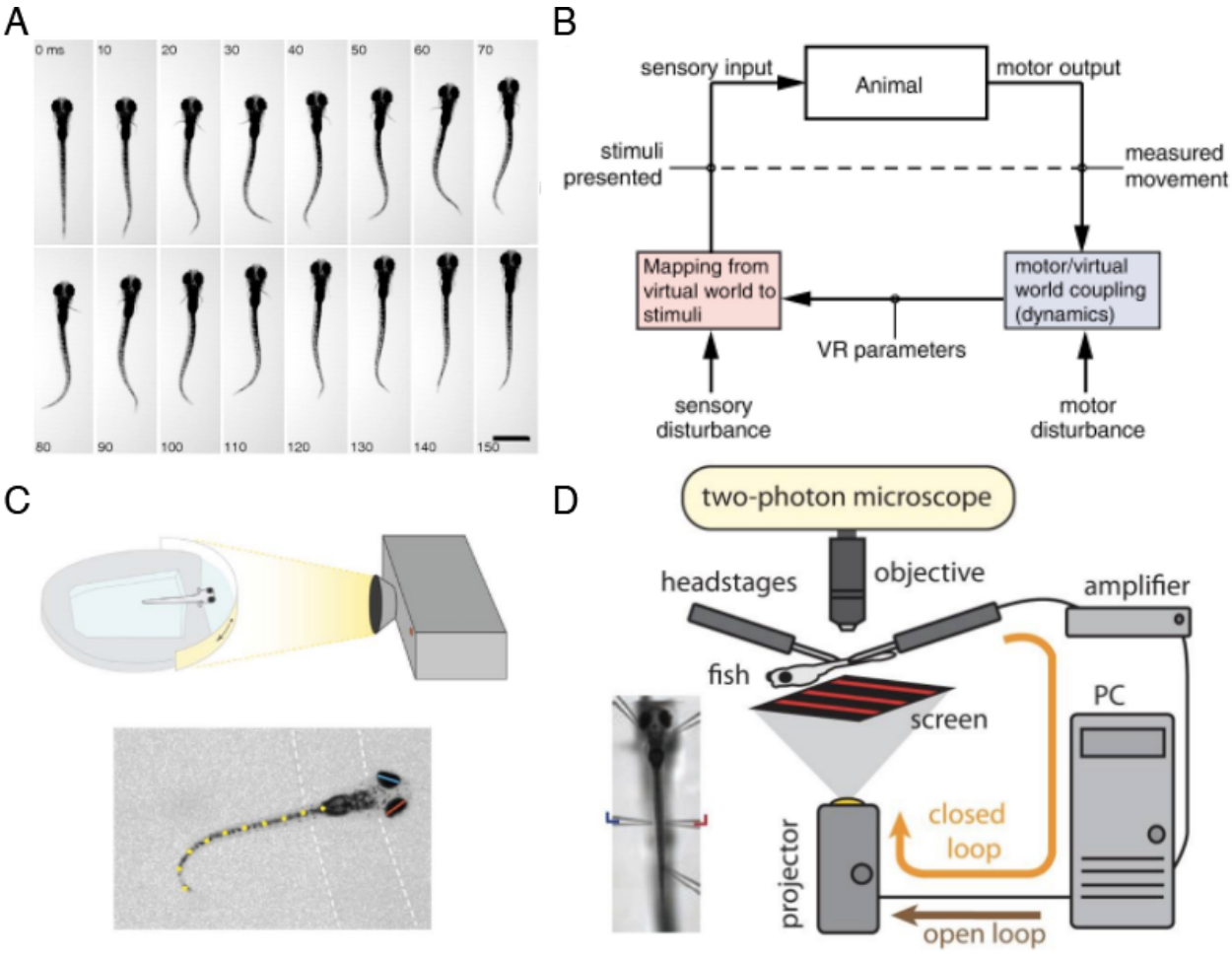

Figure 1.4. Actual and virtual zebrafish locomotion.
(A) Sample images, separated by 10 ms, from high-speed video recording of larval zebrafish performing a slow swim bout. Adapted from Green et al. 2011. **(B)** Schematic of the design of virtual reality (VR) experiments. The animal is presented with a synthetic stimulus; the animal's actions are recorded and used as input to a series of computations (elements below the dashed line) that will determine the resulting change in the stimulus. The recorded behavior is transformed into parameters in the coordinate system of the VR, with the option for adding an exogenous perturbation. These parameters are used to update the visual stimulus, with another opportunity for an exogenous perturbation (e.g., adding forward optic flow). Adapted from Dombeck and Reiser 2012. **(C)** An example schematic of a VR paradigm for studying eye and tail responses in restrained larval zebrafish. Top: a prey-like visual stimulus is projected on screen in front of an agarose-embedded fish. Bottom: kinematic parameters relevant for updating the visual stimulus are estimated from high-speed video of the fish. Adapted from Portugues and Engert 2011. **(D)** An example schematic of a VR paradigm for studying the optomotor response in paralyzed larval zebrafish. Fictive locomotion is recorded via tail-attached electrodes. This signal is used to dynamically accelerate the grating stimulus projected below the fish: when the fish attempts to swim, it sees a naturalistic (or non-naturalistic) effect on optic flow.

Functional imaging in zebrafish

Early calcium imaging experiments in larval zebrafish used confocal microscopes (O'Malley et al. 1996). Confocal microscopy has excellent spatial resolution and is logistically simple, given that large universities or medical centers have confocal microscopes in core facilities. That being said, the technique has some limitations, especially for functional imaging: first, confocal imaging rapidly bleaches fluorophores throughout the sample even when imaging a single plane, which limits its viability as a technique for imaging volumes; additionally, confocal microscopes excite fluorophores with visible light; for imaging GFP-derived fluorophores like GCaMP, this entails illuminating the fish brain with very bright blue light that may evoke an undesired behavioral response in the fish, as well as obscure any visual stimulus which the experimenter would like to present. Even if the visible excitation light were not an issue, the physical layout of a typical confocal makes it difficult or impossible to add the hardware required for delivering the types of visual stimuli shown in Fig. 1.4C and 1.4D. These issues were are all largely resolved by the development of two-photon microscopy (Denk et al. 1990), which uses a pulsed infrared laser to excite conventional fluorophores via two-photon absorption, a nonlinear optical process wherein two coincident photons at some wavelength λ are absorbed by a fluorophore with a nominal excitation peak at $\lambda/2$. Practically, this means driving emission of visible fluorophores with invisible infrared light. For labs that could afford the high cost of building a custom two-photon microscope, the benefits to functional imaging were immense: the two-photon excitation effect is a non-linear (quadratic) function of the excitation power,

which means that a focused two-photon laser only excites (and therefore, bleaches) fluorophores in a tiny volume around the focus of the beam. This process gives two-photon imaging high optical sectioning, with minimal photobleaching outside of the image plane of interest; these two traits makes it an effective technique for volumetric imaging. There are additional advantages: for imaging green fluorophores like the GCaMP family, the two-photon laser wavelength is in the neighborhood of 920 nm (approximately twice the one-photon excitation wavelength), which is invisible to fish. Thus, high-contrast visual stimuli can be designed easily (so long as they do not overlap with the emission wavelength of the target fluorophore). Custom-built two-photon microscopes also allow extensive freedom for customization and integration of the relevant hardware for virtual reality experiments, e.g., hardware for presenting a visual stimulus and recording animal behavior.

The early calcium imaging experiments in larval zebrafish involved labelling known cell types (e.g., spinal projection neurons) with a calcium indicator and imaging their responses in relation to behavior. With the combination of two-photon imaging, virtual reality, and transgenic fish expressing calcium indicators in many neurons, a new kind of exploratory experiment became popular. Researchers began imaging large numbers of neurons during behavior and searching for cell with a specific type of response (Ahrens et al. 2012; Orger and Portugues 2016; Lovett-Barron et al. 2017). Experiments of this form, where a large number of neurons across the brain are imaged together, placed a premium on imaging speed. Two-photon imaging involves scanning a focused laser beam through the sample, so image formation is the integration of a one-

dimensional mechanical process (raster scanning). Practically, this limits two-photon imaging speeds to approximately 30 Hz over a fish-brain-sized field of view. In the interest of performing functional imaging at higher speeds, light sheet microscopy has emerged as an alternative to two-photon microscopy. In light sheet microscopy, the entire focal plane of the detection objective is illuminated at once by a “sheet” of low numerical-aperture light that enters the sample from the side. The fluorescence emission from the entire focal plane is captured by a camera in a single exposure. By comparison with the point-scanning excitation method used in two-photon imaging, illuminating the entire sample plane at once with a light sheet (i.e., “plane-scanning” instead of “point-scanning”) grants a massive acceleration of imaging speeds—with a modern scientific camera, a fish-brain-sized field of view can be imaged at 200 Hz in a light sheet microscope. By moving the detection objective during imaging, it is possible to perform volumetric functional imaging across nearly the entire fish brain at a useful volumetric rate (1-3 Hz) at cellular resolution in behaving animals (Ahrens et al. 2013; Panier et al. 2013; Vladimirov et al. 2014).

Outlook

The larval zebrafish has the distinction of being the only vertebrate model organism with a brain that allows comprehensive, non-invasive physiology during behavior. There are several technological developments that promise to increase this advantage. Current functional imaging approaches use intracellular calcium concentration as a signal of neuronal activity. The intracellular calcium concentration is only an indirect reporter of action potentials: intracellular calcium contraction cannot convey reliably the timing of

individual action potentials, and it gives no information about the subthreshold membrane potential. Because both of these biophysical measurements are of importance for understanding the fine structure of communication between neurons, there is a large effort to develop optical reporters of membrane voltage (Kralj et al. 2012; Abdelfattah et al. 2018). On the larger scale, there are mounting efforts to generate connectomes for the larval zebrafish using light and electron microscopy (Hildebrand et al. 2017; Kunst et al. 2019), which promise to offer a picture of neuronal circuits at synaptic resolution.

The effort behind all these tools is impressive, but I suspect that too often the larval zebrafish is used by tool developers as a simple way to demonstrate some new microscopy technique (Fosque et al. 2015; Liu et al. 2018), and the resulting flurry of technical papers may belie the fact that these tools have not yet produced outsized progress on biological questions. Of course, we cannot expect tools alone to drive discovery—that drive must come from meaningful biological questions, and here I think behavioral neuroscience in larval zebrafish may face some challenges going forward. Besides their relatively simple optomotor behaviors (in comparison to adult zebrafish), it is not clear what else larvae can do—we have not observed larvae performing spatial navigation, or interacting with conspecifics in a complex fashion, or learning tasks. Mature fish surely do some or all of these behaviors, but mature fish are large (by microscopy standards) and inconvenient for imaging. If complexity of the nervous system necessarily precedes complexity of behavior, then the larval zebrafish fish brain may be much more complex than the actual behavior the animal performs, in which

case that complexity starts to look like a trap for behavioral neuroscientists and theorists who are bedazzled by all the imaging tools. But there may be other approaches for understanding the brain that make better use of the strengths of the larval zebrafish. For example, larval fish are growing animals; although at five days of age these animals chiefly avoid threats and eat, they possess brains that will eventually support a host of complex, cognitive behaviors. How does the brain scale up? How do complex behaviors emerge? These questions cannot be so easily asked in other model organisms, but they may be directly answered in zebrafish, e.g. by longitudinally studying brain development non-invasively in larval and juvenile fish as they mature. I consider this research direction particularly exciting because comprehensively understanding brain development and function will inevitably include glial cells, which are the subject of my attention in this thesis.

Chapter 2: Volumetric imaging of zebrafish astroglia indicates their functional similarity to mammalian astrocytes

Abstract

Extensive research in mice suggests that mammalian astroglia, including astrocytes, Müller glia and Bergmann glia, are critical for proper assembly and function of neural circuits throughout the brain. These cells respond to variations in local neuronal activity with transient increases in intracellular calcium, but a full picture of astroglial responses to neuronal activity in nervous system function is only starting to emerge. We report astroglial structures in the larval zebrafish brain that appear morphologically and functionally similar to mammalian astrocytes. These findings suggest that glia-neuron interactions are widespread throughout vertebrates, and establish the larval zebrafish as a model for studying this fundamental aspect of nervous system function.

Introduction

In the past two decades, larval zebrafish have emerged as a bountiful model for basic neuroscience research, owing largely to the optical accessibility of the larval fish nervous system and the availability of powerful genetic tools for creating transgenic animals. Neuroscience research in larval zebrafish has thus far centered around the role of neurons in processing sensory stimuli and driving behavior; at the same time, essentially no effort has been devoted towards investigating the contribution of astroglial cells to brain function in larval zebrafish. By contrast, astroglia in mice (astrocytes, Müller glia, Bergmann glia) have been studied extensively, with a particular emphasis on using calcium imaging to observe how these cells dynamically interact with neurons

and neuronal circuits (Benediktsson et al. 2005; Schummers et al. 2008). The conspicuous absence of research on zebrafish astroglial dynamics seemed to us a missed opportunity which we could immediately address using our existing tools for volumetric imaging.

In the interest of establishing larval zebrafish as a model system for studying glia-neuron dynamics, we created transgenic larval zebrafish expressing calcium indicators in astroglial cells and used these animals to characterize the basic anatomical, functional, and genetic properties of zebrafish astroglia.

In this chapter, I begin by describing the morphological structure of astroglia across the brain of the larval zebrafish. I show that the morphology of larval zebrafish astroglia is consistent with reports of astroglial structure from adult zebrafish, and that larval zebrafish astroglia ramify extensively in neuropil regions. Using high-speed volumetric fluorescence imaging, we then found that zebrafish astroglia engage in complex calcium signaling events on multiple spatiotemporal scales. Taken together, the results here indicate that zebrafish astroglia can be considered homologous in many ways to mammalian astrocytes. Additionally, I demonstrate the power of fast volumetric imaging for studying excitability in astroglia. I hope that the results presented here motivate further studies of astroglial function in larval zebrafish.

Results

Anatomical structure of zebrafish astroglia

I began by characterizing the structure and distribution of astroglia in transgenic larval zebrafish using fluorescence microscopy. Optically, we have extensive access

throughout the fish brain, but our lab has thus far focused on the neural control of movement in the hindbrain, so the subsequent anatomical studies will focus on that brain region.

We expressed a variety of fluorescent reporters under the promoter for glial fibrillary acid protein (GFAP), an intermediate filament with expression restricted to astroglia (Bernardos and Raymond 2006). Fish used for these experiments were within the range of ages typically used for behavioral experiments i.e., 5-9 days past fertilization (dpf). Based on prior reports of astroglial structures in adult zebrafish (Than-Trong and Bally-Cuif 2015) and *xenopus* tadpoles (Sild et al. 2016) we anticipated that larval zebrafish astroglia would exhibit a radial morphology, with cell bodies abutting ventricular surfaces and sending long fibers projecting to pial surfaces, terminating in endfeet. To clearly resolve the distribution of astroglial cell bodies, we created fish expressing nuclear-localized GCaMP6f under the GFAP promoter. From imaging these animals, we observed that astroglial somata are highly clustered around the ventricular zones throughout the brain (Fig. 2.1A, B). In the spinal cord and hindbrain, astroglial somata are distributed along the midline ventricular surface (Fig. 2.1A, B). In addition to brightly labelled putative astroglial somata, we also observed many dimly labelled nuclei throughout the brain and spinal cord, which we suspected to be neurons.

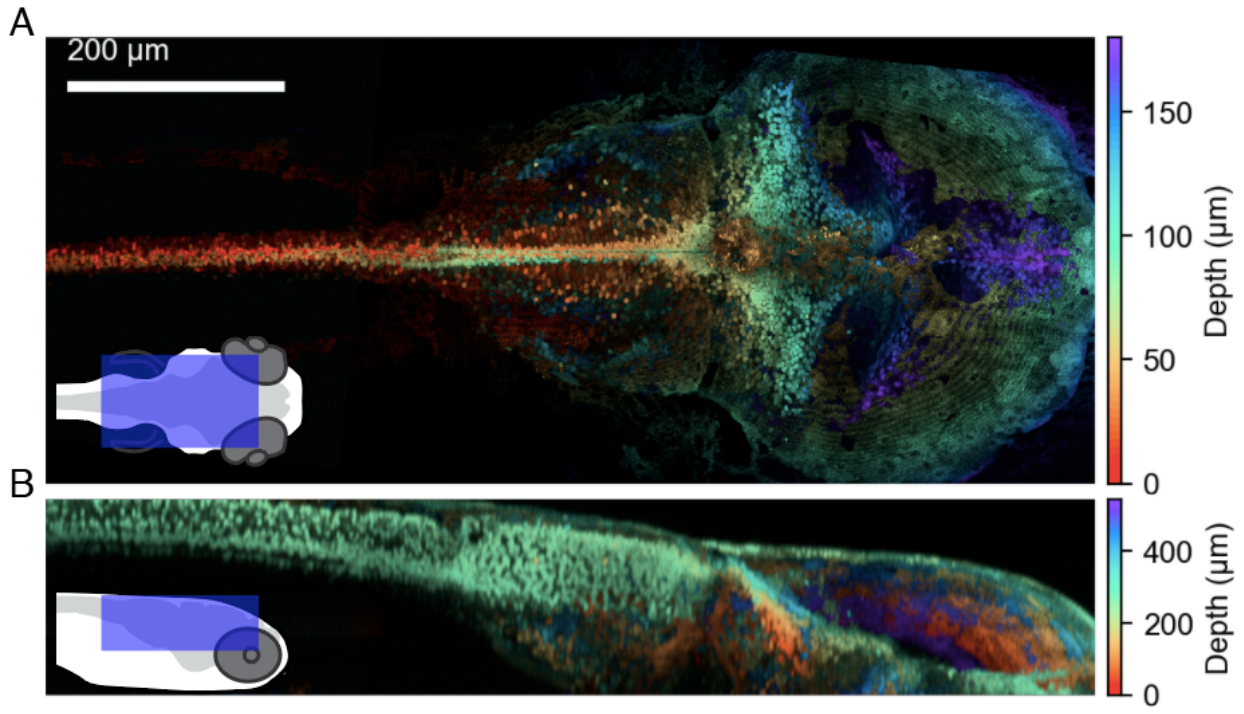

Figure 2.1. The distribution of astroglial nuclei.
(A,B) Color-coded maximum projections along the dorso-ventral (top) and medio-lateral (bottom) axes of a confocal stack of a 6 dpf Tg(*gfap:h2b-GCaMP6f*) fish. There is considerable autofluorescence, especially above the optic tectum. There are also many dimly fluorescent cells emanating away from the ventricular zones. These cells are unlikely to be astroglia. Distance in the volume is encoded by color. Astroglial nuclei throughout the brain are concentrated near ventricular surfaces.

To examine the gross morphology of the astroglial processes and their spatial relationship relative to neuronal cell bodies, we generated double-transgenic animals expressing the red fluorophore TdTomato under the GFAP promoter, and GCaMP6f under the neuronal promoter Elavl3 with the nuclear-localization tag H2B; we then imaged these animals with a confocal microscope. In order to more clearly visualize the distribution and orientation of the radial glial fibers, we filtered the astroglial channel of the confocal stack with an isotropic band-pass filter with a low passband (Fig. 2.3; methods). At a coarse level, we observed that astroglia send processes through regions of the brain rich in neuronal cells bodies before ramifying in neuropil regions (which

appear as voids in nuclear-localized neuronal imaging) (Figs. 2.2, 2.3). We did not observe a high degree of curvature or tortuosity in astroglial projections, and adjacent astroglia appeared to have very similar projection patterns. In the spinal cord and caudal hindbrain, I found that astroglia project radially to pial surfaces (Fig. 2.3B, bottom right) as previously described (Johnson et al. 2016), but in more rostral regions of the hindbrain, astroglial cell bodies occupy increasingly dorsal ventricular territory and these cells project more ventrally (Fig. 2.3A, B) —in the extreme case, astroglia with somata abutting the ventral aspect of the upper rhombic lip project nearly parallel with the dorsal-ventral axis (Fig 2.3A, top left). Presumably the projection angle of these astroglia changes as pial tissue expands and reshapes the brain during development. We do not know why, but we observed very weak labelling of astroglial cells in the optic tectum (Fig. 2.3B). Subsequent functional imaging results later in this chapter will indicate that there are abundant astroglia in the optic tectum, so we assume that the weak labelling is due to weak GFAP promoter activity in the optic tectum astroglia.

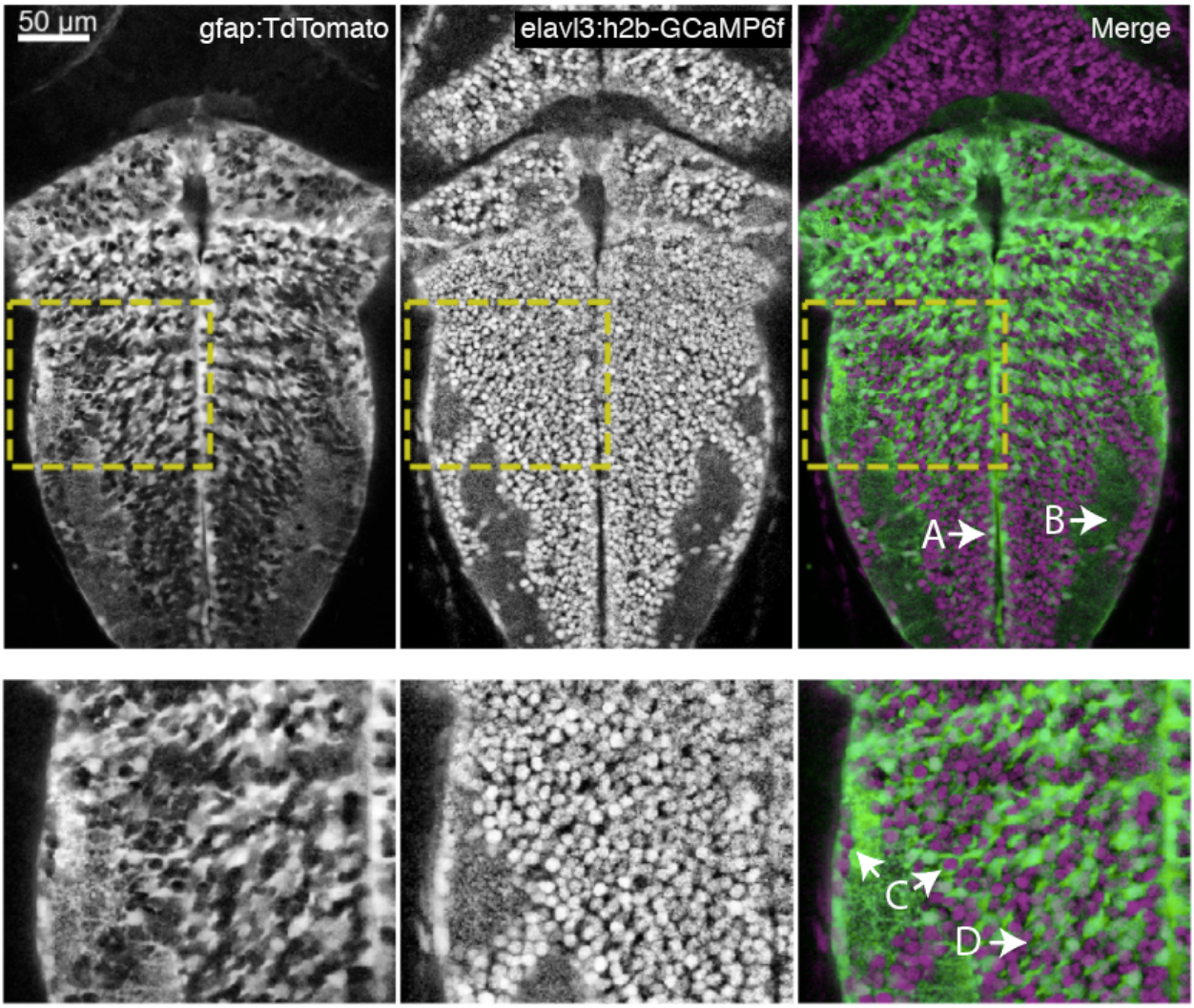

Figure 2.2. The distribution of astroglial processes and neuronal cell bodies in the hindbrain.
Shown is a single coronal plane through the fish hindbrain and midbrain from imaging data acquired with a confocal microscope in a double-transgenic *Tg(gfap:TdTomato);* Tg(*elavl3:h2b-GCaMP6f*) fish at 4 dpf. There is some bleedthrough of astroglial TdTomato signal into the neuronal color channel, as indicated by hazy labelling of neuropil regions in the middle column. **(A)** Example of astroglial somata concentrated along the midline, abutting the ventricular space. There are many double-labelled cells, but those along the ventricular zone are the **(B)** Astroglial processes ramify in neuropil regions (i.e., regions of the brain where neuronal nuclei are absent). **(C)** Some neuronal somata are surrounded by astroglial processes. **(D)** Parallel astroglial projections sliced coronally appear as arrays of ellipsoids.

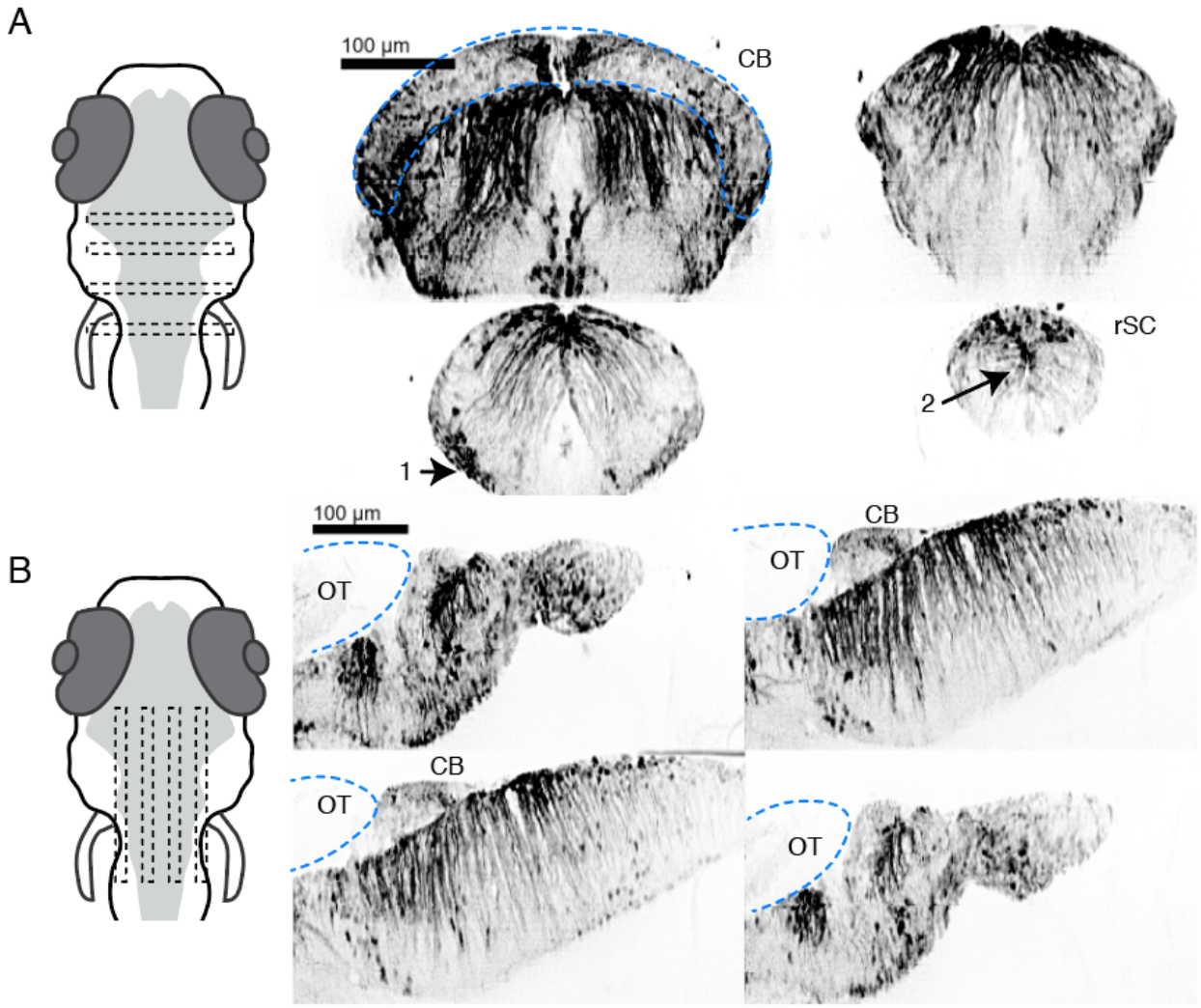

Figure 2.3. Projection patterns of astroglial processes in the hindbrain.
A confocal stack from a 4 dpf Tg(*gfap:TdTomato*) larva was band-pass filtered and localy maximum projected. The passband of the image filter was optimized for emphasizing the radial morphology and somata while removing fine processes (gliapil). Local maximum projections enable visualizing sparse anatomical structures over moderately-sized volumes. **(A)** A sequence of local maximum projections along the rostro-caudal axis of of the hindbrain and midbrain, illustrated via the cartoon on the left. Endfeet are apparent at the ventrolateral aspect of the brain (1). The projection target of astroglial radial projections grows increasingly ventral, and the location of the astroglial cell bodies grows increasingly dorsal, from the rostral spinal cord (rSC) to the midbrain (2). **(B)** The same display method from (A), but with projections along the medio-lateral axis. Abbreviations: CB = cerebellum; rSC = rostral spinal cord; OT = optic tectum

As the larval zebrafish is a developing organism, we were interested in whether

astroglia in larva resembled astroglia in adult fish. In mammals, glial morphology

changes drastically during development, as radial glia largely differentiate into astrocytes. To examine the morphology of single astroglial cells, we generated sparse transgenic animals by injecting the *tol2* recombinase along with a plasmid carrying *gfap:GCaMP6f*, which yielded animals with a varying density of labelled astroglia. We then screened for sparse-expressing animals and performed high-resolution confocal imaging. We found that individual astroglia in larval animals bear a striking resemblance to their adult counterparts (Fig. 2.4A,B); in particular, both larval and adult astroglia form extensive ramifying processes in neuropil regions. This observation does not preclude the possibility that there are substantial functional differences between larval and adult astroglia, but the commonality does at least suggest that, to the extent that form and function are linked in these cells, astroglia in larval animals are functionally similar to astroglia in adults.

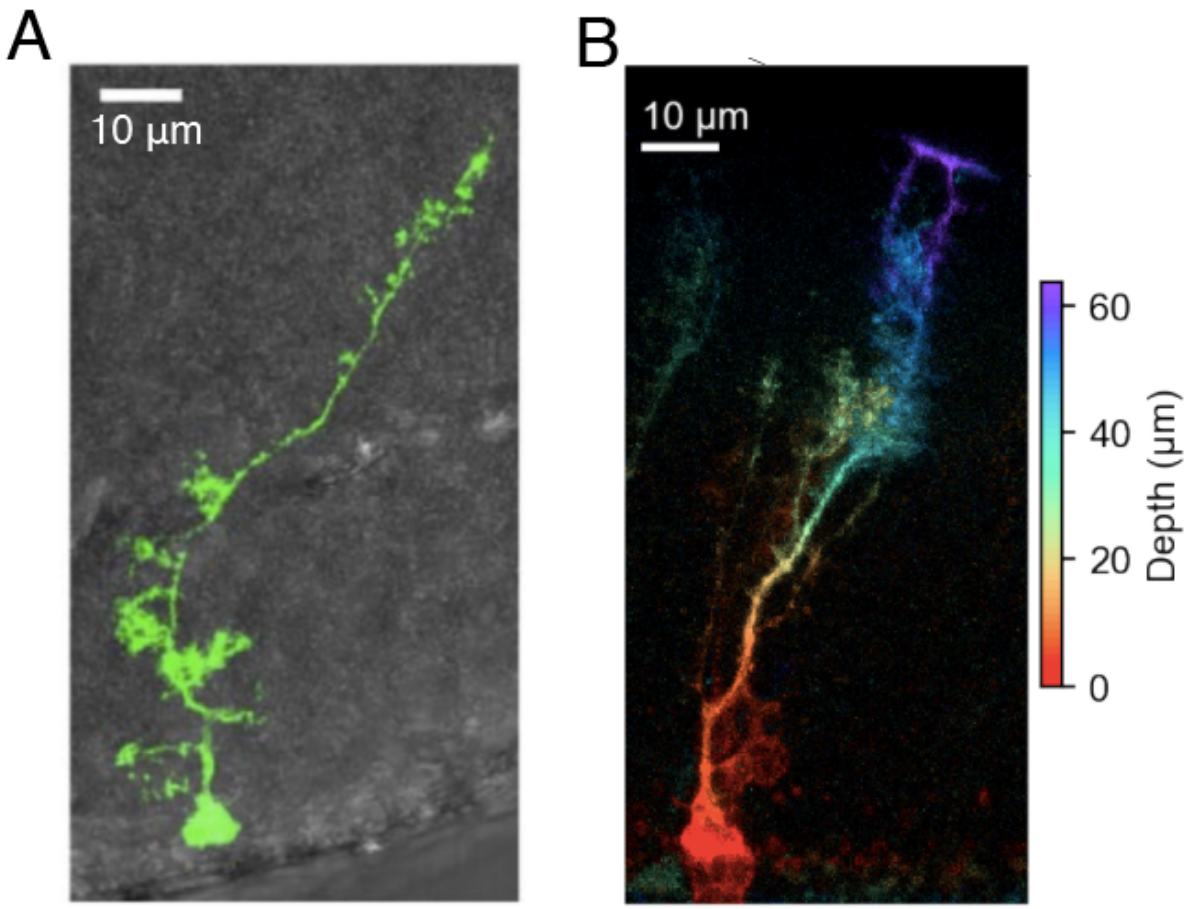

Figure 2.4. Larval zebrafish astroglia are morphologically mature.
(A) A single astroglial cell from the telencephalon of an adult zebrafish, fluorescently labelled via electroporation. Adapted from Chapouton et al. 2010. **(B)** A color-coded maximum depth projection of a brightly-labelled astroglial cell from an 8 dpf larval zebrafish transiently expressing *gfap:GCaMP6f*. The cell forms ramifications as it passes through a neuropil region before forming endfeet at the boundary of the brain (upper right, blue).

Anomalous cells labelled by the GFAP promoter

In transgenic fish with both cytosolic and nuclear-localized fluorophores under the GFAP promoter, we observed anomalous dimly labeled cells that we deemed more likely to be nascent neurons rather than astroglia based on the following properties: these anomalous cells do not exhibit expected astroglial morphology or soma localization; these anomalous cells are found in brain areas known to be densely

packed with neurons; and these anomalous cells are counter-labelled by fluorophores expressed under the neuron-specific promotor for Elavl3 **(**Fig 2.1A, Fig 2.2). We concluded that many of these anomalous cells are likely neurons, which is not surprising given that radial glia divide asymmetrically to produce neurons (Malatesta et al. 2000; Johnson et al. 2016).

What can explain labelled neurons in a GFAP transgenic fish? One possibility is that the neuronal daughter cells inherit fluorescent proteins expressed by their glial progenitors, and these proteins persist until they are degraded. Data on the decay half-life for the fluorophores we used (GCaMP6f, tdTomato) are not available, but the decay half-life of green fluorescent protein (GFP) is reported to be approximately 26 hours in mammalian cells (Corish and Tyler-Smith 1999). If we assume the fluorophores used in the present study are approximately as stable as GFP, then we should expect some fluorophore inheritance to occur, given that larval zebrafish are undergoing active neurogenesis.

Another possible explanation for labelled neurons in the GFAP-transgenic fish is that the GFAP promoter may not be perfectly specific to glial cells. This possibility contains a range of sub-possibilities: in a mild case, nascent neurons may present with decaying levels of GFAP promoter activity; in an extreme case, there may be mature neurons with high GFAP promoter activity. We cannot distinguish between either of these possibilities using the data presented here, but the distribution of labelled cells in adult GFAP transgenics is much sparser and more restricted to the ventricular zones (Bernardos and Raymond 2006), so the fluorophore decay theory seems likely.

The GFAP promoter may also drive variable expression of fluorophores across subpopulations of astroglia. For example, our GFAP transgenic fish have relatively sparse labelling in the optic tectum, while a transgenic fish expressing markers using the her4.1 promoter have much denser labelling of astroglia in the optic tectum. Researchers studying mouse astrocytes have found that the GFAP promoter only labels a subpopulation of astrocytes in the mouse brain (Walz 2000), and have since invested in variations of the GFAP promoter or alternative promoters that label a larger fraction of astroglia. Given these caveats, it is important to bear in mind that a) we cannot be certain that all cells labelled by the GFAP promoter are astroglia, and b) we cannot be certain that all astroglia are labelled by the GFAP promoter. Nonetheless, our GFAP transgenic animals formed a sufficient basis for us to initialize the next phase of our research: studying the calcium dynamics of astroglia in larval zebrafish.

Multiscale calcium dynamics observed in larval zebrafish astroglia

Astroglial calcium activity spans multiple spatial scales, from compartmentalized opening of few transmembrane calcium channels, to coordinated calcium waves propagating across populations of cells via gap junctions (Shigetomi et al. 2016). Comprehensively observing astroglial calcium activity requires imaging populations of astroglia in their entirety, from end-foot to cell body, over hundreds to thousands of cells. To this end we used light sheet microscopy, which allows rapid, long-term volumetric imaging in transparent samples at resolution sufficient to capture sub-cellular events (Keller et al. 2008; Vladimirov et al. 2014). Using this technique, we observed calcium activity in astroglia across a range of spatial and temporal scales; the calcium

activity we observed is broadly consistent with what other researchers have observed in mammalian astroglia. Furthermore, our use of volumetric imaging allowed us to observe phenomena that would not be easily detected using planar imaging in rodents. For the purposes of this chapter, I will focus on calcium signaling events at two scales: spontaneous transients, which often involve calcium activity in subcellular compartment or a single cell; and brain-wide events, where are events where large numbers of astroglia are excited at once across the brain, typically after vigorous motor behavior. It is a bit unfortunate to call a biological event "spontaneous" when what we really mean is that we do not know what caused that event, but this is standard terminology, for better or for worse.

Spontaneous calcium events

From calcium imaging studies of mammalian astrocytes, we know that individual astrocytes are often host to spatially and temporally independent calcium events, which are presumed to be local responses to synaptic activity (Shigetomi et al. 2013b). We found many examples of this small-scale calcium activity in our volumetric imaging data. These calcium events were typically short in duration (1-10s) and spatially confined to small compartment within a single cell, e.g. a radial process, or a portion of gliapil, or an endfoot. We also observed many instances of calcium activity spreading within individual cells, or between cells. These events were rarer and longer than the subcellular events. Volumetric imaging allowed us to visualize the full extent of these spatially-propagating calcium events (Fig. 2.5 A-C). For example, the calcium transients shown in Figure 2.5B and 2.5C would appear as transient fluorescent spots if imaged

with a planar imaging modality, whereas our use of fast volumetric imaging reveals the full spatial extent of these calcium events.

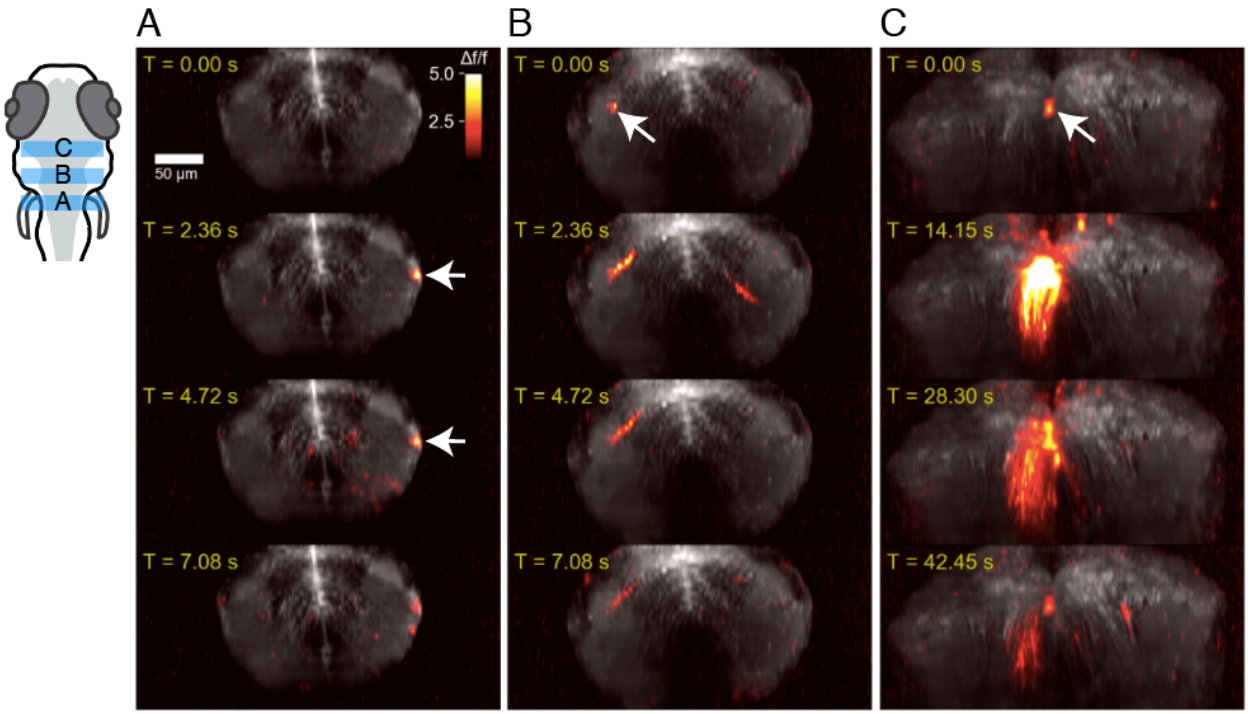

Figure 2.5. Sparse, transient calcium activity in astroglia.
Panels A-C show calcium activity within 3 maximum projections of frontal slices of the hindbrain of a *Tg(gfap:GCaMP6f)* fish at 5 dpf. **(A)** A brief calcium transient in a single astroglial endfoot (arrows). **(B)** A calcium transient that starts in a neuropil region (arrow) in the hindbrain, presumably in fine astroglial processes; the calcium activity spreads to the radial fiber of the astroglial cell. **(C)** A calcium transient that starts from a single astroglial soma (arrow) and spreads to a large number of adjacent cells over a much longer period of time than the transients depicted in (A) and (B). In addition to spreading laterally between cells, the calcium activity spreads ventrally down radial processes.

Given our background in relating calcium activity in neurons to behavior, we wanted to know if we could relate the timing of these calcium transients to some behavioral or sensory process, but we could find no such relationship. We looked for spatial or temporal structure in a large number of spontaneous calcium transients and found neither (Figure 2,6A,B). Even very proximal astroglial processes had very dissimilar

calcium activity timeseries. Given the segmental organization of the fish hindbrain, and the fact that most non-escape behavior is driven by the coordinated activity of populations of cells, it would be incredibly surprising if a single calcium transient in a single astroglial endfoot (e.g., Fig. 2.5A) could be predicted by, or have a measurable effect on, the animal's behavior. Instead, it's much more likely that these transients are responses to spatially localized extracellular cues. At this point we can only approach these calcium transients phenomenologically. We do not know what triggers these events, nor do we understand the mechanism or regulation of the spatial propagation of these events within and between cells. These transients can be quite complex—for example, the multi-cell transient depicted in Figure 2.5C starts within a single cell and spreads to neighboring cells, while also spreading within cells.

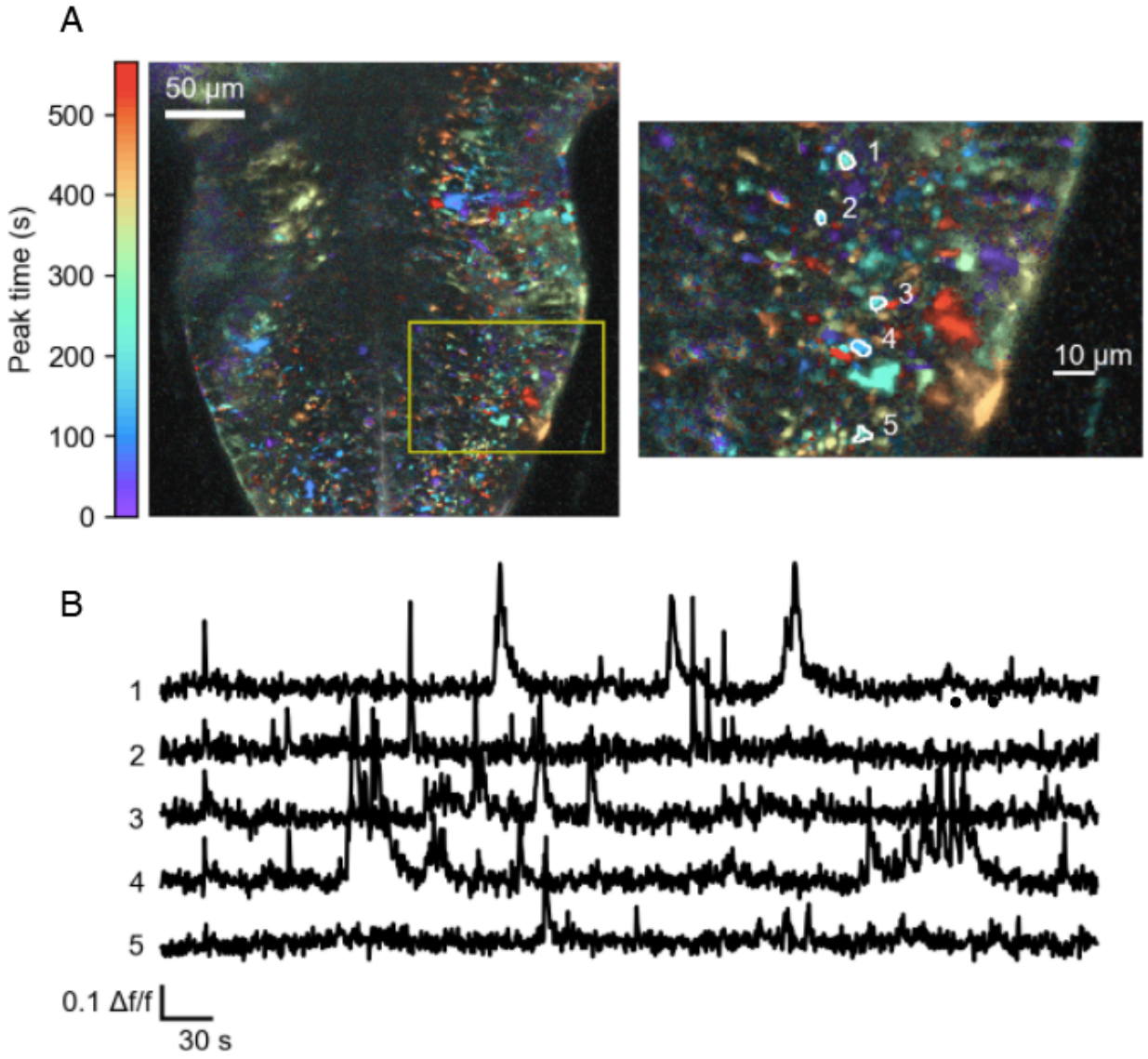

Figure 2.6. Sparse, independent astroglial calcium transients across the hindbrain. **(A)** A single plane from a volumetric imaging dataset from *Tg(gfap:GCaMP6f)* fish at 5 dpf. The time of the peak calcium activity over a range of 10 minutes is color-coded for each pixel. The varying colors throughout the hindbrain indicate that over this 10-minute timespan the calcium transients are largely uncorrelated, even for astroglial processes in close proximity. The enlarged portion of the image shows endfeet at the edge of the brain and astroglial projections *en passant*, all with largely independent calcium transients. **(B)** The time series of hand-drawn regions of interest (ROI), indicated by numbered polygons in the right column of (A). With the exception of single coordinated transient ~30s into the recording, there is no clear coordination of these events.

Brain-wide events

In addition to the so-called spontaneous events previous described, we consistently observed large ensembles of astroglia engaged in spatially-propagating waves of calcium activity. An example of this phenomenon is shown in Figure 2.7. This kind of calcium activity is difficult to visualize, as these brain-wide events have dynamics in time and three spatial dimensions. Like the single-cell events depicted earlier, these brain-wide calcium events are largely all-or-none, and thus for the purposes of visualization these events can be approximately described with two parameters per voxel—peak intensity and phase (e.g., the relative time when the voxel reached peak intensity). Several additional features of these events are worth noting. First, in contrast to the spontaneous calcium transients depicted in Figures 2.5 and 2.6 (which emerge from a single point of origin), these brain-wide events begin with sparse calcium activity widely distributed across the brain (Fig. 2.7A); this pattern that suggests that some coordinated change in the extracellular environment, e.g. the release of a neuromodulator, is the trigger for the event. To add support to his hypothesis, we noticed that there was a tendency for the earliest calcium activity to occur in neuropil regions, e.g. the ventral hindbrain, cerebellar neuropil (Fig. 2.7A); these are compartments known to receive projections from neuromodulatory nuclei (Tay et al. 2011). After their onset, these sparse calcium responses spread within and between astroglia; this could be mediated by cell-cell communication between astroglia, and regenerative calcium currents within astroglia. In many parts of the brain, such as the hindbrain and optic tectum, calcium waves propagate to astroglial somata (Figs. 2.7, 2.8), which led us to suspect that these

large-scale calcium events may represent a signaling pathway from astroglial processes (which sense neuronal activity) to their somata (which control neurogenesis and gene expression). But if these brain-wide events do represent a form of signaling within astroglia, that signaling is highly variable within and between fish. Within a single animal, the strongest brain-wide events may excite astroglial somata; but in weaker events, somatic excitation is not evident (Fig 2.7B), and likewise for other astroglial processes, like endfeet. The spatial extent of brain-wide astroglial events also varies extensively between animals. In some animals, e.g. the animal shown in Figure 2.8, astroglia in the optic tectum are potently excited, while in other fish the tectal astroglia are not recruited at all (Fig. 2.7). In summary, the crude phenomenology I present here suggests that, under certain circumstances, astroglia across the fish brain receive a common excitatory input that induces localized calcium responses in ramifying processes; subsequently, this calcium activity spreads within and between astroglia in a complex and variable spatiotemporal pattern.

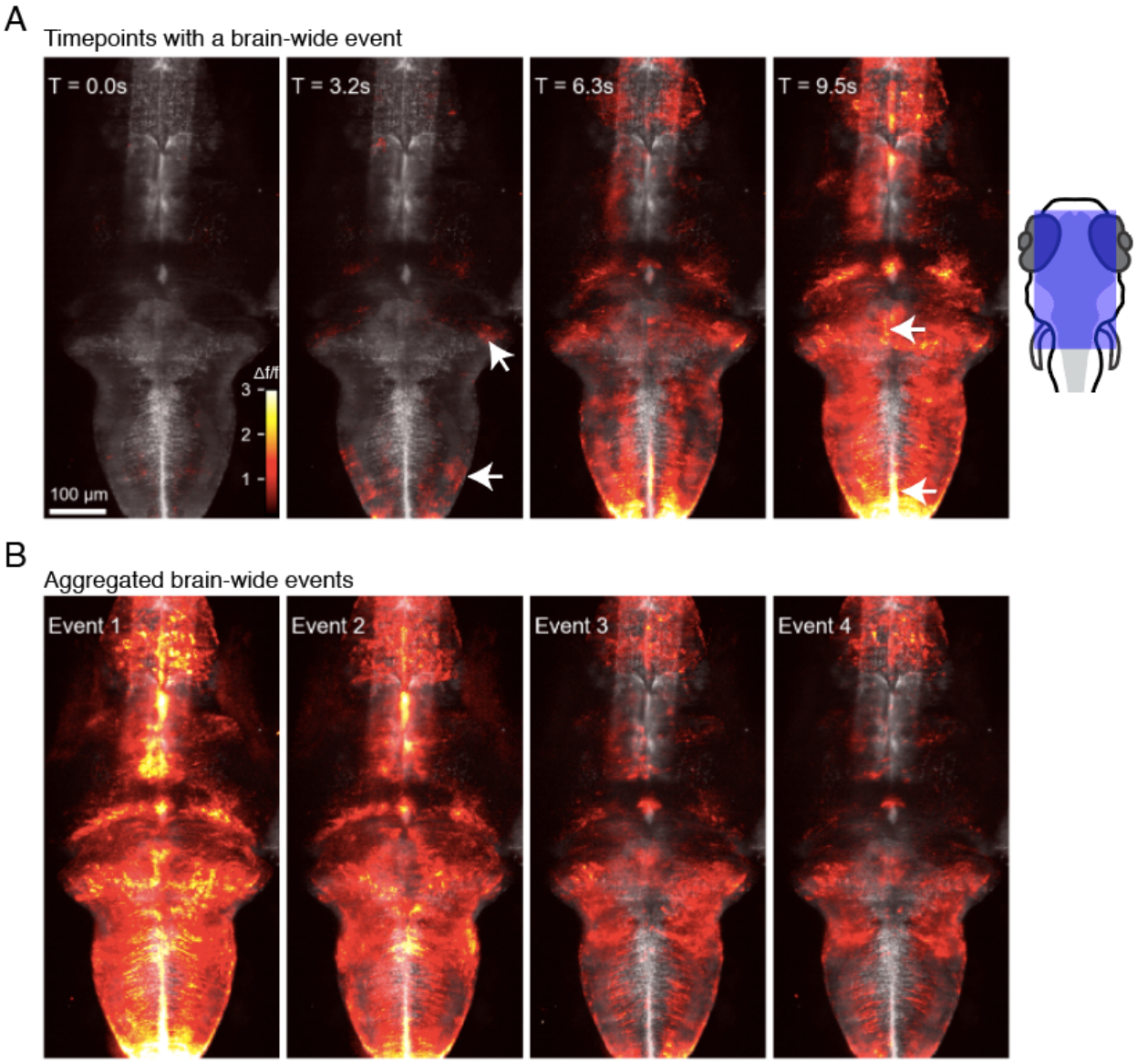

Figure 2.7. Brain-wide astroglial calcium waves.
(A) A sequence of maximum *z*-projections from a volumetric dataset recorded from a 6 dpf *Tg(gfap:GCaMP6f)* fish. These projections demonstrate calcium transients in astroglia across the brain. At 3.2s, localized calcium activity can be seen in astroglial ramifications in the hindbrain and midbrain (arrows). At 6.3s, calcium activity has spread throughout astroglial fibers across the brain, including the forebrain and astroglial somata in the hindbrain. At 9.5s, astroglial calcium activity has spread to astroglial somata across the brain (arrows). **(B)** A sequence of maximum *z*- and *t*-projections over examples of individual brain-wide events depicting the aggregate astroglial calcium activity for each event. Events are ordered by intensity of population astroglial calcium activity. In only the first two events does calcium activity spreads to astroglial somata along the ventricular surfaces of the brain; the spatial distribution and intensity of calcium activity in astroglial processes is also quite variable between events.

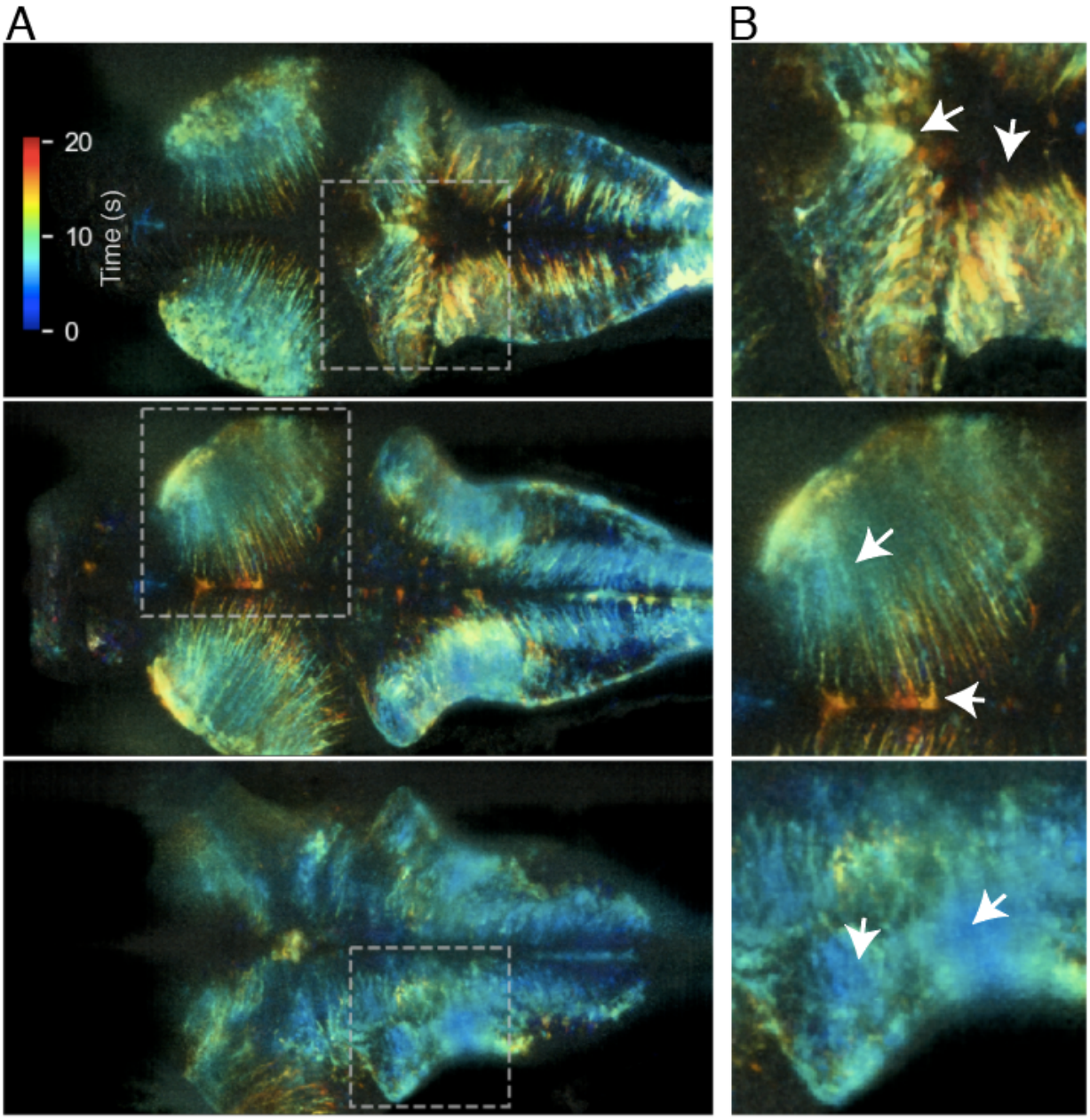

Figure 2.8. Spatiotemporal evolution of a brain-wide calcium wave.
Visualizing spatial distribution of calcium activity timing in a single brain-wide calcium event using a temporal color code in a 6 dpf *Tg(gfap:GCaMP6f)* fish. **(A)** Data were maximum projected in 3 chunks along the *z*-axis, then the timeseries of each pixel was mapped to a range of colors and the mean was taken along the projection axis. The color of a pixel thus represents the times when that pixel had the highest calcium activity, with bluer colors representing earlier activity and redder colors representing later activity (see colorbar). Continuously varying colors, which indicate spatially propagating calcium activity, are abundant throughout the brain. Pixels in the most ventral projection are blue-shifted, indicating that the calcium activity began in this part of the brain before spreading to the green- and red-shifted regions shown in the middle

Figure 2.8 (continued) and upper projections. **(B)** Enlarged regions of interest from the image sequence shown in (A). First row: calcium activity propagating via processes reached astroglial somata in the cerebellum (left arrow), but not somata in the anterior hindbrain (right arrow). This contrasts with events 1 and 2 in Figure 2.7B, which did excite dorsal hindbrain somata. Second row: calcium activity spread from the optic tectum neuropil (top arrow) to a few astroglial somata (bottom arrow) after about 10s. Third row: the earliest calcium activity occurs in patches of astroglial ramifications that are surrounded by less blue coloration, indicating spatial propagation (arrows).

We next asked whether these events were at all related to larval zebrafish behavior. In mice, spatially-propagating calcium waves been reported in radial glia and astrocytes (Cornell-Bell et al. 1990; Weissman et al. 2004), but a clear link between these phenomena and behavior has not been shown, nor could a link to behavior ever be shown easily, given that calcium waves in mammalian cells are typically observed in brain slices. However, our use of larval zebrafish as a model allows us to simultaneously observe astroglial calcium activity across the brain while the animal engages in fictive behavior. Additionally, we can image neurons and astroglia simultaneously in fish expressing spectrally separable calcium indicators, e.g. GCaMP5f and jRGECO1b. When we examined the fictive behavior and neuronal activity of larval zebrafish around brain-wide events, we observed that these large-scale astroglia calcium transients were often preceded by vigorous locomotor activity, and correspondingly vigorous neuronal calcium activity. During the peak of these brain-wide events, both behavior and neuronal calcium activity were quiescent (Fig. 2.9A,B). Because fluctuations in population neuronal activity correlate so well with fictive behavior, subsequent results will use population neuronal activity as a proxy for fictive behavior.

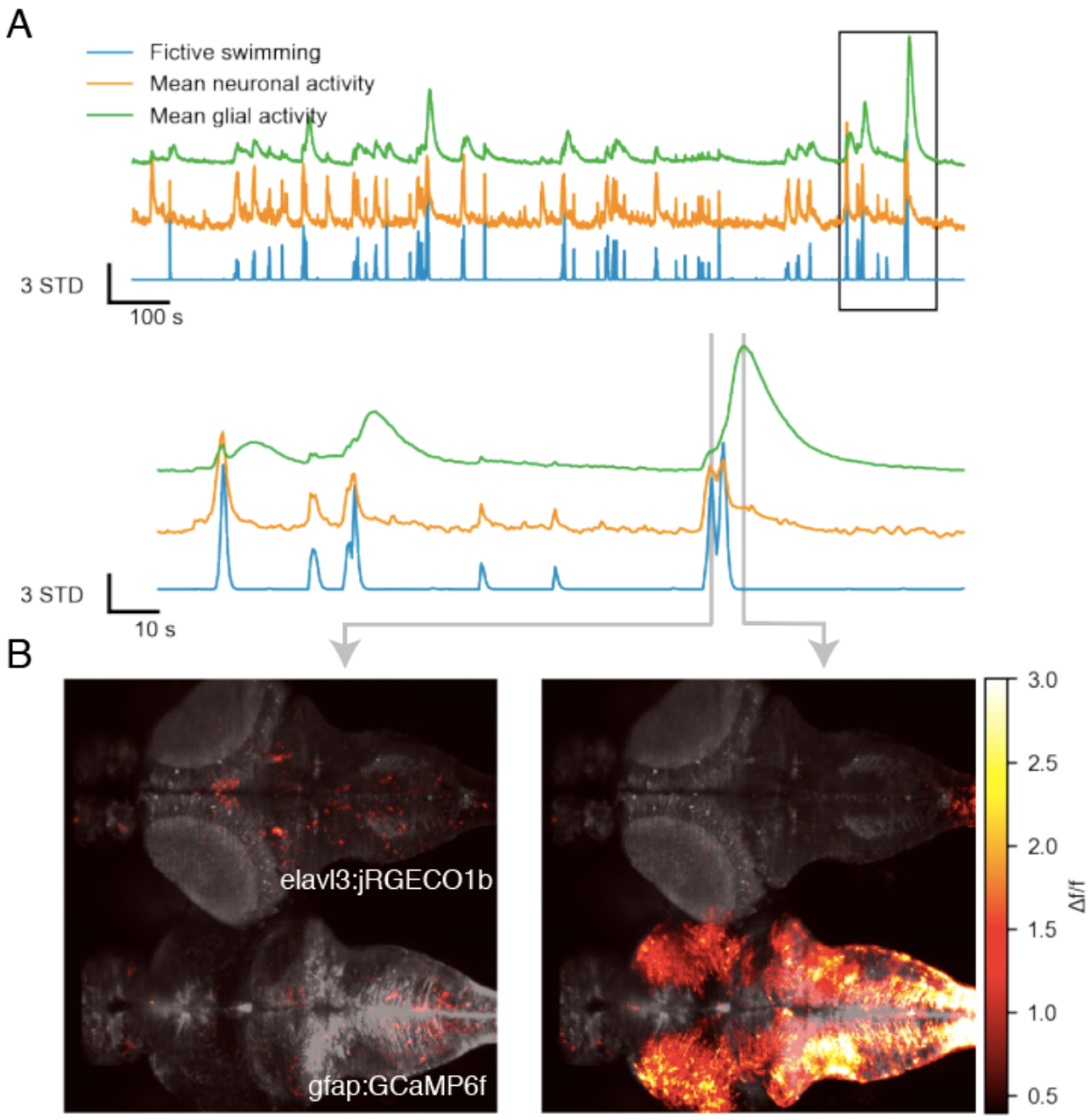

Figure 2.9. Brain-wide astroglial calcium events follow vigorous attempts to swim. Brain-wide astroglial calcium activity in a 6 dpf Tg(*gfap:GCaMP6f;elavl3:jRGECO1b*) was recorded during fictive swimming. **(A)** Dual population imaging of astroglia and neurons during fictive behavior. Colored traces are a timeseries representation of fictive behavior, mean neuronal calcium activity, and mean astroglial calcium activity, all z-scored to share the same y axis. Population neuronal activity is tightly correlated with fictive behavior, while population astroglial activity is slower (lagged relative to behavior) and more variable than neuronal activity. An enlarged portion of the timeseries (bottom row) shows that astroglial responses during locomotion are weak, but after a fraction of vigorous behavioral epochs, astroglial responses are very strong, with a long duration

Figure 2.9 (continued) (~10s). **(B)** Maximum intensity dorsal-ventral projections of single timepoints of the imaging data that generated the timeseries in (A). Dual-color imaging is implemented by projecting a green image and a red image onto two halves of the camera chip, hence the appearance of two brains. Astroglia are sparsely active during locomotion; shortly after locomotion, astroglia across the brain are potently excited. At the same time, neuronal calcium activity is quiescent.

Across several animals, we found that brain-wide astroglial calcium events (as measured by the population mean of all astroglia) were highly variable in their amplitude (Fig. 2.10A), but their timing was quite consistent: astroglial population activity trailed the population mean activity of neurons with a ~5s lag (Figure 2.10B). The duration of these brain-wide events depended on the amplitude, as expected if the calcium concentration within a cell decays exponentially; across fish it was typical for astroglial calcium levels across the brain to remain elevated for 5-10s (Fig. 2.10A) during a brain-wide event. During this time, neuronal activity was largely quiescent. Together, these results reveal a link between the behavioral state of larval zebrafish and brain-wide "astroglial tone".

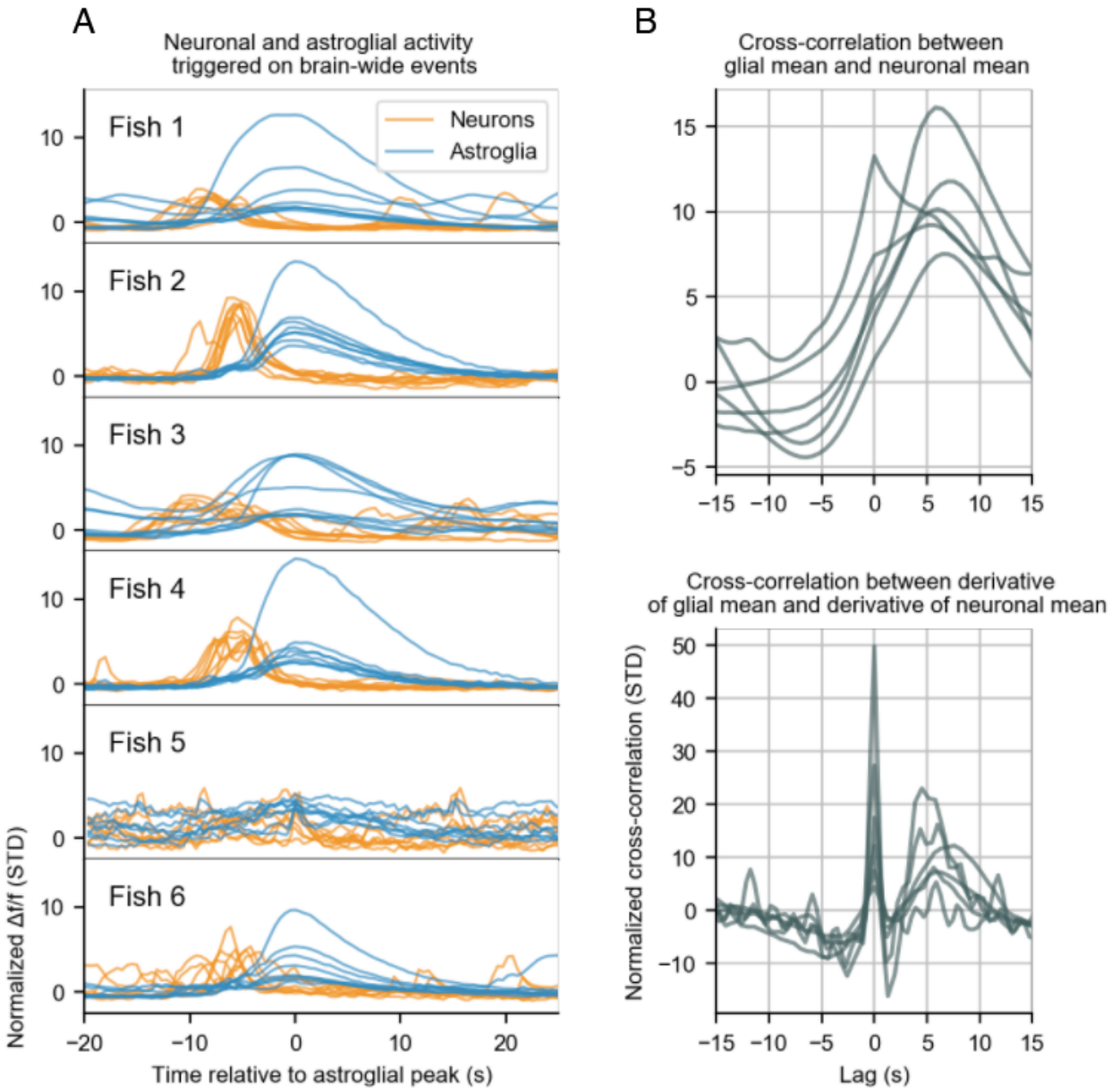

Figure 2.10. Astroglial population activity lags neuronal activity.
(A) Z-scored Mean astroglial and neuronal activity from several Tg(*gfap:GCaMP6f;elavl3:jRGECO1b*) fish, triggered on brain-wide events. Brain-wide events were detected by finding peaks in mean astroglial activity. In all animals except fish 5, this technique identified brain-wide astroglial events that were reliably preceded by peaks in mean neuronal activity, which is a proxy for fictive locomotion (Fig. 2.9A). As noted in Figure 2.7B, there is substantial variability in the amplitude of brain-wide events, which corresponds to variation in the fraction of astroglia excited during the event. By contrast, locomotion-related neuronal activity is much less variable. Locomotor output appears suppressed during elevated astroglial calcium activity. **(B)** Cross-correlation analysis of mean astroglial activity and mean neuronal activity across

Figure 2.10 (Continued) same population of animals that sourced the data shown in (A). Additionally, the cross-correlation between the first temporal derivatives of the astroglial means and neuronal means was taken in order to detect alignment of rise times between the two cell populations (bottom). In both cross-correlations, the peak alignment between the neuronal and astroglial signals is ~5s. The cross-correlation of derivatives reveals a strong peak at 0s lag which corresponds to weak astroglial responses to fictive locomotion seen in 2.9A. These signals may originate from astroglia or anomalous GFAP+ cells discussed earlier in the chapter.

Discussion

Astroglial cells in zebrafish and other non-mammalian vertebrates have historically been studied chiefly for their role in neurogenesis. The goal of this chapter has been to argue that larval zebrafish astroglia may also be involved in neuronal circuit function. To advance this argument, we provided anatomical and functional imaging evidence from astroglia to reveal multiple points of homologous structure and function between astroglia in larval zebrafish and astrocytes in mammals.

Anatomy

I first presented anatomical data which showed that larval zebrafish astroglia have a radial morphology with extensive ramifications in neuropil. The radial morphology is a hallmark of a neurogenic brain, as newborn neurons use radial glial fibers as a scaffold for migration (Rakic 1978). We postulate that the fine ramifying processes we observed are functionally homologous to a similar morphology observed in mammalian astroglia, which fill the extracellular space around neurites and allow astroglia to sense and influence neuronal activity (Shigetomi et al. 2016). Our use of light microscopy in this work limited the effective spatial resolution of our imaging; thus, we could not observe these ramifications, or putative astroglial-neuronal contacts, at the synaptic scale. Nanometer-resolution imaging with electron microscopy and subsequent dense

reconstruction of larval zebrafish astroglia would be a valuable approach for fully resolving the morphology of these cells; this technique has been successfully applied in a small region of mouse cortex (Kasthuri et al. 2015), and doing the same for a portion of the larval zebrafish brain would allow a better comparison of astroglial morphology in fish and mice.

Spontaneous events

After a describing the gross and fine anatomy of zebrafish astroglia, we used volumetric calcium imaging to observe spontaneous and evoked calcium activity in these cells. The "spontaneous" calcium activity we observed is almost certainly not literally spontaneous—such events must be caused by something, likely an extracellular cue. Furthermore, we observed that these events could propagate within and between cells in a complex manner. Similarly complex calcium activity has been observed in in mouse astrocytes: mouse astrocytes respond to a variety of extracellular cues, and the dynamics of these calcium events vary across cellular compartments within a single cell (Verkhratsky et al. 2012; Volterra et al. 2014; Bazargani and Attwell 2016). Resolving which cues are driving and shaping calcium events in zebrafish astroglia requires experiments where the chemical composition of the extracellular and intracellular space can be carefully controlled, e.g. whole-cell recordings in a brain slice preparation, a standard technique for studying astrocytes in mice. Developing these techniques for larval zebrafish will be crucial for gaining molecular insight in astroglial calcium signaling in these animals.

Evoked brain-wide events

We observed that astroglia across the brain responded with intense calcium activity after certain behavioral events. Phenomenologically, these brain-wide events resemble spatially propagating calcium waves observed *in vitro* radial glia and mouse astrocytes (Newman and Zahs 1997; Weissman et al. 2004), as well as coordinated excitation of astrocytes and Bergmann glia observed *in vivo* (Paukert et al. 2014). The latter phenomenon is perhaps most relevant for the work presented here. The coordinated excitation of the two astroglial populations (astrocytes in visual cortex and Bergmann glia in cerebellum) was found to be driven by release of the neuromodulator norepinephrine, and under specific (mildly aversive) behavioral conditions. The next chapter will explore in greater detail the possibility that noradrenergic release is responsible for large-scale calcium events in astroglia.

Materials and methods

Fish lines

Zebrafish larvae were reared at 28.5 C in a 14 hour-10 hour light-dark cycle. Zebrafish from 5 to 7 days past fertilization (dpf) were fed cultured rotifers and used for experiments. All experiments complied with protocols approved by the Institutional Care and Use Committee at Janelia Research Campus (JRC). Animals' sex was unknown. Transgenic zebrafish larvae were in *casper* or *nacre* background (White et al. 2008). Tg(*elavl3:GCaMP6f*), Tg(*elavl3:H2B-GCaMP6f*), and Tg(*elavl3:jRGECO1b*) lines have been previously described (Chen et al. 2013; Dana et al. 2016; Dunn et al. 2016; Vladimirov et al. 2018). The Tg(*gfap:jRGECO1b*), Tg(*gfap:GCaMP6f*), Tg(*gfap:H2B-*

GCaMP6f), Tg(*gfap:tdTomato*), lines were generated with the Tol2 system (Urasaki and Kawakami 2009) and a known GFAP sequence (Bernardos and Raymond 2006).

Confocal imaging

Confocal images were acquired on Zeiss LSM 710 and 880 microscopes in the JRC core facility. For all images, the detection objective was parallel to the dorsal-ventral axis of the fish brain.

Color-coded depth projections

Several figures use color-coded depth projection images, which combine a maximum or mean intensity projection with color channel that encodes a third dimension (e.g., spatial depth or time). In both the maximum and mean projections, the source data (a 3-dimensional array of scalars) is transformed into a colorized image (a 2-dimensional array of RGB vectors). Indices along the projection axis (the axis lost in the transformation) are mapped to a smoothly varying colormap. In the case of the color-coded maximum projection, these RGB values represent the index along the projection axis where pixel attained its maximum value. These RGB values are then scaled by the maximum intensity value. Thus, for each pixel in the final depth-projected image, the color and the brightness of that pixel depends only on the intensity and index along the projection axis of the brightest values in the original data. This type of depth projection is best suited for sparse, non-overlapping intensities. By contrast, the depth-coded mean intensity projection generates meaningful output for non-sparse, overlapping intensity data. For the color-coded mean projection, each scalar in the original image is replaced by an intensity-weighted RGB vector and the resulting volume is mean-

projected. Thus, for each pixel in the final image, the color and intensity of that pixel represents an aggregation along the projection axis of all color-coded intensities in the original data.

Light sheet microscopy

All animals in fictive-behavior experiments were paralyzed and restrained. To induce paralysis, we bathed fish in a 5 mg/ml solution of the nicotinic acetylcholine receptor antagonist α-bungarotoxin for 30 seconds. Once fish no longer responded to tactile stimuli, we transferred them to a custom-fabricated sample holder. Paralyzed fish were then immersed in low-melting point agarose (Sigma) and oriented before the agarose congealed. Paralyzed zebrafish were mounted on an acrylic pedestal inside a square water-filled chamber with glass walls and a diffusive screen at the bottom for stimulus projection. Agarose was removed from the head and tail, and large-barrel glass pipettes (~40 μm inner diameter) were attached to the tail with gentle suction. Signals from the two electrodes were amplified, digitized, and read by our behavioral control software; routines within the software then calculated the standard deviation of each signal in a sliding window of 10 milliseconds: this formed the 'swim signal' or 'swim power' used for quantification of behavior.

In VR experiments, the visual stimulus was a stripe pattern (2.5 mm stripe width) which was projected underneath the fish with a video projector (MP-CD1, Sony). This pattern moved forward at a speed of 2.86 mm/s (typical) when the fish was not swimming. When the fish swam, the stripe accelerated backward at a rate proportional to swim power, with $velocity = -motosensory\ gain * swim\ power$. This visual feedback mimics

the visual feedback the animal would receive if it were freely swimming. When swim power is 0, the constant forward velocity of the visual stimulus mimics the visual scene a fish would observe were it moving backward (as in a virtual water stream). In open loop, the gain was zero, so the stripes moved forward at a fixed velocity whether or not the fish swam.

Nervous system imaging during fictive behavior was performed with a custom light sheet microscope, as previously described (Vladimirov et al. 2014). Volumetric imaging was performed at a rate of 1.5-2.5 Hz, depending on the brightness of the fluorophore being imaged and the density of axial sampling. For GCaMP6s/f imaging, a 488 nm laser was used for excitation; a 525/50 nm filter (Semrock) was used for filtering fluorescence emission, and the visual stimulus was presented with red light. For jRGECO1b imaging, a 561 nm laser was used for excitation; a 630/92 nm filter (Semrock) was used for filtering fluorescence emission (Semrock), and the visual stimulus was presented with blue light. For two-color imaging, 488 nm and 561 nm lasers were used simultaneously. An image splitter (W-View Gemini, Hamamatsu) separated the green and red fluorescence (with a 525/50 nm detection filter (Semrock) for green emission and a 645/75 nm detection filter (Chroma) for red emission); red and green images were recorded on opposite halves of the same camera chip.

Light sheet data processing

Raw light sheet microscopy data were filtered plane-by-plane with a 1.2 x 1.2 micron-wide median filter to remove single-pixel noise on the CMOS camera chip. For motion correction, a reference volume was created by taking the mean of the middle 10

timepoints in the dataset; all volumes were registered to this reference volume by estimating a 2-dimensional translation transform that maximized the overlap between the timepoint and the reference image. Why estimate a 2-dimensional transform? Although our data are 3-dimensional, our sampling is anisotropic: the sampling along the lateral axes (x and y) is much denser than the sampling along the remaining axis (z). Because of our sparse sampling in z, correcting for z motion by interpolation is not possible, and thus we manually discarded experiments with too much motion in z. After motion correction, the baseline fluorescence was estimated by smoothing each pixel's time series with a sliding-window percentile filter that estimated the 20^{th} percentile of the data in 5-minute windows. $\Delta F/F$ was then calculated for each pixel's time series (after subtracting the camera offset, which is ~100) by subtracting the baseline from the raw time series and dividing this difference by the baseline plus an offset of 10, to prevent division by baseline values very close to 0. The addition of an offset to the denominator of the $\Delta F/F$ calculation underestimates true $\Delta F/F$ but reduces the probability of artifacts caused by normalizing pixels with baselines near 0.

Chapter 3: A noradrenergic error signal acts through astroglia to suppress futile behavior

Abstract

When goal directed behavior repeatedly fails, it can be advantageous to reflect on these failures and try a different strategy. We recapitulated this phenomenon in a virtual reality paradigm for larval zebrafish. In our paradigm, fish received a constant drive to swim, yet received no visual feedback from their actions. This experience of motor futility, i.e., repeated actions with no sensory feedback, caused fish to alternate between active and passive behavioral states, characterized by vigorous efforts and quiescence, respectively. In order to understand how the nervous system generates this response to behavioral futility, we used brain-wide functional imaging to record calcium signals from the whole nervous system—neurons and astroglia—in animals as they alternated between active and passive states. We identified a population of astroglia in the hindbrain that appear to drive the transition from active to passive behavioral states; we subsequently identified hindbrain noradrenergic neurons that provide excitatory input to these astroglia, and GABAergic hindbrain neurons that receive excitatory input from the astroglia. We compose these observations together in the following model: noradrenergic neurons respond to motor actions that fail to elicit visual feedback; this error signal is temporally integrated by astroglia, which, through some unknown mechanism, excite GABAergic neurons that suppress motor output. In this way, the fish can infer that its recent actions are futile and adapt its behavioral strategy. This chapter presents published work (Mu et al. 2019).

Introduction

Goal-directed behaviors, especially movements, are often continuously adjusted by feedback (Lackner and Dizio 2017). If an agent observes that an action fails to match the target of that action, the agent can use this error signal to update subsequent actions. But what should an agent do if its goal-directed actions continuously fail? This question naturally arises in the context of locomotor behavior: inability to move is a life-threatening risk for most motile animals, and an animal's ability to move is largely determined by the animal's environment, over which the animal has limited or no control. Terrestrial animals can be stuck in mud or water; aquatic animals can be washed onto land; many predatory strategies hinge on restricting a prey animal's locomotion so that prey can be summarily ingested.

These are real challenges for almost any motile animal, so we expected that we could use the larval zebrafish as a model organism for understanding how animals respond when their actions are futile, and how the nervous system coordinates this response. Like many fish, larval zebrafish swim forward in response to forward optic flow. This behavior, called the optomotor response (OMR), helps fish stabilize their position in space by cancelling externally-generated displacement with internally-generated locomotion (Rock and Smith 1986). The OMR is sufficiently robust that larval zebrafish will perform this behavior in a simple virtual reality (VR) paradigm wherein a fish is paralyzed and its motor commands are inferred by electrophysiological recording of motor neurons in the tail musculature (Ahrens et al. 2012). A visual stimulus, e.g. forward drifting gratings, is shown to the fish, which evokes an attempt to swim; the

corresponding swim signal is used to translate the visual stimulus as if the fish had moved.

The use of virtual reality enables two experimental opportunities: first, virtual reality experiments allow very tight control over what the animal sees, and how its actions affect what it sees; second, virtual reality behavioral paradigms are compatible with mechanistic physiology experiments, e.g. imaging the nervous system at cellular resolution. We leverage both of these opportunities here.

VR paradigms for studying sensorimotor processing in larval zebrafish have a parameter called the *gain* of the virtual reality, which determines how much the visual stimulus moves as a function of the vigor of the animal's motor output. In order to observe how fish respond when their actions are futile, we designed a very simple VR paradigm where the fish sees constant forward gratings (to engage the OMR) but the gain of the VR is 0, i.e. the visual stimulus is in "open-loop". We observed that fish in open-loop alternated between two apparent behavioral states: an "active" state, characterized by frequent, vigorous attempts to swim, and a "passive state, where the fish made no attempts to swim.

We next wanted to know how this behavior is generated by the nervous system. Our intuition in this area was guided by the fact that, at a coarse level, the fish adopting a passive state resembled the canonical response of rodents observed in a class of assays that evoke behavioral passivity by inexorable, aversive stimuli, such as the forced swim test (Porsolt et al. 1979) and the tail suspension test (Steru et al. 1985). The behavioral responses of rodents in these assays are sensitive to drugs that alter

the function of neuromodulators, in particular norepinephrine (NE), so we became interested in whether the noradrenergic system and its targets could be involved in the behavioral bi-stability we observed in larval zebrafish in open-loop. In mammals, NE potently excites astrocytes (Bekar et al. 2008; Paukert et al. 2014); astrocytes have also been implicated in state-dependent modulation of neuronal circuits (Wang et al. 2012; Poskanzer and Yuste 2016). Accordingly, we decided to consider astroglia as well as neurons in our search for mediators of the behavioral state switch. As shown in Chapter 2, zebrafish astroglia engage in extensive calcium signaling, thus, calcium imaging is a promising means of observing astroglia activity. In order to image calcium activity in astroglia or neurons (or both at once, using spectrally separated calcium indicators), we used volumetric light-sheet microscopy to record neuronal and glial calcium activity across the brain in larval zebrafish as they alternated between active and passive behavioral states.

Our first finding from these imaging experiments was a population of astroglia projecting to the lateral medulla oblongata (L-MO) with calcium activity that peaked when the animal transitioned from active to passive states. We subsequently performed a range of bidirectional perturbation experiments which strongly suggested that calcium signals in these L-MO-projecting astroglia are necessary and sufficient for the animal to transition active to passive behavioral states. Our neuronal imaging data suggested that a population of hindbrain noradrenergic neurons may excite the L-MO-projecting astroglia, and subsequent perturbation experiments confirmed this. Refined imaging experiments suggested that these noradrenergic neurons encode a sensorimotor error

signal, i.e. the mismatch between motor output and expected visual stimulus. When we combined optogenetic stimulation of astroglia with calcium imaging of neurons to find cells “downstream” of the L-MO astroglia, we identified a population of GABAergic neurons that we believe are sufficient for suppressing motor activity. Taken together, we propose that a circuit composed of neurons and glia detects behavioral futility and drives the transition from active to passive behavioral states in open-loop conditions.

Results

Futile fictive fish behavior in open-loop virtual reality

To study how fish respond when their actions are futile, we modified a VR behavioral paradigm previously used for studying short-term motor learning (Portugues and Engert 2011; Ahrens et al. 2012). In this paradigm, paralyzed fish are shown a forward-drifting grating, which evokes the OMR (Baier et al. 2000). In closed-loop mode, fish have partial control over the visual environment insofar as their actions (inferred via recordings of motor neurons in the tail musculature) generate visual feedback, while in open-loop mode the animals have no control and thus their actions are futile (Fig. 3.1A). The difference between closed-loop and open-loop VR can be parametrized by the gain of the VR, which is a number in arbitrary units that indicates the scaling between the animal’s fictive actions and the visual feedback those actions generate; when gain is 0, the VR is open-loop. In closed-loop, fish exhibit regular motor output, with a bout rate of ~1 Hz, and with stable power per swim bout, as evinced by a sample trace from an example fish (Fig. 3.1B). This fictive locomotion is consistent with behavior observed in free-swimming fish performing the OMR (Budick and O’Malley 2000; Severi et al. 2014;

Dunn et al. 2016). In open-loop, however, the vigor of the swim bouts increased, leading to an extended epoch of high-vigor swim bouts, which we call an “active” state. After some time, the fish abruptly stopped swimming for an extended epoch, which we termed a “passive” state (Fig. 3.1B). Fish alternated between active and passive states for the duration of open-loop (Fig. 3.1C, Fig. 3.1D). Fish recovered a normal swim pattern if closed-loop was restored (Fig. 3.1C), which indicates that the alternation between active and passive states observed during open-loop was a direct and reversible consequence of the loss of visual feedback.

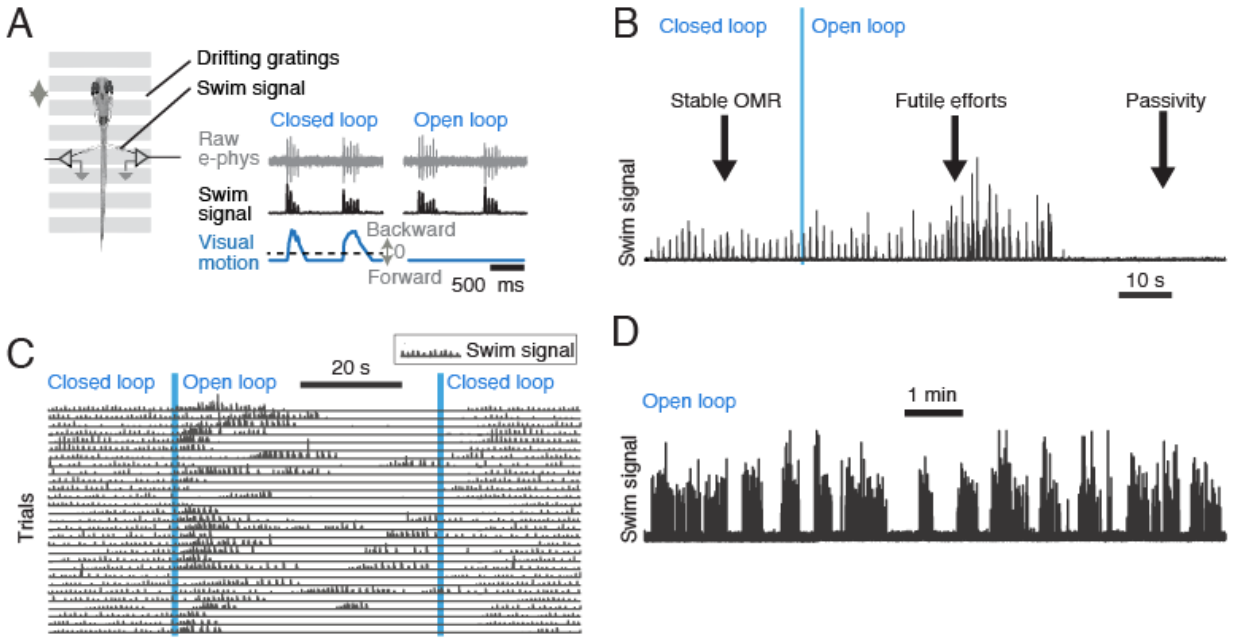

Figure 3.1. Open-loop VR induces alternating active and passive behavioral states in larval zebrafish.
(A) A schematic of the VR system. Paralyzed larval zebrafish are positioned above an image of alternating dark and light bars which passively drifts forward. This whole-field motion induces the fish to swim, and these efforts are recorded via suction electrodes attached to the tail of the animal. In closed loop, the swim signal is used to drive the visual stimulus backwards, matching the visual scene the animal would see if it swam forward. In open loop, this visual feedback is absent. **(B)** Fictive swim signal of an example fish performing the OMR at the transition from closed loop to open loop. In closed loop, the behavior of the animal is stable; in open loop the swim signal indicates

Figure 3.1 (continued) that the animal's attempts to swim with increasing vigor before ceasing all efforts and entering a passive behavioral state. **(C)** After the fish becomes passive due to open loop, the motor pattern of the fish returns to normal over many trials if closed-loop control is restored. **(D)** In open loop with constant forward gratings, the fictive swim signal from an example fish shows that the animal alternates between active and passive behavioral states.

Our belief that the active and passive behavioral states constituted two distinct modes of behavior was bolstered by our observation that in some fish the distribution of inter-swim intervals (ISI) in open-loop was bimodal, with a narrow peak around 1 seconds, corresponding to the short interval between swims in active states; and a wide peak above 5 seconds, corresponding to the long gap between swims that defined the passive state (Fig. 3.2A, Fig. 3.2B). With a hand-picked threshold of 5 seconds, we used the ISI to classify an epoch as an active state (an epoch when the ISI is less than 5 seconds) or a passive state (any ISI with length greater than 5 seconds) (Fig. 3.2A). Over 74 fish recorded in the open-loop paradigm, the typical active state lasted 34.2 ± 3.4 seconds and the typical passive state lasted 22.8 ± 2.5 seconds (mean ± S.E.M) (Fig. 3.2C).

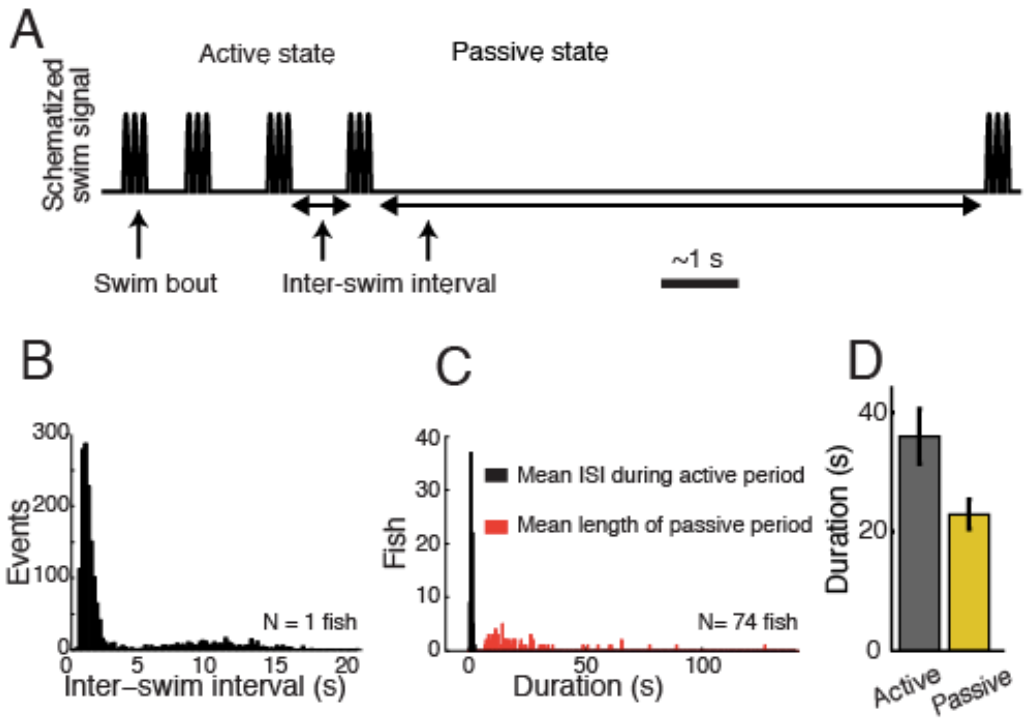

Figure 3.2. Open-loop VR induces bi-stable fish behavior.
Quantifying the distribution of active and passive states induced by open loop VR. **(A)** Cartoon illustrating the parameters of the swim signal that are relevant for subsequent quantification of fictive fish behavior. Larval zebrafish locomotion in the OMR is saltatory: fish engage in “swim bouts”, which are short (200-500 ms) sequences of attempted movements, and this is recapitulated in the fictive swimming preparation. Swim bouts are separated by a pause, typically on the order of 1s, which we call the “inter-swim interval”, or ISI. In the active state, the ISI interval is short, but it lengthens during the passive state. Thus, the passive state can be thus operationally defined as an unusually long ISI. **(B)** Distribution of inter-swim intervals from an example fish performing fictive swimming in open loop. The peak around 1s corresponds to intervals between swims that occurred while the fish was in the active behavioral state, while the much wider peak above 5s corresponds to the duration of passive states. **(C)** Population data showing the mean ISI of active states and the mean duration of passive states (after applying a threshold of 5s on the ISI) per fish. **(D)** The mean duration of the active state and passive state across animals. Error bars are ± SEM for all figures unless otherwise indicated.

We next examined the finer structure of the behavior in the active state leading up to the onset of passivity, hoping to find some changes in motor behavior that could allow us to sharpen our nascent hypotheses about the neural basis of the behavioral state switch.

We found that in the last few swim bouts before passivity, fish attempted to swim more vigorously (Fig. 3.3A). Additionally, the ISI increased leading up to passivity (Fig. 3.3B); fish also attempted to make more turns before becoming passive (Fig. 3.3C). Taken together, our analyses of futile fictive fish behavior in the active state show that the transition from active to passive states is anticipated by gradual changes in the motor pattern of the fish—swim vigor and ISI increase, and fish attempt to turn more before becoming passive.

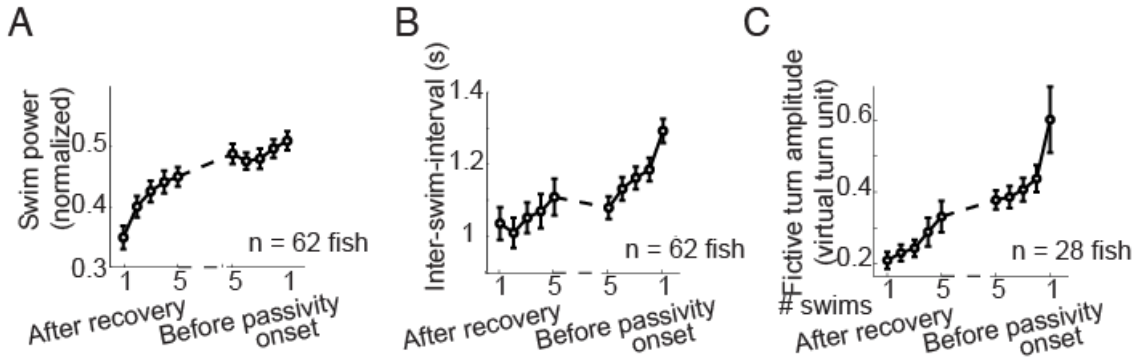

Figure 3.3. Evolution of fictive locomotion leading up to passivity in open-loop VR. The x-axis of each plot is the Nth swim bout after or prior to passivity. **(A)** Mean swim power per swim bout increases leading up to passivity. **(B)** Mean ISI increases leading up to passivity. **(C)** Mean fictive turn amplitude (estimated by comparing the fictive swim signal from the left and right suction electrodes) increases leading up to passivity.

Because we observed heightened motor vigor leading up to passivity and because we assumed that fish would find open loop aversive, we checked whether the onset of passivity was preceded by struggles. Struggles are characterized by forceful tail undulations which propagate in a caudal-to-rostral direction (reversed relative to forward swimming) and serves to propel the fish backwards (Liao and Fetcho 2008). We did not find evidence that the onset of passivity is typically preceded by struggles (Fig. 3.4A, C).

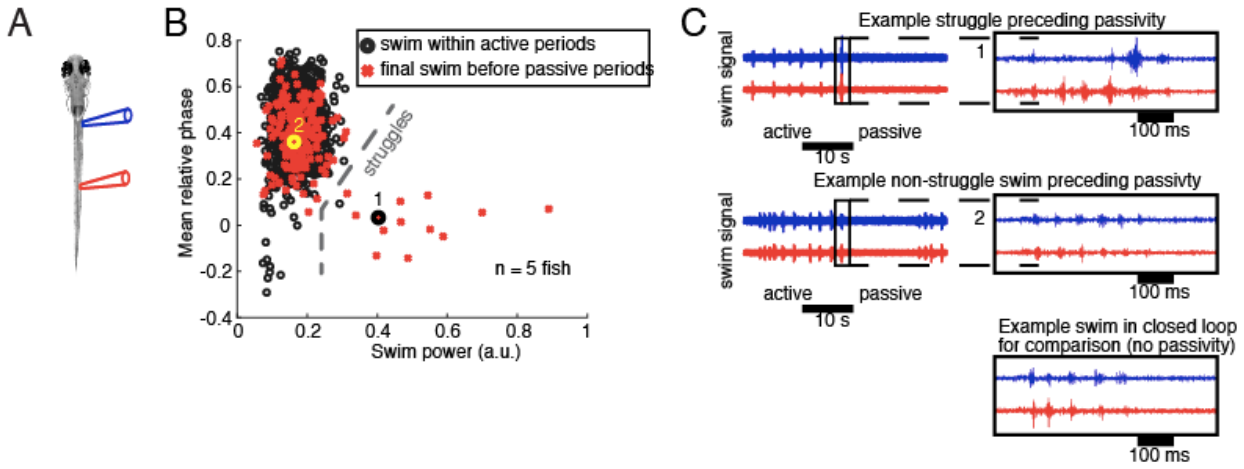

Figure 3.4. Passivity is not always preceded by a struggle.
(A) Schematized experimental setup for detecting struggles. Two suction electrodes are positioned on the same side of the fish, thereby enabling detection of the struggles by measuring the relative phase of fictive swimming in different muscle segments. **(B)** Struggles can be identified by the relative phase difference between anterior and posterior electrodes, and power per burst. Final swims before passivity can be non-struggle swims or struggles. On average 13 ± 9 % of switches are preceded by a struggle. **(C)** Example of state switches preceded by a struggle (top), non-struggle swim (middle), and for comparison, closed-loop swimming (bottom).

The terms “active state” and “passive state” are unfortunate insofar as they encourage unwarranted assumptions about the global behavioral state of the animal. In the data we present here, we assess the activeness and passiveness of an animal by binarizing one kind of behavior (swimming), but our experimentally expedient use of paralysis prevents us from observing other behaviors, such as jaw or eye movement, which may become more frequent when the fish ceases locomotor output. The most direct approach to assay a more complete behavioral repertoire of our animals would be to implement our open-loop assay in a VR paradigm for unparalyzed fish, as other research groups have done for optomotor behavior (Jouary et al. 2016; Orger and Portugues 2016). This would allow us to monitor a much larger set of behaviors with higher resolution without sacrificing the benefits of VR experiments. In lieu of a new

paradigm, we can attempt imperfect inferences about hidden behaviors via functional imaging. Specifically, we hypothesized that fish in the open loop paradigm would engage in a higher rate of spontaneous eye movement during passivity. This would be consistent with a theory wherein fish use an epoch of behavioral passivity as an opportunity to make observations of their environment without interference from vigorous actions. We imaged the calcium activity in neurons in the abducens nucleus, a brain region that coordinates movement of the eyes, in a single fish in our open-loop VR. We observed suppressed abducens activity during active states and elevated abducens activity during passive states (Fig. 3.5), which is consistent with the theory advanced above.

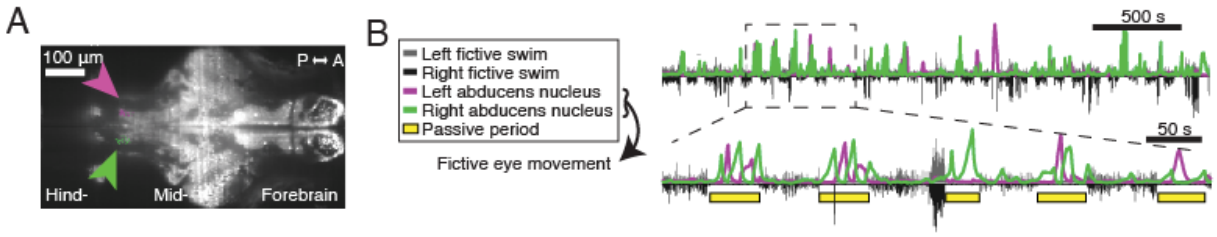

Figure 3.5. Fish attempt eye movements while passive.
(A) During passive periods, calcium activity was seen in neurons in the abducens nucleus (arrows) in animals expressing nuclear-localized GCaMP6f (Tg(*elavl3:H2B-GCaMP6f*)) imaged with a light-sheet microscope. Neurons in the abducens nucleus are known to drive eye movement (Schoonheim et al. 2010). **(B)** Increased activity in this area, alternating the between left and right aspects of the abducens nucleus, implies that animals were attempting to move their eyes during the passive periods.

Calcium imaging reveals a population of astroglia excited at the onset of behavioral passivity

In order to search for the cellular basis underlying the alternation between active and passive behavioral states, we turned to brain-wide functional imaging light sheet microscopy. This technique allows us to image calcium dynamics in neurons and

astroglia across the brain at ~2.5 whole-brain volumes per second while animals perform fictive behavior in a VR (Vladimirov et al. 2014). A 2.5 Hz volumetric sampling rate is slow compared to rapid changes in brain activity, which may occur on the timescale of milliseconds (Budick and O'Malley 2000; Faber et al. 2006), but since the alternation between active and passive states occurs on the timescale of tens of seconds, we believed that we could still resolve the underlying changes in brain activity at this relatively low temporal sampling rate. Specifically, we suspected that the transition from active to passive behavioral states was driven in part by some integrative process which occurred on the timescale of seconds, and this phenomenon should be easily detectable at a relatively low temporal sampling rate.

We imaged calcium activity in neurons, as labelled by calcium indicators expressed under the control of the neuronal promoter Elavl3 (Park et al. 2000), and astroglia, as labelled by calcium indicators expressed under the control of the astroglial-specific promoter GFAP (Bernardos and Raymond 2006). For experiments in which we wanted to observe astroglial and neuronal activity simultaneously, we created double-transgenic fish which expressed green and red calcium indicators in neurons and astroglia, and we imaged these animals using a commercial dual-color detection assembly.

We made our first observations at a relatively low level of detail—we used dual-population imaging to look at the average calcium activity of all astroglia and all neurons as the fish transitioned from active to passive behavioral states. Unsurprisingly, population neuronal activity was highest when the animal was most active, and comparatively low when the animal was in the passive state (Fig. 3.6A). To our surprise,

the trial-averaged population astroglial activity appeared ramp up prior to and peak shortly after the animal entered the passive state (Fig. 3.6A, B). This was our first indication that astroglia may play some role in the transition from active to passive behavioral states.

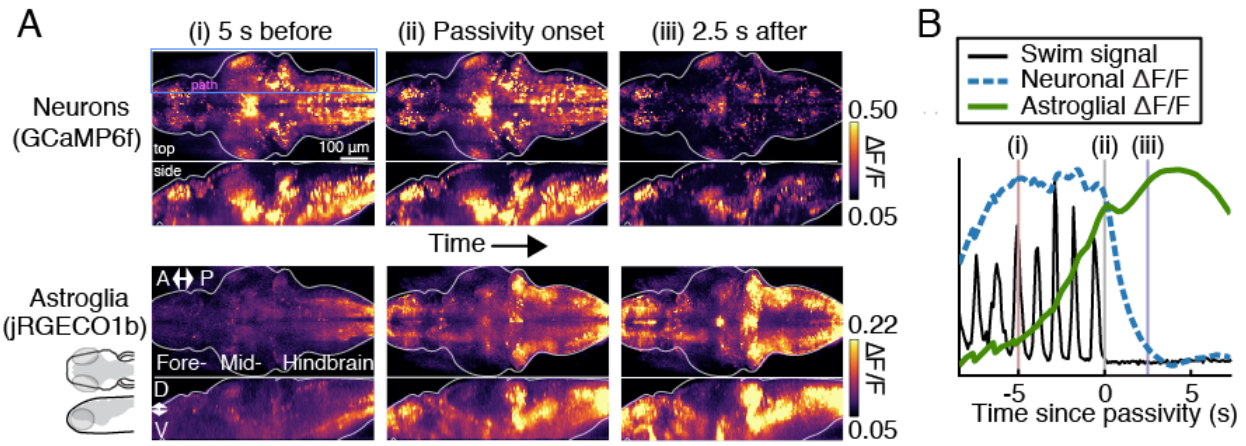

Figure 3.6. Simultaneous imaging of astroglia and neurons reveals distinct dynamics around the onset of passivity.
(A) Maximum depth- and side-projections of sample timepoints from the passivity-triggered average. Neurons express GCaMP6f, and astroglia express JRGECO1b, enabling simultaneous readout of the activity levels of both populations. Bulk neuronal calcium activity is correlated with fictive swim vigor and thus highest leading up to the onset of passivity (i-ii). During passivity, a few neuronal populations are active, but the brain is largely silent (iii). By contrast, bulk astroglial activity climbs at the onset of passivity (ii) and peaks shortly after (iii), with particularly high activity in the medio-dorsal aspect of the hindbrain. **(B)** Plotting the passivity-triggered mean neuronal and glial calcium activity as a function of time relative to passivity onset. Individual swim bouts are aligned across trials, which induces a time warping effect; the complementary activity profiles of mean neuronal activity (magenta) and mean glial activity (green) are evident.

Trial-averaging glial calcium activity in particular should be considered carefully; as demonstrated in Chapter 2, evoked astroglial calcium events can vary wildly in their magnitude. Such long-tailed distributions of intensities are is not accurately represented by a mean. For any cell type, the averaged activity of all cells is a very coarse level of description—it yields a single timeseries from a diverse population of neurons or

astroglia. Under the assumption that single neurons and single astroglia are the fundamental elements which generate our imaging data, the ideal level of description for an imaging dataset would be to have one timeseries per cell. But we have neither the spatial resolution nor the computational technique required for generating this level of description from functional imaging of all astroglia and all neurons with a cytosolic calcium indicator. To approach a more refined description of the data, we used a matrix factorization approach to segment the data into spatially contiguous collections of pixels with similar temporal dynamics. By aggregating pixels into “superpixels”, we greatly reduce the size of a dataset while preserving fine-scale temporal dynamics of interest. This strategy is essentially an application of a standard technique for image segmentation, but in the time domain (Shi and Malik 2000; Felzenszwalb and Huttenlocher 2004). We chose the size of our superpixels to approximately match the assumed size of a cell body. After segmentation, we had a collection of cellular-scale superpixels. This is still a very large dataset, but it was now small enough that we could use it as the basis for inferring functional networks, defined as spatially contiguous collections of superpixels with coordinated activity patterns. In the same way that we used matrix factorization to combine pixels into superpixels based on the similarity of their timeseries, we used matrix factorization again to cluster superpixels into putative functional networks based on their timeseries. In order to make conclusions that could be easily compared across a group of fish, we performed the multiscale matrix factorization on multiple fish, and these fish were registered to a common anatomical atlas; we then screened for putative functional networks that were shared across

multiple fish, and finally we looked at how these putative functional networks responded when fish transitioned from the active state to the passive state. We found multiple putative functional networks that showed consistent activity patterns near the onset of passivity, including neuronal and astroglial networks with elevated activity in the passive period (Fig. 3.7A). We devised a response reliability measure to quantify how consistently each network responded to the behavioral state switch (Fig. 3.7B, right column). This analysis highlighted an astroglial network localized to a gliapil region in the lateral hindbrain, which we termed the lateral medulla oblongata, or L-MO (Fig. 3.7B), wherein calcium activity reliably ramped during active states and peaked at the onset of the passive state.

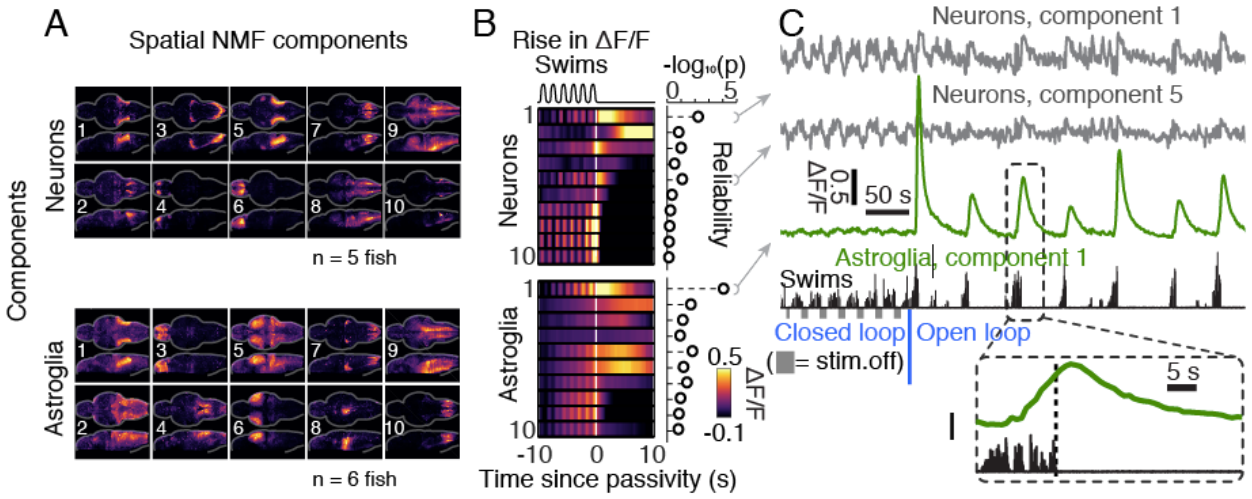

Figure 3.7. Factorization-based analysis of astroglial and neuronal activity at the onset of passivity.
Collectively decomposing the brains of many fish into putative shared functional networks indicates that cells in the lateral medulla oblongata (L-MO) are activated at the transition from active to passive states. This decomposition results in components defined by paired spatial weights and timeseries. **(A)** Spatial weights of functional components estimated by multiscale factorization of functional imaging data. **(B)** Passivity-triggered timeseries of each component timeseries shown in **(A).** As in figure 3.6B, timeseries are triggered on passivity-onset and additionally aligned to individual swim bouts. Both neuronal and astroglial components from the L-MO region respond

Figure 3.7 (continued) very reliably across trials. **(C)** Example traces from the two most reliably-activated components from a fish expressing orthogonal calcium indicators in neurons and astroglia. Astroglial component 1 (localized in the L-MO) in particular appears tuned to the onset of passivity: it is relatively quiescent when the fish is in closed loop, but potently activated when the fish becomes passive in open loop.

Bidirectional perturbation of L-MO-projecting astroglia suggests a causal role in the onset of behavioral passivity

Our analysis of the brain-wide imaging data led us to suspect that calcium signals in astroglia in the L-MO were playing a causal role in the transition from active to passive behavioral states; specifically, we suspected that elevated calcium signaling in these astroglial cells was somehow causing the fish to stop swimming. The ideal experiments for testing this hypothesis require tools for bidirectionally modulating calcium excitability in only the L-MO-projecting astroglia with high temporal precision; unfortunately, tools satisfying these requirements do not currently exist, so we performed a series of perturbation experiments using a variety suboptimal, albeit extant, tools. We started with a series of perturbations designed to extinguish calcium activity in L-MO astroglia, with the hypothesis that these perturbations would subsequently reduce the probability of fish entering the passive state while in open-loop VR, i.e. that astroglial calcium activity is necessary for the active-passive state transition. We assumed that if we killed the astroglia projecting to the L-MO by ablating their cell bodies, then any intracellular calcium signaling in the L-MO will be extinct. We used transgenic animals with a green fluorophore localized to the nuclei of astroglia—*Tg(gfap:h2b-gcamp)*, introduced in Chapter 3—and deployed an ultrafast pulsed laser to ablate the nuclei of L-MO projecting astroglia (Fig. 3.8A) (Tsai et al. 2009). We then compared the behavior of

these animals in the open-loop VR assay before and after astroglial ablation. After astroglial ablation, the amount of time the fish spent in the passive state was reduced by half relative to before ablation (Fig. 3.8C).

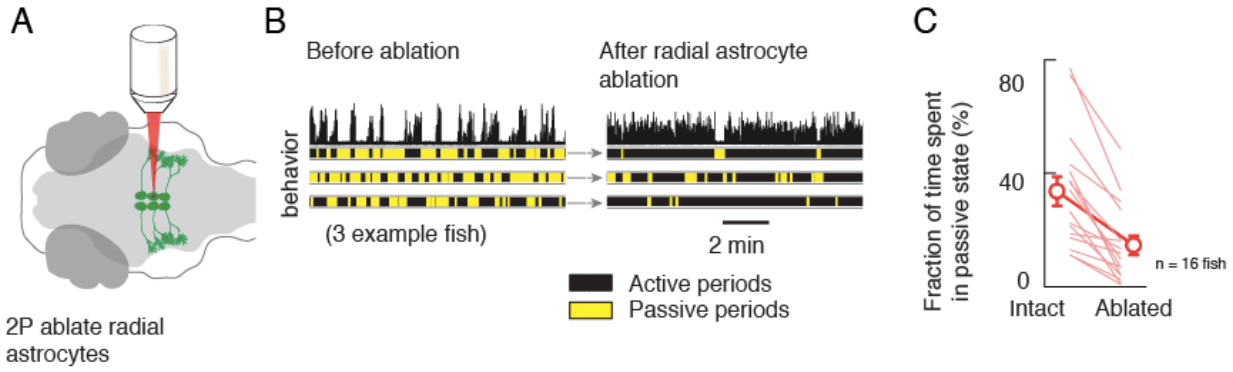

Figure 3.8. Two-photon laser ablation of L-MO-projecting astroglia reduces the incidence of futility-induced passivity.
(A) Cartoon illustrating how nuclear-localized expression of GCaMP6f in astroglial nuclei is used to guide a focused two-photon laser to the somata of L-MO-projecting astroglia. **(B)** Example traces of fictive behavior from three fish in open loop before and after ablation of L-MO-projecting astroglia. After astroglial ablation, fish spend much less time in the passive behavioral state. **(C)** Quantification of the change in passivity induced by astroglial ablation across animals. Astroglial ablation reduces by half the amount of time fish spend in the passive state.

Killing hundreds of cells suddenly (on a cellular timescale) in the central nervous system is likely to have many off-target effects, such as triggering an immune response and possibly damaging untargeted cells. Additionally, astroglia are likely important for maintaining homeostasis of the extracellular space; therefore, abruptly removing astroglia would likely shift or disrupt a wide range of cellular processes. Thus, it is possible that direct side-effects of ablation, or secondary effects due to missing astroglia, could somehow affect neuronal circuits that control motor behavior and thereby generate the post-ablation behavioral phenotype we observed. It is difficult to test this alternative hypothesis directly, so we performed a series of assays designed to

measure whether astroglial ablation caused non-specific changes to the fish's motor behavior. When we measured the behavior of the animals in closed-loop VR after astroglial ablation, we observed normal fictive behavior: after astroglial ablation, fish could still cease swimming when the OMR-inducing stimulus abated (Fig. 3.9A), and fish could still adjust their motor vigor to compensate for changes in the gain of the VR (Fig. 3.9B). We also examined the open-field behavior of unparalyzed fish before and after astroglial ablation, and observed that astroglial ablations had no effect on swim bout frequency or velocity (Fig. 3.8C, D). Furthermore, we compared neuronal calcium activity in the L-MO before and after astroglial ablation, to check whether there were changes in neuronal dynamics in the region directly affected by the loss of astroglia, but we found no detectable difference in neuronal activity (Fig. 3.8D).

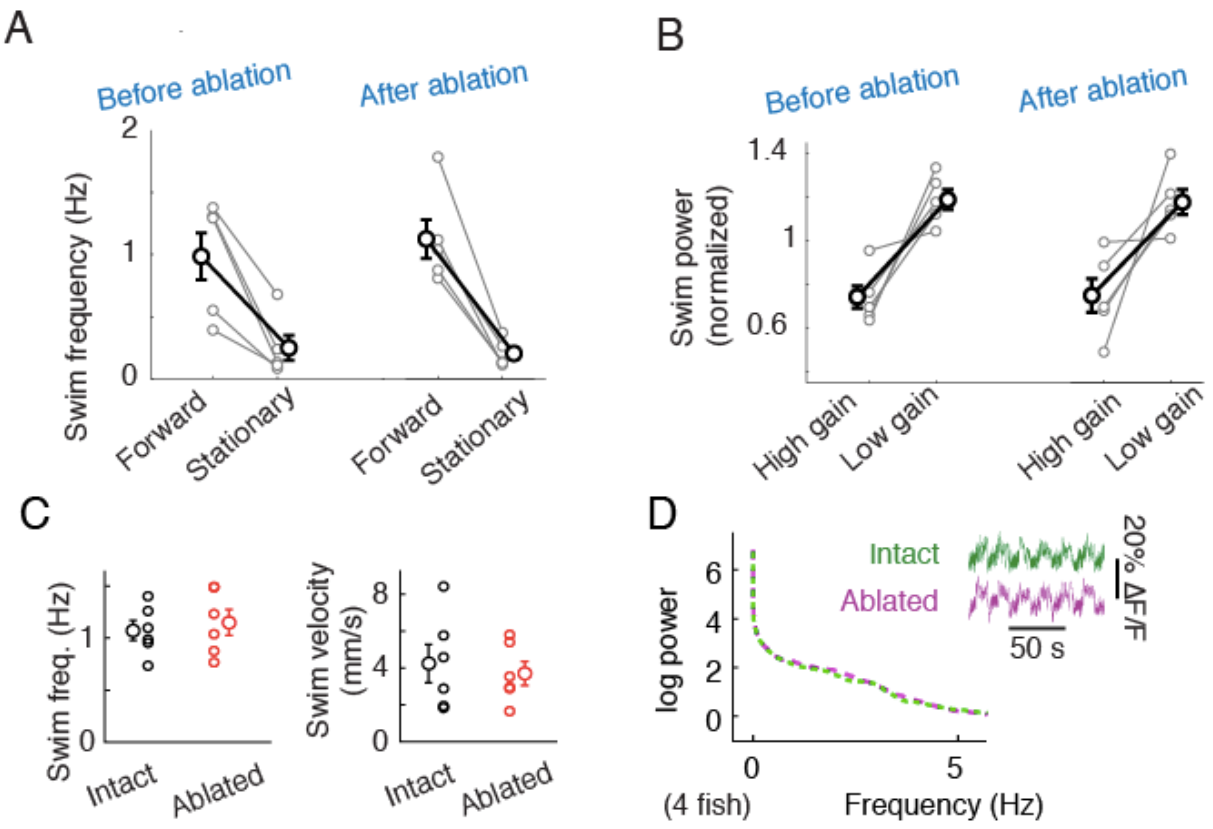

Figure 3.9. Fictive and actual behavioral assays for non-specific alterations of fish behavior induced by astroglial ablation.
(A) If astroglial ablation induced tonic hyperactivity, we would expect to observe that fish with ablated astroglial would have a higher rate of spontaneous fictive swimming, but we do not observe this: fish respond to forward gratings and stationary gratings similarly before and after astroglial ablation, i.e. the fictive optomotor response of these animals is normal. **(B)**. Normal fish in closed loop can tune the vigor of their motor output in response to a changing gain parameter. This form of short-term motor learning is preserved after astroglial ablation. **(C)** In unparalyzed fish swimming in an open field, bout frequency and velocity are unchanged after astroglial ablation. **(D)** Neuronal calcium activity in the L-MO region appears unchanged before and after astroglial ablation.

We also tried a gentler perturbation: in order to specifically block release of calcium from internal stores, we puffed the inositol 1,4,5-trisphosphate receptor (IP_3R) blocker Xestospongin C (XeC) on the cell bodies of L-MO-projecting astroglia. We used calcium imaging of astroglia to observe that XeC application attenuated calcium activity in

astroglia (Fig. 3.10A). Like the direct ablation of astroglia, blocking IP_3R-mediated calcium signaling reduced the amount of time fish spent in the passive state while in open-loop VR (Fig. 3.10B).

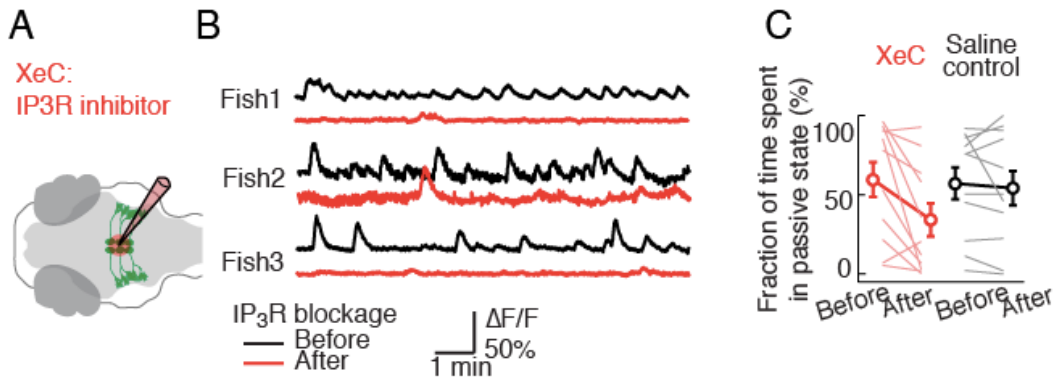

Figure 3.10. Blocking release of calcium from internal stores in L-MO projecting astroglia with an IP3R blocker reduces the fraction of time fish spend in passivity.
(A) Cartoon illustrating how the somata of L-MO-projecting astroglia are targeted with a pipette for local delivery of the IP_3R blocker Xestospongin C. **(B)** Calcium activity in L-MO-projecting astroglia before and after application of the IP_3R blocker. The IP_3R blocker reduces the amplitude and frequency of calcium events in these cells. **(C)** Population data showing that in open-loop VR paradigm, application of the IP_3R blocker reduces the fraction of the time fish spend in the passive state while in open-loop VR.

We next performed as series of perturbations in order to test whether elevating calcium activity in L-MO-projecting astroglia was sufficient to induce a passive behavioral phenotype. We first used a chemogenetic approach to tonically elevate astroglial calcium levels in behaving animals. To perform this manipulation, we expressing the rat TRPV1 channel under the GFAP promoter. Rat TRPV1, but not the endogenous zebrafish TRPV1, becomes highly permeable to calcium when it binds the molecule capsaicin. We used a sparse expression strategy where only a fraction of glial cells expressed the channel because we were concerned that a *gfap*:TRPV1 transgenic might result in neurons expressing TRPV1, which would add a major confound to any

behavioral phenotype observed after TRPV1 activation in these animals. Our sparse expression strategy—injection of Tg(*gfap:jRGECO1b*) embryos with DNA and a transposase—resulted in TRPV1 expression in a fraction of astroglial cells (Fig. 3.12 A).

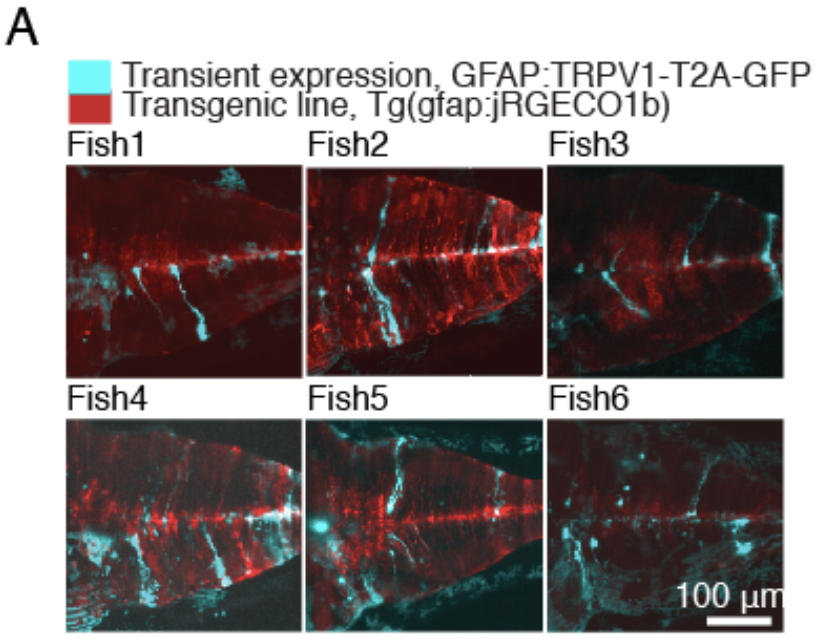

Figure 3.11. Sparse expression of TRVPV1 in astroglia.
(A) Injecting Tg(*gfap:jRGECO1b*) embryos with the *gfap:TRPV1-T2A-GFP* plasmid along with a transposase and screening the larvae for sparse expression yields animals with only a fraction of astroglia expressing TRPV1. jRGECO1b expression is less dense in these animals because the transpose injected with the TRPV1 can reverse the orientation of the *jRGECO1b* gene and thereby disable it.

Despite the small number of astroglia expressing TRPV1, addition of capsaicin to the fish water triggered elevated calcium activity (as measured via astroglial jRGECO1b) across the entire population of astroglia in the central nervous system (Fig. 3.13A), suggesting some intercellular communication between astroglia whereby transgenic cells could locally excite non-transgenic cells, e.g. via gap junction coupling (Scemes and Giaume 2006). To test whether TRPV1-mediated elevation of calcium activity could induce behavioral passivity, we measured fictive behavior of sparse *gfap:TRPV1*

transgenic fish in a closed-loop VR. Specifically, we quantified the fraction of time the fish spent a passive behavioral state. At baseline, i.e. before capsaicin was added to the bath, fish were passive 2.3±1.2% of the time; after capsaicin was added, fish were passive over 60% of the time (Fig. 3.13B-C). Neither saline administered to *gfap:TRPV1* fish, nor capsaicin administered to wild-type fish (Figure 3.13C-D), was sufficient to induce a comparable change in behavior. We examined the calcium activity of the L-MO-projecting astroglia in *gfap:TRPV1* fish to see if the calcium dynamics preceding the capsaicin-induced passivity resembled what we had previously observed in our open-loop VR assay. Indeed, we found that L-MO-projecting astroglia had similar activity patterns whether passivity was induced by futile behavior or capsaicin (Fig. 3.13A).

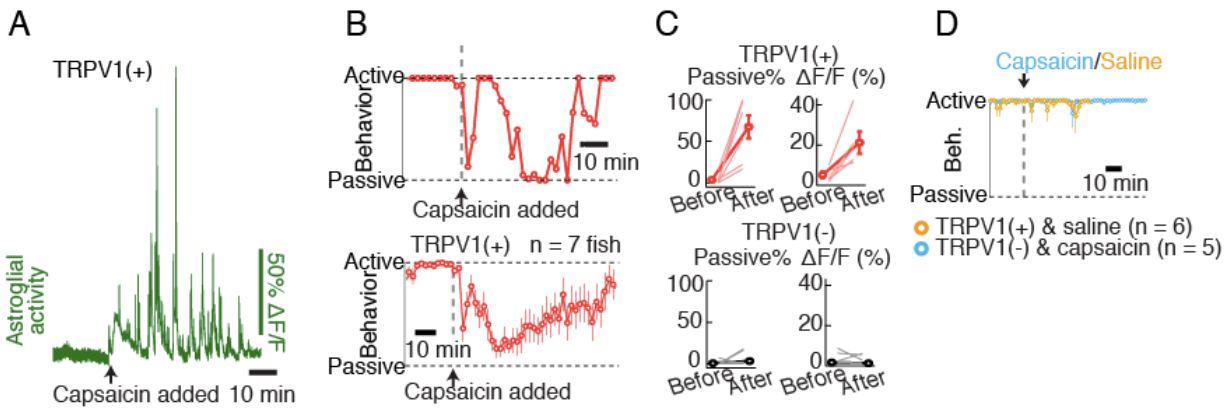

Figure 3.12. Inducing calcium activity in astroglia via capsaicin-induced activation of exogenous TRPV1 channels causes fish to become more passive.
(A) Mean glial calcium activity before and after bath application of 5 μM capsaicin. After capsaicin is added, astroglia as a population present with much more calcium activity, even though only a fraction of the astroglia express TRPV1, suggesting that the excitability of the entire population can be driven by a few cells. **(B)** Quantification of the effects of capsaicin application on the fictive swimming behavior of fish expressing *gfap:TRPV1* in a closed-loop VR paradigm. In both a single fish (top) and a population average (bottom), fish are tonically active before capsaicin is added (as to be expected, since this is how fish normally respond to closed-loop VR). After capsaicin is added, fish spend an increasing fraction of time in the passive behavioral state. The rate of Figure

3.12 (continued) passivity decays slowly, perhaps due to desensitization of TRPV1 channels. **(C)** Bulk quantification of the effects in (A) and (B) by taking the mean passive fraction, and mean calcium activity, over 10 minutes before and 10 minutes after adding capsaicin; In fish expressing TRPV1 in astroglia, addition of capsaicin elevates both the fraction of time the fish spent in the passive state and the mean activity level of astroglia. Neither effect is evident in fish without the TRPV1 transgene. **(D)** The induction of passivity in closed-loop VR requires the coincidence of TRPV1 in astroglia and capsaicin; neither exposing saline to TRPV1(+) fish, nor exposing capsaicin to TRPV1(-) fish was sufficient to induce passivity.

These results are consistent with our hypothesis that elevated calcium activity in astroglia is sufficient to induce passivity, but the tonic elevation in astroglial calcium induced by capsaicin is phenomenologically distinct from the temporally sparse calcium activity we observed in the open-loop assay; furthermore, capsaicin-mediated excitation of astroglia affects astroglia across the central nervous system, rather than just the L-MO-projecting astroglia. Thus, we endeavored to find a way to elevate astroglial calcium with more temporal and spatial precision. Fortunately, light-activated ion channels designed for depolarizing neurons can, if expressed in astroglia, increase astroglial calcium concentration to mimic physiological activation (Figueiredo et al. 2014; Cho et al. 2016). We expressed the short-wavelength channelrhodopsin CoChR (Klapoetke et al. 2014) under the GFAP promoter, which gave us the ability to excite these cells with blue light (Fig. 3.15A, 3.16A). We integrated a digital micromirror device (DMD) into our VR setup, which allowed us to direct excitation light to a region of interest with high spatiotemporal resolution (Zhu et al. 2012). After using calcium imaging to validate that optical excitation of astroglia evoked physiologically plausible calcium responses (Fig. 3.14A), we recorded fictive behavior from Tg(*gfap:CoChr-eGFP*) fish in a closed-loop VR assay and observed the effect of acute photostimulation of astroglial processes in

the L-MO region. Optically exciting astroglial processes in the L-MO induced strong, transient reduction in fictive swimming (Fig. 3.15B-C), which is consistent with our hypothesis that these cells cause the fish to become passive in open loop. A drawback of using CoChR is that it would also excite any neurons that happen to be labelled in our GFAP transgenic (Sloan and Barres 2014). We addressed this drawback by repeating these experiments with the optogenetic G-protein-coupled receptor Opto-α1-AR, which, when activated, drives release of calcium from intracellular stores without directly modulating the membrane potential like a channelrhodopsin (Airan et al. 2009). Photostimulating astroglia using Opto-α1-AR expressed under the GFAP promoter also suppressed swimming in closed-loop VR (Fig. 3.15C, right column). Taken together, these perturbation experiments provided strong evidence for our hypothesis that astroglial activity directly contributes to the onset of passivity in open-loop VR.

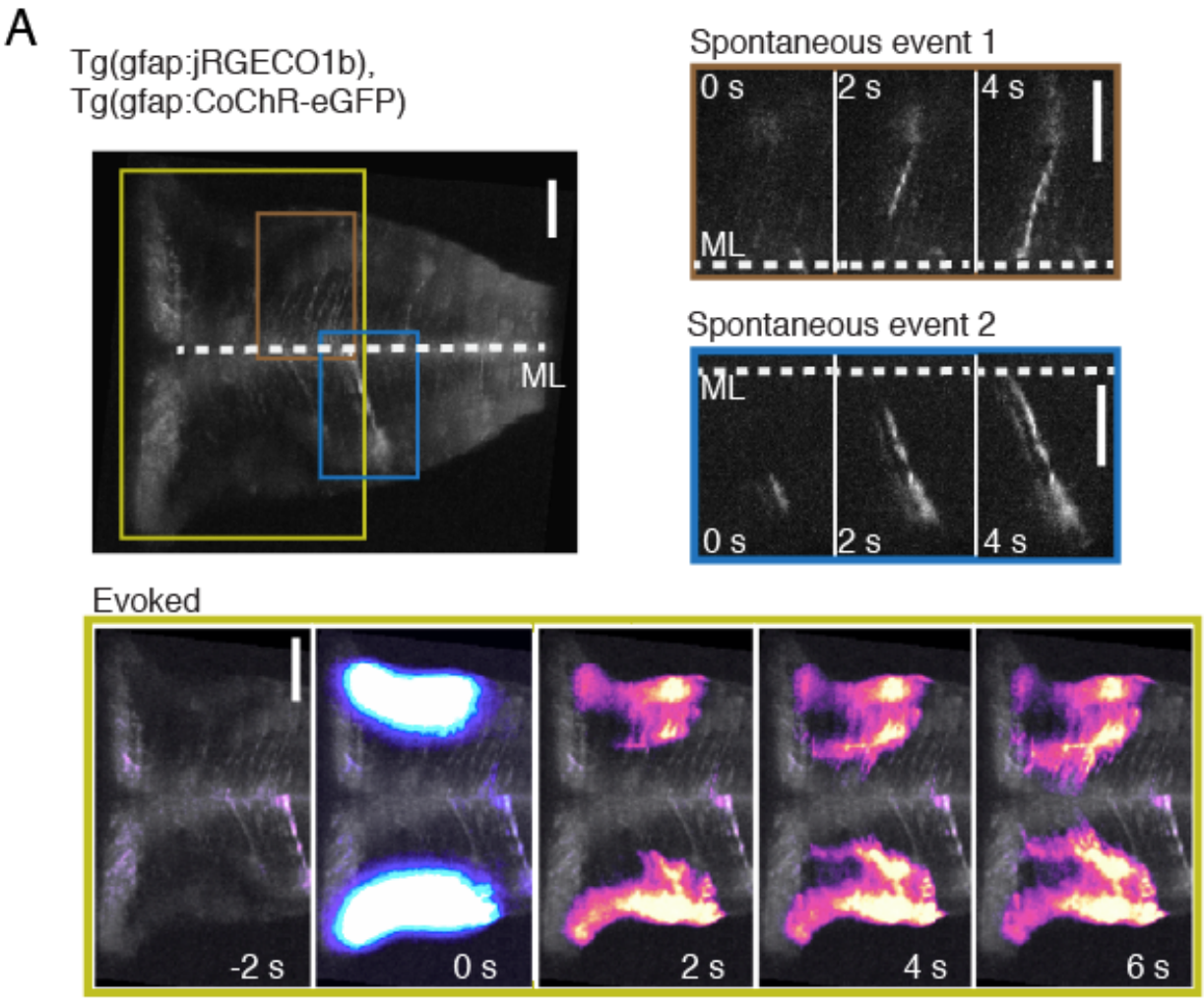

Figure 3.13. Optogenetic photostimulation of astroglia evokes spatially propagating calcium activity that qualitatively resembles spontaneous events.
(A) In a single fish expressing both CoChr and jRGECO1b under the GFAP promoter. **(Top right)** Two spontaneous events occur in cells in the region defined by the green and blue rectangles. These events are characterized by calcium activity within single astroglia that propagates toward the respective astroglial somata at the midline (ML, dashed line). **(Bottom)** The trial average of ~10 trials of optogenetic stimulation of astroglial processes in the L-MO causes a similar pattern of spatially propagating activity, but in a large number of cells. Scale bar: 20 uM.

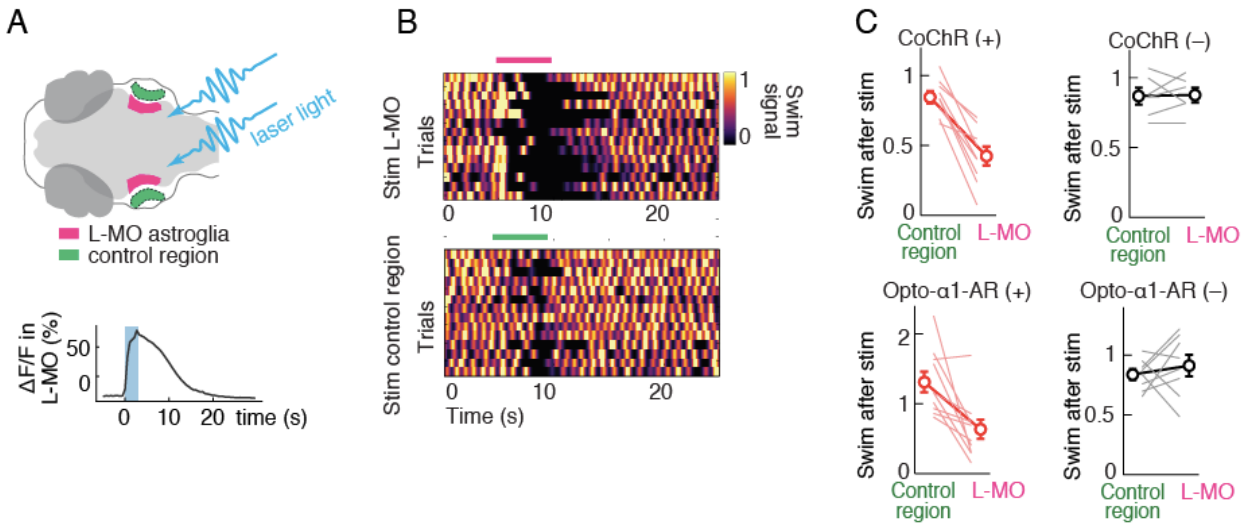

Figure 3.14. Optogenetic activation of L-MO-projecting astroglia induces passivity. **(A, top)** Cartoon illustrating targeting of patterned light to either the L-MO or a control region in the ear **(A, bottom)** Trial-averaged calcium activity in astroglia evoked by optogenetic excitation; the photostimulation artifact has been computationally removed. (B) Fictive swim power from a single Tg(*gfap:CoChr-eGFP*) fish, rendered with a colormap across multiple trials of photostimulation. The fish is in a closed-loop assay and swimming at ~1 Hz at baseline. When the L-MO region is stimulated, the fish becomes passive for ~5-10s, while there is only a transient reduction in swim power when light is directed to a control region. This transient reduction in swim power is likely due to the fish's response to the sudden appearance of blue light. **(C)** Population-level quantification of the behavioral effects of photostimulating L-MO astroglial processes. In only CoChr+ and Opto-α1-AR+ fish, photostimulating the L-MO astroglia induces a reduction in swim power.

Putative GABAergic neurons may receive excitatory input from L-MO astroglia

We found it very unlikely that astroglial activity in the L-MO was sufficient on its own to change the behavioral state of the animals. Rather, we believed that L-MO-projecting astroglia influence behavior by influencing on local neuronal circuits, as has been observed in other model organisms (Ma et al. 2016). By simultaneously imaging calcium activity in neurons while optogenetically exciting astroglia (Fig. 3.16 A), we found that putative GABAergic neurons in the L-MO showed elevated calcium activity after astroglia were excited (Fig. 3.16 B). Furthermore, optogenetically activating these

putative GABAergic neurons suppressed fictive swimming (Fig. 3.16 C), much like the astroglial excitation.

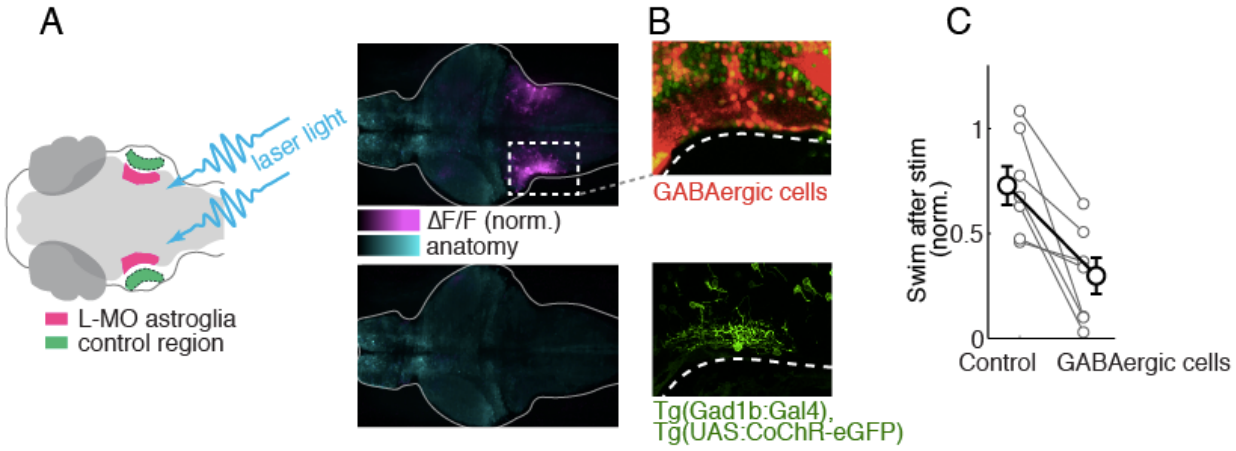

Figure 3.15. Putative GABAergic recipients of astroglial input inferred by simultaneous imaging and photostimulation.
(A, left) Cartoon illustrating targeting of patterned light to either the L-MO or a control region in the ear. Photostimulation in these experiments is done while imaging calcium activity in neurons using jRGECO1b. **(A, right)**. Example functional maps from a single fish. Intensity values represent the trial-averaged fluorescence taken in a short window after photostimulation. **(B)** Anatomical fluorescence imaging showing a density of GABAergic neurons in the L-MO region; these neurons co-localize with the photostimulation-induced activity peak in (A). **(C)** Quantification of the behavioral effects of optogenetically stimulating GABAergic L-MO cells in Tg(*Gad1b:Gal4*);Tg(*UAS:CoChR-eGFP*) fish. Photostimulating these cells induces a suppression of fictive swimming. N=7 fish.

L-MO-projecting astroglia are excited by norepinephrine

After observed that astroglia are excited during the transition from active to passive behavioral states, we immediately suspected that the astroglia were responding to norepinephrine (NE) released from the noradrenergic system. This suspicion came from two directions: first, studies of astroglia in other animals have found that NE is a potent driver of astroglial calcium responses (Bekar et al. 2008; Paukert et al. 2014), and second, in mammals NE has been implicated in cognitive adaptation to changing

circumstances (Bouret and Sara 2004; Aston-Jones and Cohen 2005; Sara 2009; Tervo et al. 2014), which loosely matches the alternation between active and passives states we observe in our open-loop VR assay. We looked in our brain-wide imaging data for signatures of the noradrenergic system, which in larval zebrafish is composed of neurons in the locus coeruleus (LC) and a medullary cluster (this cluster lacks a convenient name, so we called it the NE-MO) (Tay et al. 2011; Farrar et al. 2018). We found that neurons in the LC and NEMO increased their activity before the onset of passivity (Fig. 3.17A-B).

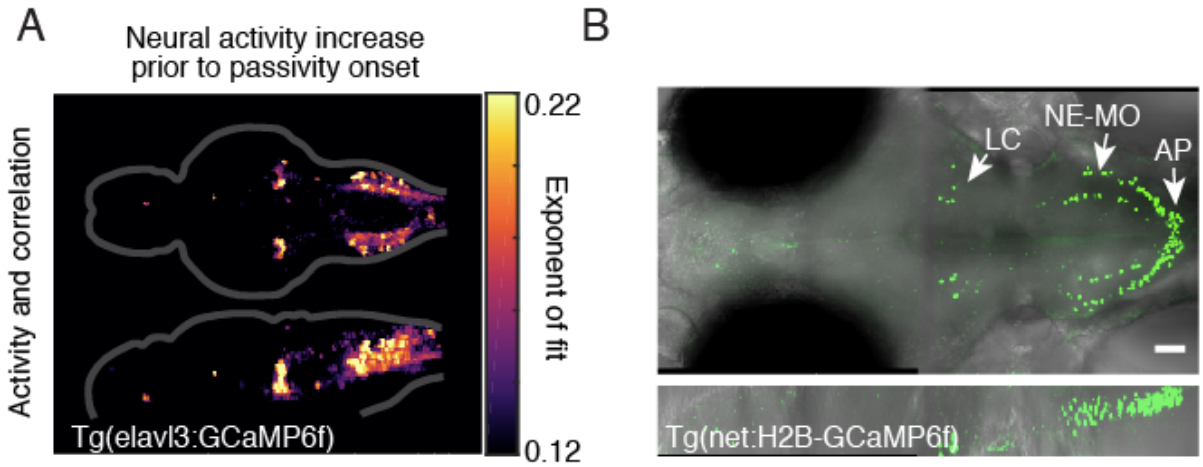

Figure 3.16. Hindbrain noradrenergic neurons rapidly increase their activity leading up to the onset of passivity.
(A) Dorsal-ventral and medial-lateral maximum projections of maps of coefficients generated by fitting neuronal calcium activity in the epoch leading up to passivity with an exponential function. Brighter values indicate larger coefficients, corresponding to a faster rate of calcium activity increase in those voxels leading up to passivity. **(B)** Dorsal-ventral and medial-lateral maximum projections of nuclear-localized fluorescence indicating the somata of cells expressing the noradrenergic marker gene *net*. This anatomical map qualitatively matches the functional map in (A).

To observe activity in the noradrenergic system, we used the *gal4*/*uas* conditional expression system to create transgenic fish expressing gal4 under the monoaminergic promoter *th1*. We then crossed these Tg(*th-p2a-Gal4*) fish with Tg(*UAS:GCaMP6s*) fish,

and crossed the offspring of this cross with Tg(*gfap:JRGECO1b*). These animals expressed GCaMP6s in dopaminergic and noradrenergic cells (which can be spatially distinguished) and jREGCO1b in astroglia, enabling for dual-color imaging to observe calcium activity in the noradrenergic system and astroglia simultaneously while fish performed fictive swimming in our open-loop VR (Fig. 3.17B). We observed a tight, consistent temporal relationship between noradrenergic activity and subsequent L-MO astroglial activity, suggesting that NE is driving astroglial calcium activity at the onset of passivity (Fig. 3.17B, C).

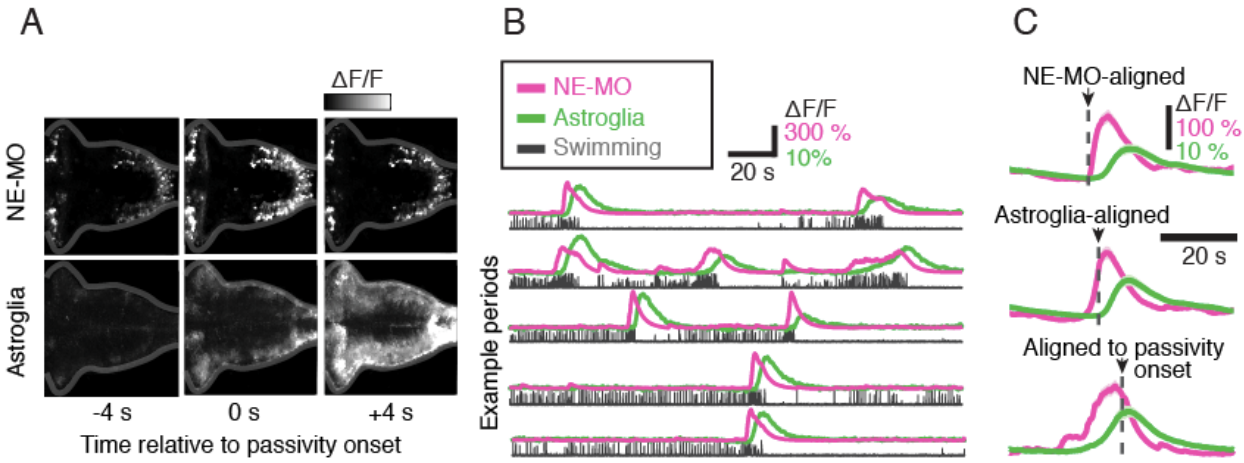

Figure 3.17. Activity in noradrenergic neurons at the onset of passivity precedes large-scale calcium activity in hindbrain astroglia.
(A) Example data from a two-color imaging experiment in which both astroglia and noradrenergic neurons express orthogonal calcium indicators. The animal is in an alternating closed-loop, open-loop paradigm; in open-loop, the animal becomes passive. Shown are maximum dorsal-ventral projections from 3 sequential timepoints, centered at the onset of passivity. Top row: GCaMP6s expressed under the monoaminergic promoter *th*; bottom row: jRGECO1b expressed under the GFAP promoter. Bulk astroglial calcium activity can be seen peaking shortly after the peak in activity in hindbrain noradrenergic cells (NE-MO). **(B)** Timeseries representation of additional data from the experiment sampled in (A), with the addition of behavioral data. The time-lag between NE-MO activity and astroglial activity is evident. **(C)** Mean calcium activity from NE-MO cells and astroglia taken from a window of time around each active -passive state transition and aligned to different timepoints within that epoch.

For L-MO-projecting astroglia to respond to NE, (at least) two things would need to be true: first, L-MO-projecting astroglia would need to express receptors for NE, and second NE would need to be released in the vicinity of astroglia. To address the first matter, we performed single-cell RNA sequencing on astroglia and neurons isolated by fluorescence-guided hand-sorting cells from brains of fish expressing tdTomato under GFAP and GCaMP6f under Elavl3. This procedure yielded gene expression profiles for astroglia and neurons; we found evidence that astroglia express a variety of noradrenergic receptors (Table 3.1). Specifically, we found evidence that astroglia strongly express the α2B and α1Ab receptors, and weakly express a variety of other receptors, in particular, the α1Bb receptor, which will be relevant shortly (Table 3.1). Additional evidence came from *in situ* hybridization results showing localization of noradrenergic receptors in astroglia processes and cell bodies (Fig. 3.18A). For the second matter, we validated that NE fibers project to the L-MO region using immunofluorescent labelling of NE fibers and astroglia and found extensive commingling of the two in the L-MO region (Fig. 3.18B). We did not trace these noradrenergic fibers to their somata of origin, so we cannot say whether the noradrenergic fibers in the L-MO originate in the LC or the NE-MO.

Gene	Std gene	Annotation	Astroglial TPM	Neuronal TPM
Adra1aa	ENSDART00000030938.8	adrenergic receptor, α1Aa	7.2	3.2
Adra1ab	ENSDART00000167973.1	adrenergic receptor, α1Ab	26.0	59.7
Adra1ba	ENSDART00000013641.8	adrenergic receptor, α1Ba	6.4	2.4
Adra1bb	Adra1b	adrenergic receptor, α1Bb	1.6	0
Adra1d	ENSDART00000014678.6	adrenergic receptor, α1D	6.6	0.0
Adra2a		adrenergic receptor, α2A	0.3	9.6
Adra2b		adrenergic receptor, α2B	109.8	22.3
Adra2c		adrenergic receptor, α2C	2.9	0
Adra2da		adrenergic receptor, α2D	0.3	1.5
Astroglial markers				
Cx43		Connexin-43	240.2	0
Slc1a3b	EAAT1	Glial glutamate transporter	399.7	0
Neuronal markers				
Ap1s3a	Ap1s3	adaptor protein AP-1, sigma 3	0	723.5
Cdh5		Cadherin 5	0	56.2

Table 3.1. Selection of RNA sequencing referred to in the text, and markers of the two cell types.
The α2B adrenergic receptor in particular was highly expressed in astroglia. Astroglia and neurons were well separated, as indicated by the orthogonal detection of expression of cell-type-specific marker genes. TPM: transcripts per million.

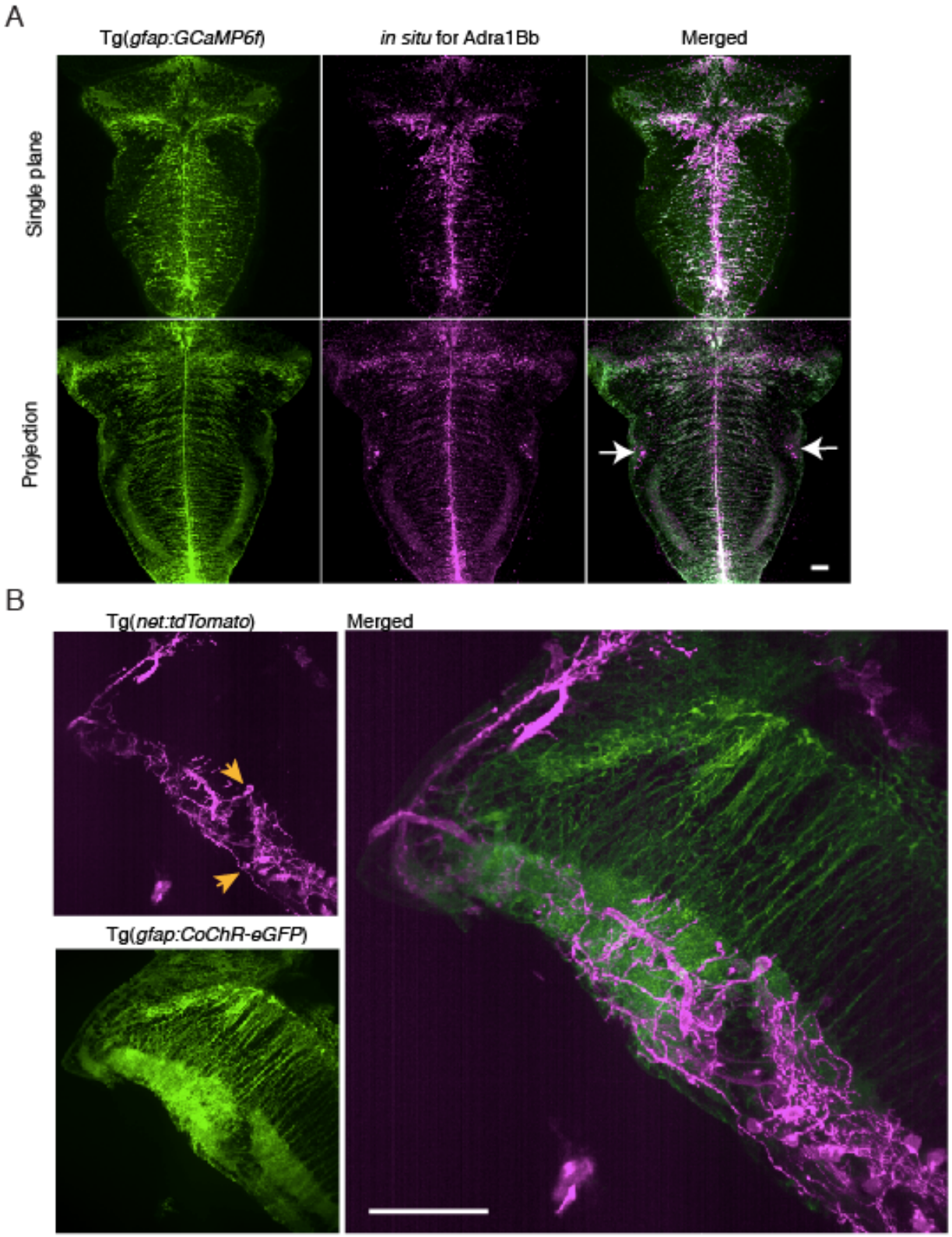

Figure 3.18. L-MO projecting astroglia express adrenergic receptors, and noradrenergic fibers innervate the L-MO.

Figure 3.18 (continued) (A) RNA encoding the α1Bb adrenergic receptor is visualized through fluorescence *in situ* hybridization. The lateral hindbrain (L-MO) showed high levels these transcripts, which suggests localized expression of the α1Bb receptor (arrows). The projection is a maximum intensity projection over a 40 μm thick section. **(B)** Expansion microscopy was used to generate high resolution images of noradrenergic neurons (arrows) and noradrenergic fibers innervating the L-MO. Astroglial processes are also shown in the same region.

Having established that the cellular structures in the LMO are compatible with our hypothesis that astroglia respond to NE at the onset of passivity, we tested the extent to which the two main noradrenergic nuclei (LC and NEMO) are necessary for the switch from active to passive behavioral states. We used an ultrafast pulsed laser to ablate noradrenergic neurons in either the NEMO or LC, and then monitored fictive behavior of fish in our open-loop VR. Our prediction was that if either noradrenergic nucleus was necessary for the transition from active to passive behavioral states, then we would see a reduction in the rate of passivity after ablating that nucleus. We found that after NE-MO ablation, but not after LC ablation, the fish spent much less time in the passive state (Fig. 3.19A). We subsequently checked whether optogenetically exciting NE-MO was sufficient to excite LMO-projecting astroglia. For this experiment, we used Tg(*th-p2a-Gal4);* Tg(*UAS:CoChr-egfp*);Tg(*gfap:jRGECO1b*) animals so that we could optogenetically stimulate noradrenergic cells with blue light while recording calcium signals in astroglia with green light. Optogenetic stimulation of the NEMO reliably induced a surge of calcium activity in L-MO-projecting astroglia and induced transient behavioral passivity (Fig. 3.19B). Both of these effects were abolished after ablating LMO-projecting astroglia (Fig. 3.19C, D), which shows that the passive state induced by optogenetic stimulation of NE-MO depends on astroglia.

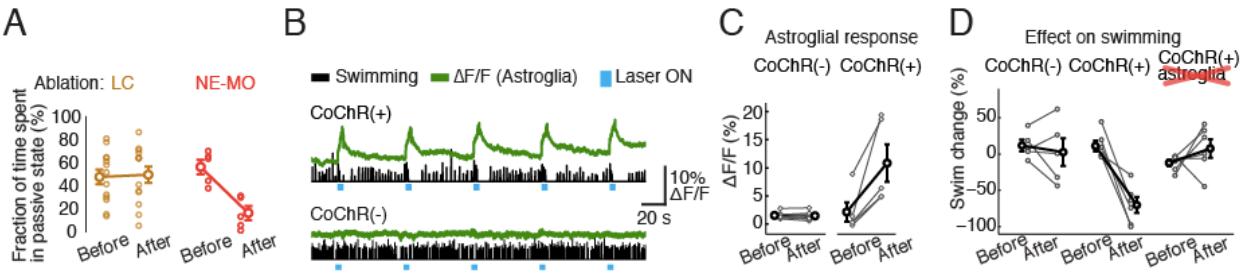

Figure 3.19. Hindbrain noradrenergic neurons are necessary for passivity in open loop. **(A)** Comparing the effects of two-photon laser ablation of the LC (left) or the NE-MO (right) on the rate of passivity in open-loop VR. Ablating the NE-MO, but not the LC, resulted in a reduction in the rate of passivity in open-loop VR. **(B)** Optogenetic stimulation of the NE-MO region in parallel with calcium imaging of astroglia in two example fish, one of which expressed CoChr in noradrenergic neurons (top). Both animals performed fictive swimming in closed loop. Photostimulation of the NE-MO region induced an astroglial calcium response and a transient passive epoch in the animal with the opsin in the NE-MO. **(C)** Population-level quantification of the effect of NE-MO photostimulation on astroglial calcium response demonstrated in (B). Only in fish expressing CoChr in noradrenergic neurons did photostimulation of the NE-MO induce a strong calcium response in astroglia. **(D)** The effect of photostimulating the NE-MO on fictive behavior was evaluated across three groups of fish: (i) animals without CoChr in noradrenergic neurons, (ii) animals with CoChr in noradrenergic neurons, and (iii) animals with CoChr in noradrenergic neurons *and* two-photon-laser-ablated astroglia. Only in the second group of animals did photostimulation of the NE-MO induce a subsequent suppression of fictive swimming.

In order to determine which receptor(s) mediate the astroglial response to NE, we performed a series of pharmacological manipulations. We added adrenergic receptor antagonists while optogenetically exciting NE-MO and recording calcium activity in L-MO astroglia. Pharmacologically blocking the α1-adrenergic receptor using the antagonists prazosin or cyclazosin abolished the astroglial response to NE-MO stimulation (Fig. 3.20A, B), which indicates that the astroglial α1 NE receptors mediate the response to NE-MO stimulation. We further tested this hypothesis by recording astroglial calcium responses to local extracellular administration of the α1-agonist

methoxamine; puffing methoxamine on astroglial processes evoked a strong calcium response, while puffing saline had no effect (Fig. 3.20C).

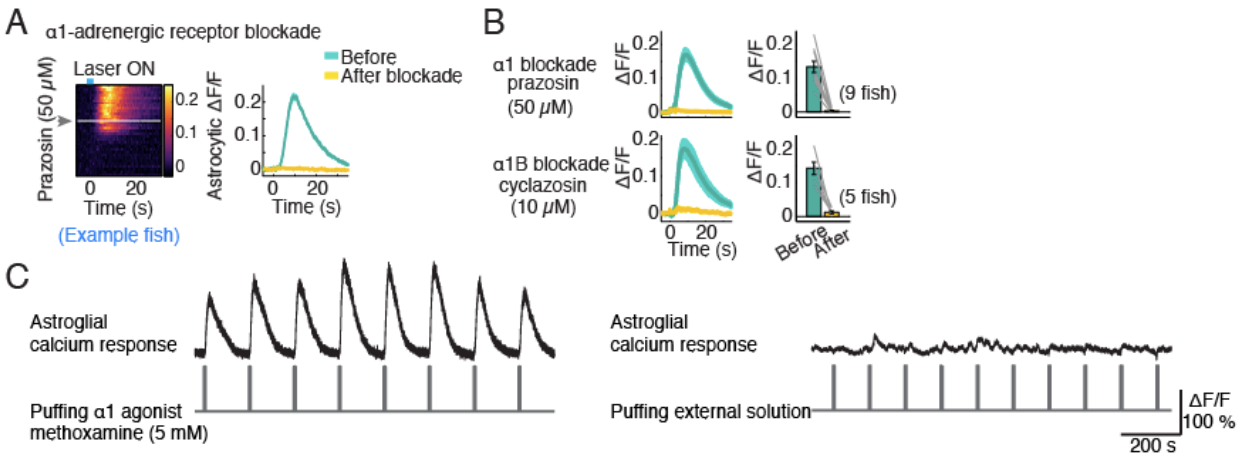

Figure 3.20. α1-adrenergic receptors are necessary for astroglial calcium responses to NE-MO photostimulation.
(A) Data from an example fish showing that astroglial calcium responses to NE-MO photostimulation are abolished shortly after the α1 adrenergic receptor prazosin was applied to L-MO-projecting astroglia. Left, astroglial calcium responses from multiple trials of photostimulation represented as a raster plot. Right, the time series obtained by taking the trial-average before and after application of the drug. **(B)** Repeating the same experiment exemplified in (A) but with more animals yields a consistent result. Applying cyclazosin, α1-adrenergic receptor antagonist that is specific to the α1b receptor, suggests that the α1b-adrenergic receptor is specifically necessary for astroglial calcium responses. **(C)** Applying either the α1-adrenergic receptor agonist methoxamine (left) or saline (right) while optically recording astroglial calcium responses shows that α1-adrenergic receptor activation is sufficient for driving astroglial calcium responses.

Is NE the only source of input to L-MO-projecting astroglia? We were inspired by work in mice (Paukert et al. 2014) to check whether calcium responses in L-MO-projecting astroglia are driven by NE alone, or a combination of NE and local circuit activity (which astroglia may respond to via, e.g., changes in extracellular concentration of glutamate or potassium). Since we know that the L-MO neuropil is modulated by the animal's motor output (Fig. 3.7A), we used the fictive behavior of the animal as a proxy for local circuit activity in the L-MO. We found that fictive swimming that coincided with

optogenetic excitation of the NE-MO induced a much larger calcium response in astroglia than either fictive swimming or NE-MO excitation alone (Fig. 3.21B, C).

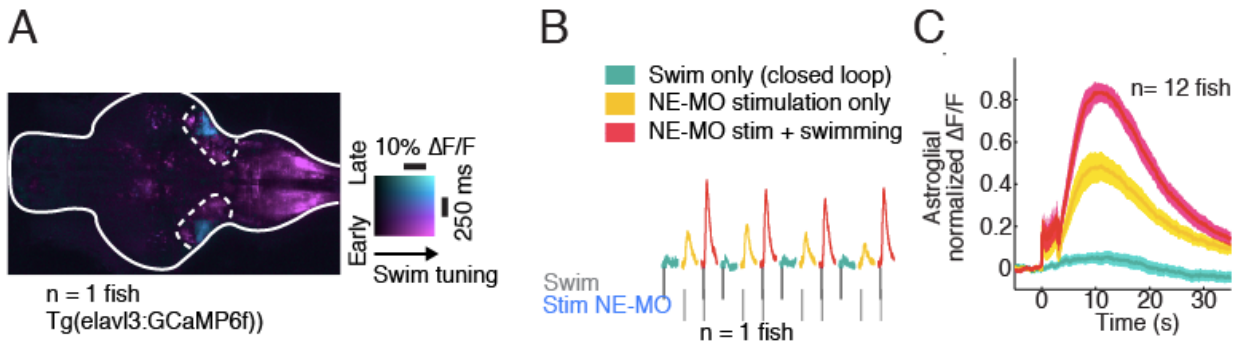

Figure 3.21. Astroglial calcium activity in the L-MO depends on coincident NE-MO activity and locomotor circuit activity.
(A) Functional map derived from analysis of functional imaging data showing brain areas where neuronal calcium activity is tuned to fictive locomotion. The magenta-cyan axis of the colormap encodes the phase of the tuning relative to swimming. **(B)** Sample traces from a single fish in an experiment where the NE-MO is stimulated independently of fictive swimming or coincidently with a fictive swim bout. Photostimulation was performed in parallel with functional imaging to record responses of L-MO-projecting astroglial processes to three stimulus conditions: swimming, NE-MO photostimulation, or NE-MO photostimulation coincident with swimming. **(C)** Population-level quantification of the results of the experiment described in (B), comparing the event-triggered average responses of astroglia across the three conditions described in (B). The astroglial response to coincident fictive swimming and NE-MO activation is more than the sum of either response alone.

Hindbrain noradrenergic neurons encode sensorimotor error

The previous experiments led us to formulate the following model: L-MO astroglia encode swim futility, which we postulate is the sum of recent behavioral failures (i.e., sensorimotor errors), via intracellular calcium levels; some mechanism downstream of astroglial intracellular calcium then drives a neural circuit to suppress behavior. Under this model, the L-MO-projecting astroglia must receive inputs that encode sensorimotor errors, and then temporally integrate these inputs to generate a behavioral futility signal. Knowing that NE released from the NE-MO is a potent source of input to L-MO

projecting astroglia during the transition from active to passive states, we asked if the NE-MO encodes sensorimotor error (Keller et al. 2012). To answer this question, we used calcium imaging to observe activity in NE-MO under three conditions, interleaved over swim bouts: (1) fictive swimming in closed loop, to mimic naturalistic swimming; (2) backward optic flow without a fictive swim, to mimic an exogenously generated forward displacement of the fish; (3) fictive swimming in open loop without any feedback (Fig. 3.22A). If NE-MO is chiefly motor-tuned, then we would expect to see strong responses to conditions (1) and (3), however, if NE-MO is tuned specifically to sensorimotor error, then we should see strong responses only in condition (3). Indeed, this is what we observed: NE-MO responses were negligible when fish swim in closed-loop or when fish observed backward optic flow without fictive swimming, but large when fish swam without receive visual feedback (Fig. 3.22B). We next quantified whether NE-MO responses encode the difference between perceived and expected visual feedback during fictive swimming. We randomly varied the gain of the VR to enable the following sensorimotor contingencies: 'successful' fictive locomotion, when the fish performed fictive swimming while gain > 0; and 'failed' fictive locomotion, when the fish performed fictive swimming while gain ≤ 0 (Fig. 3.22C). NE-MO signals recorded in this assay were proportional to the degree of sensorimotor mismatch: when fish swam while the gain was set to 0, NE-MO responses were proportional to locomotor vigor (Fig. 3.22D, E); when fish swam when the gain was < 0 (when gain < 0, fictive swimming will move the visual stimulus forward, rather than backward), NE-MO responses were proportional to the stimulus velocity (Fig. 3.22F, G).

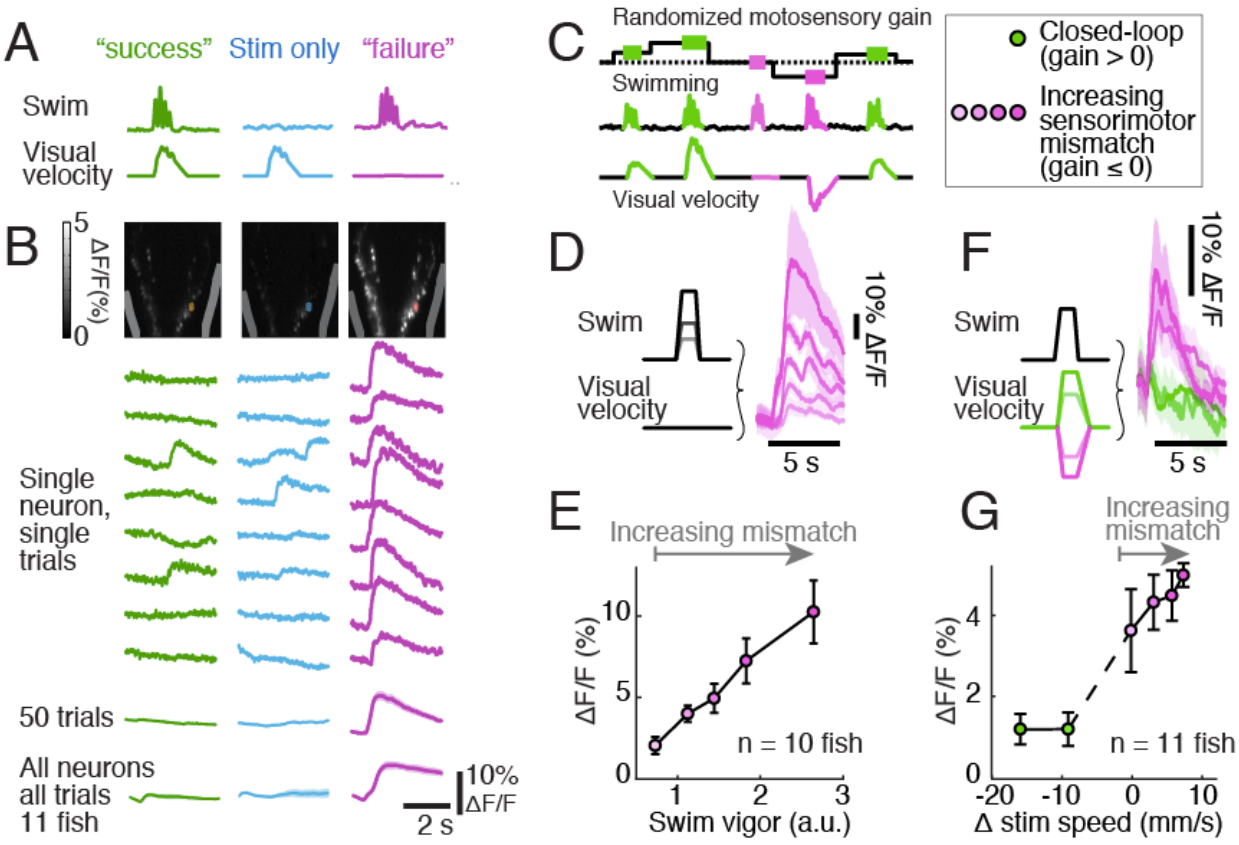

Figure 3.22. NE-MO cell responses are consistent with sensorimotor error encoding. **(A)** Cartoon illustrating our conceptualization of sensorimotor error. We consider three sensorimotor contingencies: first, motor output that coincides with the normal visual stimulus (in the case of the OMR, the normal stimulus in response to forward swimming is backward optic flow); second, backward optic flow without any motor output, and third, motor output without any visual stimulus (sensorimotor error). **(B)** Imaging calcium activity in NE-MO cells while animals experience the three sensorimotor contingencies defined in (A). In single trials (top) and the population average (bottom), NE-MO cells only respond to sensorimotor error. **(C)** Schematic of VR experiments designed to test whether NE-MO responses are proportional to the magnitude of sensorimotor mismatch. **(D)** Example NE-MO fluorescence data triggered on fictive swimming (with variable vigor) at 0 gain. NE-MO responses scale with the vigor of the fictive swims. **(E)** Population data of swim-triggered NE-MO responses plotted against fictive swim vigor, showing a linear relationship. **(F)** Example NE-MO fluorescence data triggered on fictive swimming (with constant vigor) with variable gain. **(G)** Population data of swim-triggered NE-MO responses plotted against visual stimulus speed, showing a linear relationship for speeds above 0.

Given that the NE-MO respond as if these cells encode sensorimotor error, we next

tested whether L-MO projecting astroglia are integrating this noradrenergic error signal,

perhaps akin to evidence accumulation processes that have been described in other central nervous system circuits (Shadlen and Newsome 2017; Pinto et al. 2018). To test for evidence of this process, we designed a VR paradigm that blended open- and closed-loop VR while we imaged calcium levels in L-MO-projecting astroglia. In this blended paradigm, each swim bout was randomly assigned to either nonzero gain (closed-loop) or zero gain (open-loop), with some probability *p* (Fig. 3.23A). We anticipated that, if L-MO-projecting astroglia are integrating evidence for futility, then their calcium levels in our assay should be proportional to the closed-loop probability *p.* Indeed, this is what we observed: mean glial calcium responses during swimming in this assay were indicative of *p* (Fig. 3.23B). This shows that an astroglial calcium signal can function as an integrator of behavioral failures, and thus possibly signal that recent behavior is futile.

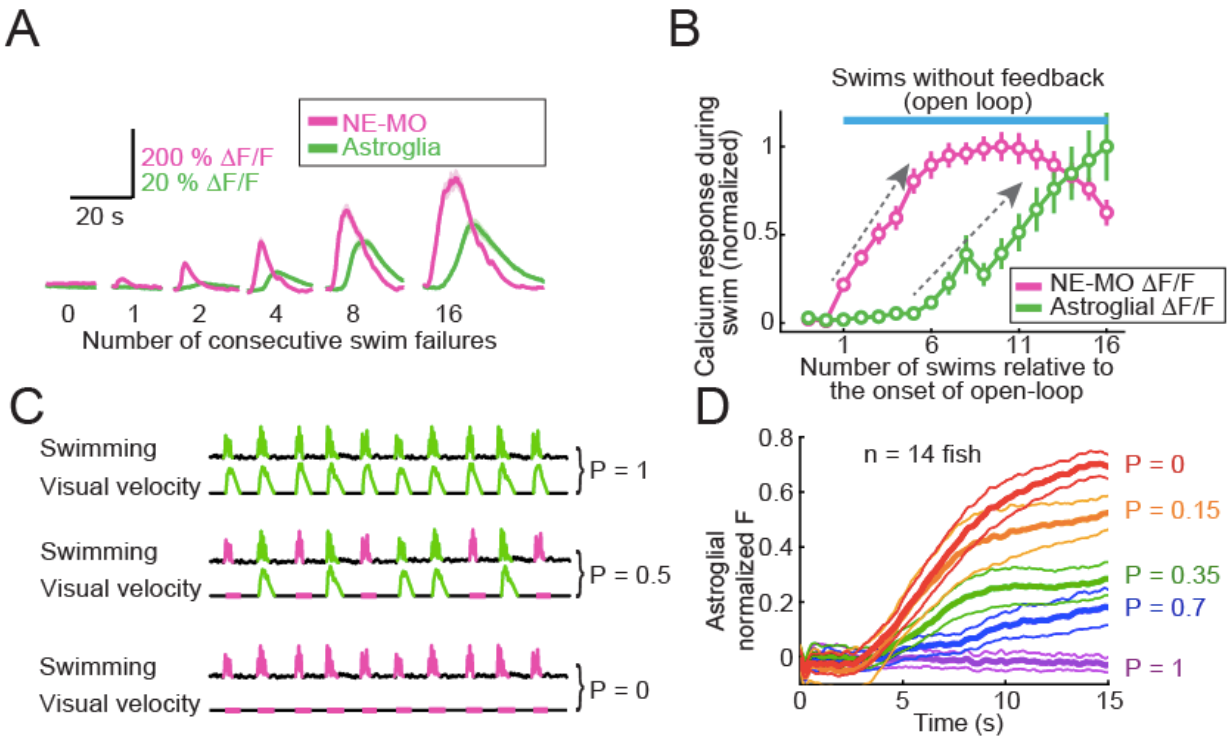

Figure 3.23. Evidence that L-MO-projecting astroglial calcium signals encode accumulation of sensorimotor error.
(A) NE-MO and astroglial calcium activity recorded from a single fish in an alternating closed-loop / open-loop VR paradigm, where the duration of open loop was locked to an integer number of swim bouts (major x axis). Both NE-MO and astroglial calcium signals increase with increasing numbers of failed swims. **(B)** Astroglial calcium signals accumulate with increasing numbers of swim failures. NE-MO calcium signals also increase at the onset of open-loop but saturate and/or decrease earlier than astroglial calcium levels. Gray arrows emphasize the putative accumulation of an error signal. **(C)** Illustration of an experiment to test whether astroglial calcium levels encode time-averaged motor futility. A fish swims in a VR where, for each swim bout, the gain is either 1 (closed loop) or 0 (open-loop) with some probability *P*. **(D)** Population-average response of L-MO-projecting astroglia in the paradigm schematized in (C), with different closed-loop probabilities. The mean astroglial calcium level reflects the closed-loop probability *P*.

Discussion

Here we report that larval zebrafish respond to the loss of sensorimotor feedback by entering a bi-stable behavioral mode wherein animals alternate between active and passive behavioral states. Additionally, we found that astroglia and noradrenergic

neurons are crucial for the transition from active to passive behavioral states. We synthesize these findings in a model wherein noradrenergic neurons respond to individual

Our first main finding was that larval zebrafish respond to open-loop VR by alternating between active and passive states. As humans, we found this behavioral response very relatable: we have all experienced frustrating, seemingly futile tasks that ultimately drive us to give up and do something else. We also found examples of similar behavioral responses in the literature—researchers studying depression have developed a host of assays designed to evoke a phenomenon termed “behavioral despair” in rodents. Behavioral despair is operationally defined as a prolonged epoch of stable behavioral passivity induced by repeated exposure to inexorable aversive stimuli, such as electric shocks, immersion in water, and being suspended from the tail (Maier 1984; Steru et al. 1985). These stimuli are all explicitly aversive, but our open-loop VR may not be; we have not evaluated whether open-loop VR is aversive to larval zebrafish. Thus, it seems premature to say that larval zebrafish in open-loop VR are experiencing behavioral despair, but we can still note the commonality of the passive behavior evoked in both cases.

Why might passivity be a common response to generalized behavioral futility? It is possible that this response is strategic. Suppose an immobilized animal uses the feedback-stabilized motor control strategy that works well under normal locomotion. While immobilized, all locomotion attempts fail to move the animal and thus these attempts will produce error signals; if the animal responds to these error signals by

raising the vigor of its subsequent efforts, then the animal will soon be attempting to move with maximum vigor, yet these vigorous actions will still generate error signals. The feedback-stabilized motor control strategy fails here: it equilibrates with the animal exerting maximum vigor for every action, yet accomplishing nothing, or worse. Generally speaking, vigorous actions are more metabolically expensive, more salient to potential predators, and more likely to interfere with observation of the environment than less vigorous actions; as long as these vigorous actions fail to remobilize the animal, their costs weigh over the nonexistent benefits. These costs can all be minimized by ceasing all efforts as long for as those efforts are futile, i.e. by adopting a passive behavioral state, where the urge to move is suppressed. The animal should only become passive once it can infer that its recent actions have accomplished nothing and thus that the same holds for subsequent actions. But if the animal wants to remobilize, this passive state cannot last forever—the animal should be prepared to act again at the first sign that it has regained mobility, and sometimes the simplest way to test for remobilization is just to attempt to move again. Under these conditions, the animal can be expected to alternate between active behavioral states, which maximize the short-term probability of escaping immobilization, and passive behavioral states, which minimize the long-term probability of metabolic depletion and exposure to predators. In summary, immobilization, due to a predator or environmental conditions, is a life-threatening failure mode for feedback-stabilized motor control. The failure mode can be addressed by adding a higher-order control rule: when repeated movement attempts fail to produce the correct feedback, become passive for some interval of time before

attempting to move again. This speculation could be tested by making observations of wild fish, or other animals, *in situ*, with a particular emphasis on observing the various types of locomotor challenges animals experience, and what motor strategies animals use to respond to these challenges.

Our second main finding was that astroglial calcium signaling in response to norepinephrine is crucial for the switch from active to passive behavioral states. Our finding that astroglia in larval zebrafish respond to norepinephrine is not surprising, given the evidence from other model systems showing that NE (or its homolog) excites astroglia (Paukert et al. 2014; Ma et al. 2016). But our claim that astroglia are part of a behaviorally relevant circuit is surprising. The traditional view of neural circuits, which is grounded in a long history of electrophysiology experiments, holds that circuits in the central nervous system are exclusively composed of neurons, but recent studies leveraging calcium imaging have revealed circuits composed of neurons and astroglia (Morquette et al. 2015; Ma et al. 2016; Poskanzer and Yuste 2016). The existence of interactions between neurons and astroglia should not come as a surprise: astroglia are excitable cells that express receptors for neuromodulators, and there are many mechanisms through which they can influence neuronal activity (Ahmed et al. 1990; Wang et al. 2012; Deemyad et al. 2018). Additionally, astroglia may fill a specific computational niche: because of their extensive spatial ramifications and relatively slow calcium dynamics, astroglia may spatiotemporally integrate signals more easily than neurons (Deemyad et al. 2018). This is merely informed speculation; network modelling studies could investigate this claim further.

Through optogenetic stimulation of L-MO-projecting astroglia, we identified a population of putative GABAergic neurons that we believe are somehow excited by calcium activity in L-MO-projecting astroglia (Fig. 3.16). We do not know the mechanism for this putative interaction, but in other organisms it has been shown that astroglial calcium flux can trigger release of ATP from astroglia, which then modulates neuronal activity through purinergic receptors on neurons (Wang et al. 2015; Ma et al. 2016; Shigetomi et al. 2016). Resolving the exact mechanisms of astroglial-neuronal communication in larval zebrafish will be a challenging undertaking, as new tools and preparations will need to be developed—chiefly, a brain slice preparation which allows washing in and washing out of specific receptor agonists and antagonists. But until such a preparation exists, we can only speculate as to how exactly astroglia may influence neuronal activity in larval zebrafish.

We synthesize our behavior and physiology data into a model wherein noradrenergic hindbrain neurons encode sensorimotor error, and astroglia integrate this signal, subsequently suppressing behavior when the integrated sensorimotor error (or, "behavioral futility") crosses some threshold. Additional analyses and experiments would add validity to this model. First, this model makes a claim about a process that should be evident in single trials of open-loop-induced passivity, yet we provide evidence for the model on the basis of trial averages that aggregate over many behavioral epochs (Fig. 3.22, 3.23). If our model is correct, and if the phenomena it describes are the primary mechanisms for determining when fish are active and when fish are passive, then the model should have predictive power at the level of single

trials. We have not yet demonstrated this. Second, although we have access to nearly all of the relevant variables (visual stimulus state, fictive behavior, activity levels in NE-MO cells and L-MO-projecting astroglia), we have not yet attempted to use these variables to fit explicit computational models of error detection and integration that could be used to predict behavior. Doing so would likely highlight the strengths and shortcomings of our model, and thereby enable us to improve it.

Materials and methods

Experimental animals

Zebrafish larvae were raised and used for experiments under the same conditions as those described in Chapter 2. The transgenic line TgBAC(*gad1b:loxP-RFP-loxP-GFP*) (Satou et al. 2013) was used without Cre-mediated recombination and called Tg(*gad1b:RFP*). The Tg(*elavl3:ReaChR-TagRFP-T*) was previously described (Dunn et al. 2016). The Tg(*gfap:CoChR-eGFP*), Tg(*gfap:opto-α1AR-GFP*), Tg(*dbh:KalTA4*), Tg(*UAS:CoChR-eGFP*) and Tg(*gfap-TRPV1-T2A-eGFP*) lines were generated with the Tol2 system (Urasaki and Kawakami 2009), a known *gfap* sequence (Bernardos and Raymond 2006) and the following:

1. Construct containing dopamine-β-hydroxylase (dbh) promoter (dbh-GFP-pDEST-ISce); a gift from Thomas Look (Dana Faber Cancer Institute)
2. Construct containing transient receptor potential cation channel subfamily V member 1 (TRPV1) (or capsaicin receptor) from rat; a gift from David Prober (California Institute of Technology)
3. pEGFP-gfap (Intron1/5'/Exon1-zebrafish) (Addgene plasmid # 39761)
4. FCK-gene86-GFP (CoChR); a gift from Ed Boyden (Klapoetke et al. 2014)
5. pcDNA3.1-opto-α1AR-EYFP (Addgene plasmid # 20947)

The Tg(*gad1b:Gal4*) fish line was generated by CRISPR-mediated knock-in of Gal4 (Gal4FF) at the *gad1b* locus as described (Kimura et al. 2014). The sgRNA sequence

for *gad1b* is TGGAACTGCTCACCAGAAGG. *2XNRSE-tbait-hsp70-Gal4* (Kimura et al. 2014) was a gift from Shin-ichi Higashijima.

Fictive swimming in virtual reality

Functional imaging during fictive behavior was performed using the same methodology described in Chapter 2. For behavioral experiments without imaging, paralyzed fish were agarose-embedded in a petri dish instead of the custom light sheet chamber.

Patterned photostimulation

To target specific populations of cells for optogenetic stimulation, we built two photostimulation modules using digital micromirror devices (DMD) from commercial projector displays (P-300, AAXA; Lightcrafter discovery kit, Texas Instruments). One photostimulation module was integrated to a standard epifluorescence microscope, and the other was integrated to our light sheet microscope. The optical design of our photostimulation modules has been previously described (Zhu et al. 2012). Briefly, the DMD was illuminated by a blue laser (488 nm in setup 1; 473 nm in setup 2). Patterned light reflected off the DMD was spatially filtered with a pinhole to select the 0^{th} diffractive order, then the relayed image of the DMD was expanded and projected onto the sample plane of the microscope. We wrote C#, Python, and Arduino software to control the lasers and create spatial patterns for photostimulation. The following parameters were used for optogenetic stimulation: For Tg(*dbh:KalTA4);*Tg(*UAS:CoChR-eGFP*) fish on setup 1, the excitation intensity was 0.17 mW / mm^2 and the stimulation duration was 3 seconds of 10 millisecond pulses delivered at 10 Hz. For Tg(*gfap:opto-α1AR-GFP*) fish on setup 1, the excitation intensity was 0. 42 mW / mm^2; the stimulation duration was 10

seconds of continuous illumination. For Tg(*gfap:CoChR-eGFP*) fish on setup 2, the stimulation intensity ranged from 0.23 to 0.46 mW / mm^2; the stimulation duration was 3 seconds of 10 millisecond pulses delivered at 10 Hz.

Two-photon ablation of cells

For single-cell plasma ablation, we used a tunable ultrafast laser (Coherent, Chameleon Ultra II). Astroglia were selected based on their location between rhombomere 2 and rhombomere 6, along the midline of the dorsal hindbrain, and a genetic marker in Tg(*gfap:H2B-GCaMP6f*) fish. Ablation was done with high laser power (930 nm, 500 mW, measured after the objective) directed to a point on each cell with short exposure time (1-4 ms), with 300-400 ms between ablations to prevent thermal damage. After successful ablation, previously bright, round nuclei appeared dim, irregular or fragmented. Cells without this signature were selected again for a subsequent round of ablation. Each fish required 3–5 rounds of ablation. Subsequent imaging or behavioral experiments were initiated at least 30-60 minutes after the last round of ablation. Noradrenergic neurons in the LC and the norepinephrine cluster of the medulla oblongata (NE-MO) were similarly ablated in Tg(*th-P2A-Gal4*)*;* Tg(*UAS:GCaMP6s*) fish. In control experiments, similar numbers of neurons labeled by Tg(*elavl3:H2B-GCaMP6f*) in nearby brain regions were ablated with the same protocol.

TRPV1-mediated activation of astroglia

For TRPV1-mediated activation (Chen et al. 2016a) of astroglia, we injected the *gfap:TRPV1-T2A-eGFP* plasmid into embryos from Tg(*gfap:jRGECO1b*) transgenic fish at the 1–2 cell stage. TRPV1 protein expressed sparsely in astroglia. Fish were

screened at 3 dpf: larvae with strong, sparse GFP expression in the hindbrain were the 'TRPV1 (+)' group; those without detectable GFP expression were the 'TRPV1(-)' group. Both groups were screened again based on expression of jRGECO1b, and subdivided into four groups: 'TRPV1(+) jRGECO1b(+)'; 'TRPV1(+) jRGECO1b(-)'; 'TRPV1(-) jRGECO1b(+)'; and 'TRPV1(-) jRGECO1b(-)'. All fish were tested behaviorally; jRGECO1b-positive fish were imaged in a light sheet microscope. For all experiments, fish were recorded for at least half an hour, and then capsaicin (Sigma; 5 μM final concentration in system water) or saline was delivered into the recording chamber, and recording continued for 1 to 2 hours. Calcium responses and behavior were quantified in two 10-minute windows: from 11 minutes to 1 minute before capsaicin ('before' treatment) and from 10 to 20 minutes after capsaicin ('after' treatment).

IP_3 receptor blockade

To partially block the calcium concentration increase in astroglia, we inhibited IP_3 receptor-dependent calcium release by loading the inhibitor Xestospongin C (Sigma) (Gafni et al. 1997) near astrocytic cell bodies. Glass pipettes were pulled on a micropipette puller (P-1000, Sutter Instruments), and broken on a microforge (MF900, Narashige), to get a 10 µm-wide tip. This sharp glass pipette was loaded with 5 µL of a mixture of Xestospongin C (100 µM, in external solution) and a fluorescent dye (Dextran, Texas Red, 0.5%, or Dextran, Fluorescein, 0.5%, Thermofisher) to visualize the ejection. The pipette was then inserted through the skin of a paralyzed Tg(*gfap:GCaMP6f*) fish and advanced to the hindbrain ventricle, near astrocytic somata. We first assessed how long the fish spent in a passive state while in open loop for 30

minutes. Then, pulses (20 psi, 30 ms, inter-pulse-interval 30 seconds, 10 pulses) were delivered using a pressure ejection system (Picosprizter III, Parker Hannifin). Fish were then switched to the closed-loop condition for ~20 minutes to allow the drug to take effect and then back to open loop to record the time spent in passivity.

Segmentation of fluorescence imaging voxel data

We developed a data-processing pipeline to first convert the raw pixel data into superpixels, and then to merge the superpixels into "components": superpixels with similar activity patterns and reproducible anatomical structure; and finally to align and compare superpixels and components at specific behavioral reference points and across different fish. For each fish, our analyses began with motion correction via ANTs 2.1.0 rigid-body registration of all volumes to the average volume (Avants et al. 2010). Then we created an intensity-based brain mask and fully divided the brain into about 1000 spatially contiguous three-dimensional blocks, which overlapped slightly to capture cells on the borders. We used the Spark cluster computing framework (Zaharia et al. 2010) to parallelize cell-detection across blocks. Our algorithm was based on constrained non-negative matrix factorization. For n voxels, t timepoints, and c cells, we factorized

$$V_{(n \times t)} \approx W_{(n \times c)} H_{(c \times t)} + X_{(n \times 1)} I_{(1 \times t)} \quad \text{(eq. 1)}$$

where V is the full spatiotemporal fluorescence matrix for each block, W and H are, respectively, the spatial location and time series of segmented cells, and X and I are a

rank-1 spatiotemporal model of the background signal. We set the block size under the assumption that each block would contain 100 tightly packed 6 μm diameter spheres. Thus, we set the number of cells in each block to be 100, and then gradually reduced this number (through iterative multiplication by 0.95) until the system in equation 1 was not rank-deficient and factorization converged.

We combined local intensity peaks and local correlation coefficients to initialize W (and used a constant value to initialize X); and approximately solved equation 1 using alternating least-squares (Berry et al. 2007), with at least 10 iterations, and at most 100 iterations or until numerical convergence (defined as a change in the value of the residuals < 0.001).

We imposed spatial and temporal constraints to regularize this factorization, including mean-amplitude normalization of each cell; hard spatial constraints: retaining the largest connected segment within a static 12 μm diameter sphere (centered on a local-intensity peak); and soft sparseness constraints: a sparse projection of the spatial footprint for each cell using the algorithm of Hoyer (Hoyer 2004), with sparseness,

$$\text{sparseness}(W_i) = \frac{\sqrt{n} - \sum_j |W_{ij}| / \sqrt{\sum_j |W_i|^2}}{\sqrt{n} - 1} \quad \text{(eq. 2)}$$

set to be at least equal to the spatial sparseness of a binary 6 μm diameter sphere (these constraints were not applied to the model of the background signal).

We clustered segmented cells into functionally relevant components in two steps. First, we used non-negative matrix factorization to reduce the time series for all segmented

cells in the brain into low-dimensional components. Specifically, for k cells, t timepoints, and $m = 60$ components, we factorized

$$H_{(k \times t)} \approx S_{(k \times m)} T_{(m \times t)}$$

where H are time series for all segmented cells in the brain, while S and T are the spatial and temporal low-dimensional components. These components need not be spatially localized, so we substituted local intensity-based initialization for nonnegative double SVD method (Boutsidis and Gallopoulos 2008) and imposed no spatial constraints on this factorization.

Second, we detected components in this reduced representation. We deemed a component to be functionally relevant when it contained cells with similar activity patterns and showed robust and reproducible anatomical structure across fish. In contrast, noise components lacked clear spatial structure or were not reproducible across fish.

To evaluate reproducibility, we constructed an average brain template, independently for neurons and astroglia, using the nonlinear registration tool *antsMultivariateTemplateConstruction2* (Avants et al. 2010). We registered the spatial component of each fish to this template, and did semi-automated clustering across all components of all fish. We clustered spatial components by binning adjacent voxels of each component, computing the correlation coefficient between all components, thresholding the correlation matrix, and clustering the thresholded correlation matrix using the clique percolation method (Palla et al. 2005), an algorithm that can flexibly assign each component to more than one cluster or to no clusters. We manually fine-

tuned this initial clustering by excluding components from clusters if the average spatial correlation of the component with the cluster was too low, and including the component if the average correlation of the component to all components within the cluster was sufficiently high. This step yielded 10-20 neuronal and astrocytic clusters. All components within each cluster were averaged, smoothed, and warped to individual fish space. Figure 3.x shows the 10 group-average components with highest p values.

To avoid misalignment of group-average components in individual fish, we used an additional nonnegative matrix factorization step, which aligned the components more tightly to each fish. Specifically, we refactorized equation 3, with S initialized by and constrained to be within the binary mask of each group-average component. This added step allowed us to combine the consistency of components across multiple fish with the individual spatial variation of components within each fish. Finally, we averaged the activity of cells within the spatial mask of each component, and compared this average across active and passive states.

Analysis of component and cell activity around passivity onset

We related neuronal and astrocytic component and cell dynamics to behavior by upsampling all calcium signals to 10 Hz, and registering them to passivity onset, and to the midpoints of bouts preceding this onset. As timings of individual bout sequences varied (relative to passivity onset) across trials, we registered bouts by averaging the relative times of bout sequences across trials and fish and linearly interpolating between individual-trial and average bout-sequence times.

This approach allowed us to study average activity of each component and cell relative to passivity onset. We estimated the increase in calcium during and after passivity onset by comparing a sliding 1 s window of Δf/f to the baseline, defined as the average over 10 to 5 s before passivity onset. We computed the significance of any increases in calcium by one-tailed Wilcoxon signed-rank test across trials. At this exploratory stage, we sought to identify candidate components and cells associated with passivity onset by computing $-\log(p \text{ value})$, where p values from the Wilcoxon rank-sum were averaged between 1 s to 4 s after passivity onset. We further analyzed the temporal profile of activity of neurons and astroglia close to passivity onset at the single-cell level, by averaging activity of each segmented cell within a one-second window centered on the peak of each bout, and fitting an exponential function to the activity averaged over the last five bouts before passivity onset (Figure 6A). We interpreted the best-fit exponent of the cell as the rate at which single-cell fluorescence increased before the fish became passive.

***In situ* hybridization**

Zebrafish larvae at 6 dpf were euthanized with an overdose of MS-222 (tricaine) and fixed overnight in 4% PFA-PBS, pH 7.4 at 4°C. Fish were dissected to expose the brain and processed for whole mount *in situ* hybridization (WISH) using the RNAScope technology by manufacturer protocol (Gross-Thebing et al. 2014). The adra1Bb custom probe was designed by the manufacturer and used on transgenic *Tg(gfap:GCaMP6f fish)*. Fish were then mounted in Vectashield (Vector Laboratories, Burlingame) and

imaged on a Zeiss 880 upright confocal microscope with a 25x water immersion objective.

Immunohistochemistry with expansion microscopy

Tissue preparation

Fish brains were dissected out in PBS and fixed in 4% PFA-PBS, pH 7.4 overnight at 4^{o}C, then rinsed well with PBS before antibody labeling.

Antibody staining

Brains were incubated in blocking buffer (10% goat serum, 0.8% Triton X-100 in PBS) overnight at 4^{o}C. Brains were then incubated with primary antibodies chicken anti-GFP (Aves, GFP-1020) and rabbit anti-dsRed (Clontech, 632496) diluted 1:500 in blocking buffer, for 2 days at 4^{o}C, followed by washing in wash buffer (0.3% Tween 20 in PBS) 5x 30 mins at room temperature. Brains were incubated in fluorescent secondary antibodies goat anti-chicken Alexa Fluor 488 (Invitrogen, A11039) and goat anti-rabbit Alexa Fluor 594 (Invitrogen, A11037) diluted 1:500 in blocking buffer, for 2 days at 4^{o}C, followed by washing in wash buffer 5x 30mins at room temperature. Brains were then washed and stored in PBS. All antibody staining steps included shaking.

Expansion

Expansion was done as described (Tillberg et al. 2016) (see also Freifeld et al., 2017)Freifeld et al., 2017). AcX was resuspended at 10mg/mL in anhydrous DMSO, aliquoted, and stored desiccated at –20^{o}C for up to several months. AcX aliquots were diluted 1:100 in PBS to produce anchoring solution just before use. Specimens were

incubated with at least 100-fold volume excess of anchoring solution, at room temperature overnight, protected from light, without shaking.

Gelation solution (8.6% (w/v) sodium acrylate, 2.5% (w/v) acrylamide, 0.15% (w/v) bisacrylamide, 2M sodium chloride, 1xPBS, 0.01% (w/v) 4HT, 0.2% (w/v) TEMED, and 0.2% (w/v) APS in milliQ water) was prepared as follows: all components except 4HT, TEMED, and APS were mixed to produce StockX, which was aliquoted and stored at -20^{o}C for up to several months. Aliquots were thawed and chilled to 4^{o}C, and then 4HT, TEMED, and APS were added from concentrated stocks (0.5% (w/v) 4HT, 10% (v/v) TEMED, 10% (w/v) APS) just before use. Specimens were incubated with at least 100-fold volume excess gelation solution 2x 10min at 4^{o}C.

During the incubation in gelation solution, chambers were prepared by applying adhesive silicone gaskets (ThermoFisher Scientific, P24743) to plain glass slides and coating the glass bottom of each well with 1uL poly-lysine coating solution (poly-lysine solution (Ted Pella 18026) with photo-flo (EMS 74257) added up to 0.2% (v/v)), leaving at least 5 min for poly-lysine coating solution to dry onto glass.

Following incubation in gelation solution, specimens were transferred to the middle of chambers, where they adhered to the poly-lysine treated surface, leaving at least 2 mm between each specimen and the chamber wall. Excess gelation solution was removed and replaced with 36 μL gelation solution for each 9 mm diameter chamber. Chambers were sealed with cover glass, which forms a seal with the silicone gasket under gentle pressure. Care was taken to avoid bubbles within 2 mm of specimens. Chambers were

then held at 37°C for 2 hours to gel and cure specimens. Chambers were moved to 37°C within 30 min of adding APS to the solution to prevent premature gelation. After gelation, chambers were brought back to room temperature and disassembled. Top cover glass and silicone gaskets were carefully removed, leaving gels adhered to glass slides. Gels were trimmed using a razor blade to a right trapezoidal shape to aid in post-expansion orientation of the specimen. Several microliters of digestion buffer (0.5% (w/v) Triton X-100, 500 mM sodium chloride, 1 mM EDTA, 50 mM Tris pH 8) were applied around the edge of each gel to de-adhere them from the glass surface. Proteinase K (New England Biolabs, P8107S) was added 1:100 to digestion buffer to produce digestion solution. Gels were incubated in at least a 100-fold volume excess of digestion solution overnight, at room temperature, with shaking. Following digestion, gels were washed several times in PBS and kept at 4 °C until further use.

Expansion and imaging

Gels were expanded by washing in water and imaged on a Zeiss Z1 light sheet microscope with standard settings.

Name	Formal name	Supplier	Cat #
AcX	Acryloyl-X, SE, 6-((acryloyl)amino) hexanoic Acid, Succinimidyl Ester	ThermoFisher Scientific	A20770
Sodium acrylate	Sodium acrylate	Sigma	408220
Acrylamide	Acrylamide	Sigma	A9099
Bisacrylamide	N,N′- Methylenebisacrylamide	Sigma	M7279
4HT	4-Hydroxy-TEMPO	Sigma	176141
TEMED	N,N,N′,N′-Tetramethylethylenediamine	Sigma	T7024
APS	Ammonium persulfate	Sigma	A3678

Table 3.2. Materials used specifically for expansion microscopy.

RNA sequencing

Cell isolation, library preparation, and sequencing

Neurons and astroglia were isolated using methods of (Hempel et al. 2007) with minor modifications. Fish were euthanized with 1:30 dilution MS-222/Tricaine in external solution, then placed on ice. Brains were dissected in 1:30 dilution of MS-222/Tricaine in external solution, then digested with Liberase-DH (1 mg/mL; Roche) in external solution for about 1 hour. Digested brains were washed three times in external solution with 1:30 dilution of MS-222/Tricaine. Digested brains were triturated as described (Hempel et al. 2007) in external solution containing Tricaine and 2% fetal bovine serum. Cells were isolated by hand. About 300 cells were collected for each sample and lysed in 50 µl PicoPure extraction buffer. RNA was extracted and libraries were prepared as described (Cembrowski et al. 2016). Briefly, cDNA was prepared from DNAse-treated RNA using Ovation RNA-seq v2 kit (NuGEN). Barcoded libraries were prepared with Ovation Rapid library kit (NuGEN) and sequenced on a HiSeq 2500 to a depth of about 40 M reads per sample with single-end 100 bp reads.

Gene expression estimation

Sequencing adapters were trimmed from the reads using cutadapt (DOI: http://dx.doi.org/10.14806/ej.17.1.200). Trimmed reads were aligned to danRer10 Refgene transcriptome (UCSC). Gene expression estimates were reported as transcripts per million.

Chapter 4: Time- and space-efficient baseline calculation for large functional imaging datasets

Abstract

Constant advances in bioimaging tools enable researchers to image biologically relevant phenomena faster, longer, and at higher resolution. In turn, imaging experiments are producing larger and larger datasets, which pose unique challenges for data analysis due to their scale. These challenges are particularly acute for functional imaging experiments using light sheet microscopy. Light sheet microscopy datasets are often so large that necessary image preprocessing steps must be extensively parallelized, but parallelizing the specific preprocessing operations required for functional imaging requires a data repartitioning step that is particularly inefficient and hard to scale. This data repartitioning step stems from the need to estimate the baseline fluorescence in functional imaging datasets. To overcome the barrier to scalability posed by data repartitioning, we present a strategy for approximately estimating the fluorescence baseline from large imaging datasets that avoids this inefficiency. This strategy enables faster, scalable, and more flexible processing of large volumetric fluorescence data.

Introduction

Functional fluorescence imaging via light sheet microscopy is a powerful method for observing dynamics in large populations of excitable cells. In the ideal scenario, an experimenter collecting functional imaging data would have easy access to biologically meaningful results from the data with the minimum effort and latency. However, both the

computationally demanding nature of functional imaging datasets and their size pose barriers to rapid analytics.

Preprocessing functional imaging data

Parsing functional imaging data is intrinsically computationally demanding: for functional imaging data, raw images alone are not highly informative without extensive preprocessing (Fig. 4.1A-C). Intensity values in raw images indicate the quantity of excited fluorophores, but the units of interest for functional imaging are *percent change over baseline fluorescence*, or Δf/f, where the denominator *f* denotes baseline fluorescence, and the numerator Δ*f* denotes the difference between the raw fluorescence and *f*. Without normalizing by the fluorescence baseline, inactive cells that express a large quantity of fluorophore appear brighter than dimmer, more dynamic cells (Fig. 4.1). After calculating Δf/f, those silent cells will appear dim while the fluctuations of active cells will be bright (Fig 4.1). Converting a raw fluorescence image to a Δf/f image requires estimating the baseline fluorescence *f*, which is a time-domain statistic estimated by aggregation of potentially hundreds of other images (time points). Because the concentration of fluorophores in a cell can drift during imaging (e.g., due to bleaching), baseline fluorescence is often modeled as a time-varying quantity—*f* becomes *f(t)*. Done this way, generating a single baseline-normalized image requires a large amount of computation, because baseline must be estimated for each pixel; performing baseline-normalization for an volumetric entire dataset requires proportionally more computation. An additional complication is that movement of the sample that occurred during image acquisition will produce strong artifacts after

baseline normalization, so it is best to correct for sample motion *before* baseline normalization, e.g. by generating a template image and shifting each image to best match the template. Both estimating and correcting sample motion are computationally intensive. So, thinking concretely about an experimenter who has just collected a functional imaging dataset: before the experimenter can see the data in the units of interest (Δf/f), each image must be first motion-corrected and then normalized by the baseline fluorescence (Fig 5.). For small datasets, e.g. those that fit in random-access memory (RAM) on a single workstation, these computations may take time but don't require extensive data engineering; but when datasets become extremely large, these computations can become extremely burdensome to the extent that significant that new computational tools and strategies are needed.

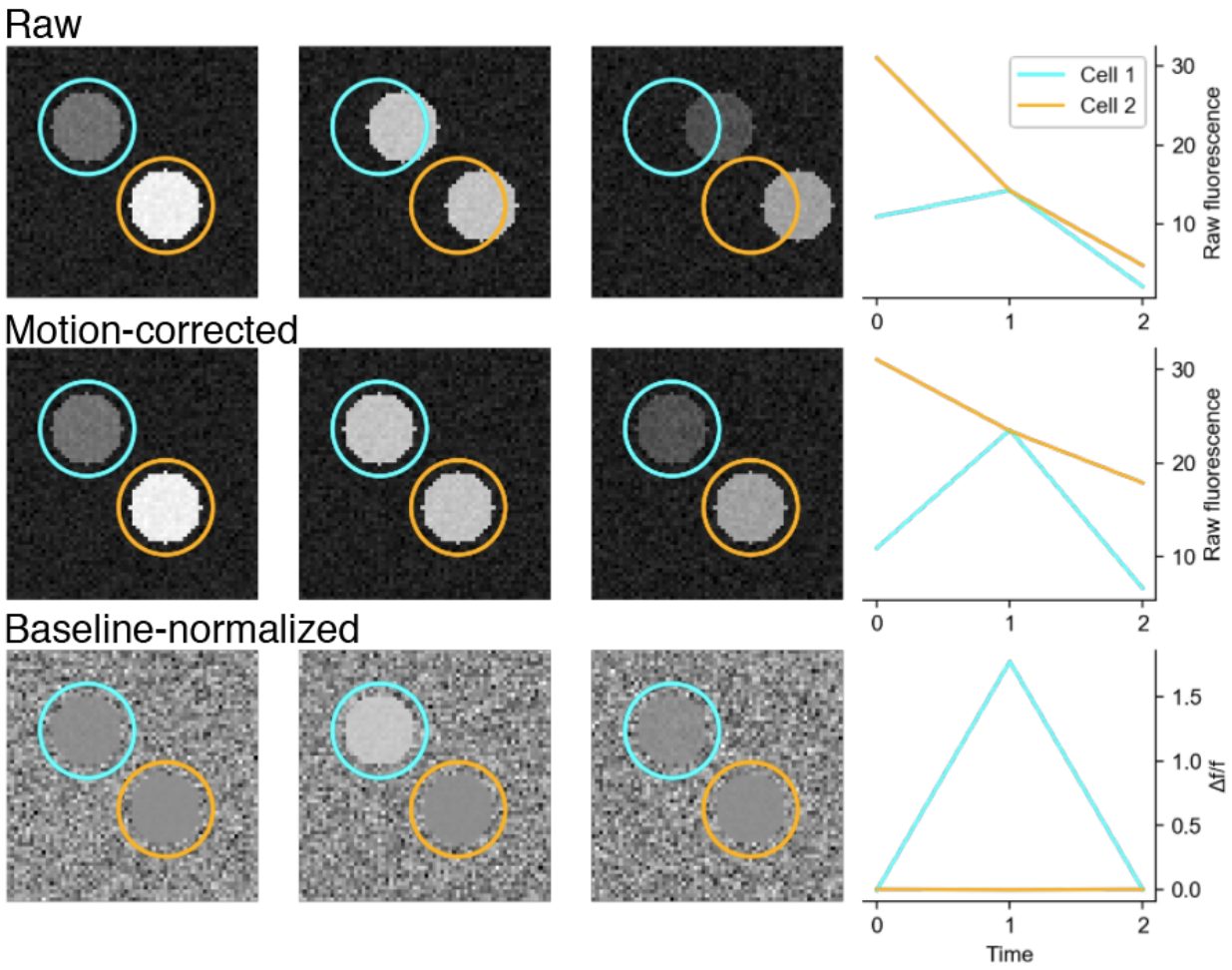

Figure 4.1. Schematized preprocessing for functional imaging data
The synthetic dataset is a sequence of three images of two “cells”. The top cell has a dim baseline, but has fluctuations relative to this baseline; the bottom cell has a bright baseline but no fluctuations. The left column shows the timeseries generated by taking the average of the pixels in regions of interest (ROI) drawn around the two cells in the first frame. The first row shows raw data, which are corrupted by sample motion and a progressive decrease in the fluorescence baseline, which emulates photobleaching; these artifacts are represented by the steadily decaying traces in the timeseries, which is what an experimenter would see during or after an experiment. The second row shows raw data after motion correction. Now the ROI are centered over the cells, but the timeseries are still corrupted by photobleaching. The last row shows data after baseline normalization. The fluctuations in the top cell are emphasized, as is the static nature of the bottom cell. This final representation is what the experimenter needs in order to evaluate the success or failure of the functional imaging experiment.

The unusually high bandwidth of light sheet microscopy

Light sheet microscopes acquire 4 megapixel images at up to 100 Hz, which corresponds to a peak data rate of ~820 megabytes (MB) per second, per camera. At this rate, the volume of data collected in 20 minutes (typical for a functional imaging experiment) will easily exceed the random-access memory of a high-performance computer workstation. The rate at which light sheet microscopes generate data is more than an order of magnitude greater than that of pre-existing functional imaging modalities. Raster-scanning microscopes with resonant galvanometers acquire .26 megapixel images at 20-30Hz, corresponding to a peak data rate of ~15 MB per second, per detector, or 1/50th the peak data rate of a light sheet microscope. Datasets from raster-scanning microscopes can be processed entirely on a single workstation, but the same is not true for light sheet microscopy datasets—because the data rate of light sheet microscopy is so much higher than for previously established imaging modalities, new tools and techniques are needed for processing the data.

Computational strategies for processing large imaging datasets

Image processing often involves repeating the same algorithm or computation on different parts of a dataset. When these computations are independent of one another, they can be processed in parallel, given sufficient computational resources to do so. Light sheet microscopy datasets present ample opportunity to leverage parallelized computation. For example, sample motion correction can be independently estimated for each time point, and thus this computation can be parallelized across the time axis of the data. Baseline normalization can be independently performed for each pixel, so

this computation can also be parallelized, but across the space axes of the data. So, how should we implement these parallelizable computations? I will first discuss two general approaches to parallel computing, ordered by increasing complexity: first, running preprocessing code on a powerful single workstation; second, running preprocessing code on a compute cluster. I will then schematically outline the existing approach for preprocessing light sheet functional imaging data on a compute cluster, and identify limitations of this approach that will be addressed by the present work.

Parallel image processing on a single workstation

The simplest approach is to run preprocessing software on a single workstation with a large number of central processing unit (CPU) cores, each of which supports independent computation; as of this writing, it is possible to purchase workstations with tens or hundreds of independent CPU cores. Besides the simplicity of working on a single computer, a strength of this approach is that analysis software can be written in such a way that all CPU cores can access the same pool of memory within a single program. However, this approach has a fundamental drawback: one cannot scale up the compute capacity of a single workstation. Once a program saturates all CPU cores on workstation, there is no way to dynamically add more capacity. This limitation is particularly unfortunate for functional imaging preprocessing, where the datasets, and thus the concomitant computational load, are constantly growing larger.

Parallel image processing on a compute cluster

An established solution to the scaling problems described above is to run programs on a distributed system of many interconnected computers sharing a single file system (a

"compute cluster"). This paradigm, termed "distributed computing", enables dynamically scaling computational resources beyond the limits of a single workstation—on a compute cluster, it's trivial to harness thousands of CPU cores to execute computations in parallel. But this scalability comes at the expense of a more complex and restrictive programming model. Because the cluster is composed of many separate computers, software designed to work in this context cannot assume that all CPU cores share the same memory space. But for extensively parallelizable problems that are CPU-limited (like most of the preprocessing required for functional imaging datasets) the added complexity is dwarfed by the huge gains in scalability. Parallel programs designed to run on a distributed computing infrastructure can, if designed properly, also run on a single workstation with multiple cores, but the inverse is not necessarily true: a parallel program designed to run on a single workstation (with a shared memory pool) may be very difficult to transfer to a distributed computing environment. Given this asymmetry, and in the interest of generality, subsequent discussion will assume that parallel computations are executed on individual CPU cores in a distributed context, i.e. without the assumption of a shared memory pool. Also in the interest of generality I will hereafter use the term "worker" instead of "CPU core" to denote a unit capable of independent parallel computation. In the following section I will describe a simple workflow for performing vital preprocessing (motion correction and baseline normalization) of functional imaging data in parallel. Without any optimizations, this workflow works for relatively small datasets, but it scales poorly and has some deep inefficiencies. Resolving some of this inefficiency is the focus of this work.

Parallel preprocessing for functional imaging

Functional imaging preprocessing typically begins with operations that are independent for each image, such as applying denoising filters, applying geometrical transformations to images to correct geometrical distortion induced by data acquisition, as well as estimating and or correcting for sample motion. Because these operations are independent for each image, they can be easily parallelized in a scheme where each worker loads an image (or collection of images) from storage and processes them accordingly (Fig. 4.2A). When the dataset is distributed in this way, the spatial axes of the dataset are local to each worker and the temporal axis is distributed across workers (Fig 4.2A). After various per-image operations, the data must be baseline-normalized. Like motion correction, baseline normalization is also parallelizable computation, but along a different axis of the data: for baseline normalization, the computation is independent for each *time series*, i.e. each the spatial temporal axis of the data needs to be local to each worker, while the spatial axes must be distributed across workers (Fig 4.2C). Between distributed processing of images and distributed processing of time series the allocation of data to the workers must drastically change. This procedure, termed “data repartitioning”, requires transfer of data between workers, e.g. by each worker writing and reading data to a shared file system (Fig 4.2B, D). Once data have been repartitioned and the dataset is distributed along the spatial axes, each worker can perform baseline normalization in parallel (Fig 4.1C). At this point the baseline-normalized time series can be saved to disk, collected to a single workstation, or re-repartitioned into images for tasks that require parallel processing of baseline-

normalized images (e.g., making a maximum z-projection for each time point) (Fig 4.2E).

The workflow I have just described has two major problems. The first is the data repartitioning step between image processing and time series processing (Fig 4.2B). Data repartitioning between workers is slow and brittle—reading and writing many small files to disk is slow, and a single crashed worker during repartitioning can be fatal to the entire process. Additionally, the complexity of data repartitioning grows supra-linearly with data size. Thus, any strategy to avoid data repartitioning is desirable for efficient and scalable data processing of large imaging datasets. Second, because of the time-domain implementation of baseline normalization, getting a single baseline-normalized image at some time index *t* strongly depends on images in a range of time indices above and below *t*. For functional imaging in larval zebrafish, a single baseline-normalized image depends on a temporal window of hundred images. This can be seen schematically Figure 4.2E, where each baseline-normalized image depends on the output of all parallel workers. So, in addition to the time required for data repartitioning, in a real dataset there is also a substantial temporal cost due to loading hundreds of images from disk just to yield a single image as output.

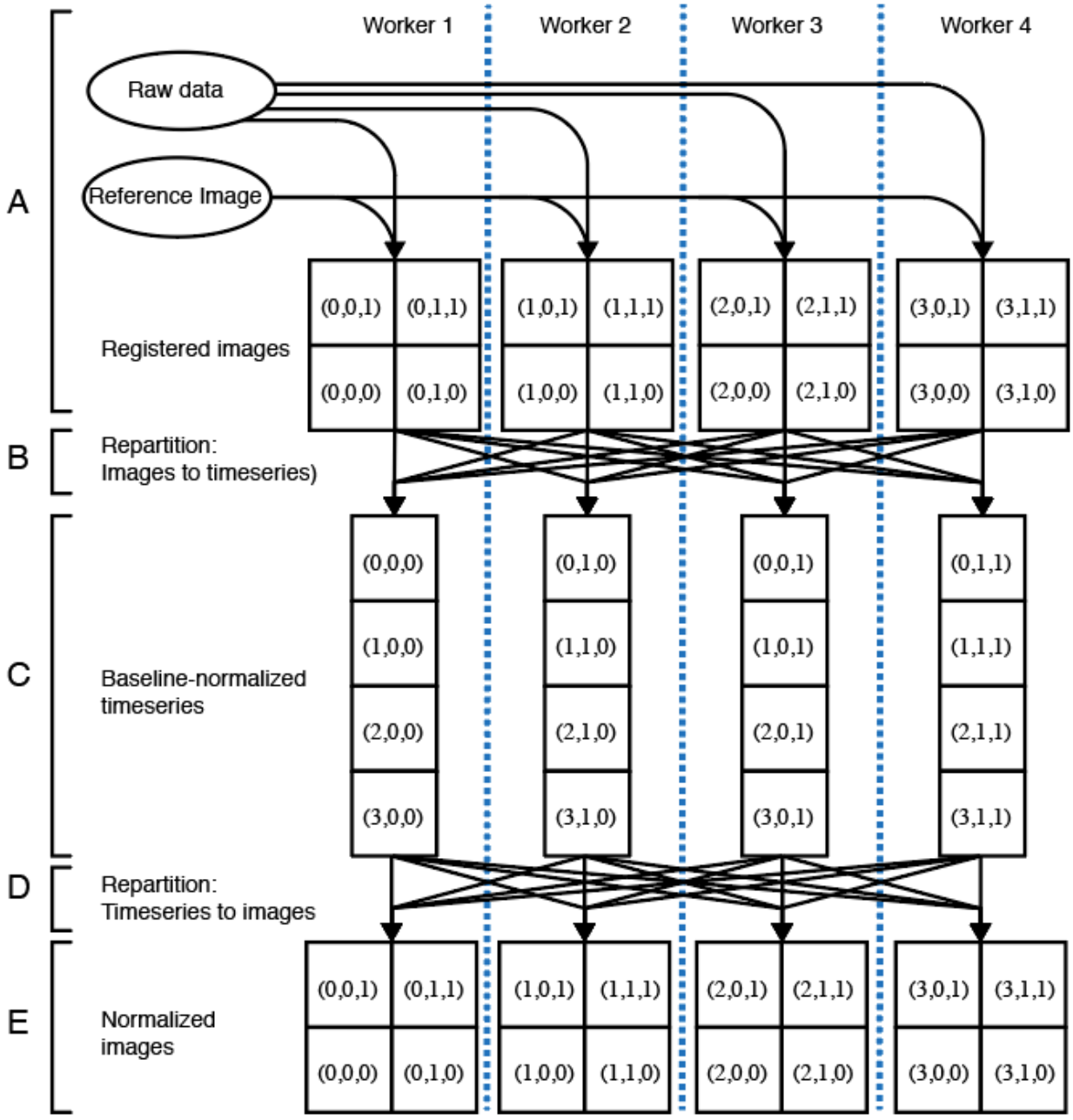

Figure 4.2. The typical scheme for converting raw fluorescence images to baseline-normalized images in parallel.
In this diagram, the dataset is composed of 4 two-dimensional images, each with 4 pixels. Each small square represents a pixel, and is labelled with a length-3 tuple that denotes the (t, x, y) coordinates of the pixel in the dataset. Computation is distributed across workers, each of which is given a column in this diagram. Communication between workers is represented by lines with a horizontal component that traverse column boundaries. **(A)** Raw data is loaded from disk and allocated to each worker. A single reference image is also loaded from disk and allocated to each worker for use as a target in motion correction. Motion correction is an in-place transformation of the raw

Figure 4.2 (continued) data. **(B)** Data repartitioning: prior to baseline normalization, registered images must be broken apart and distributed across the population of workers. This is computationally onerous. In the worst case, each worker must send data to each other worker. The complexity of this operation scales supra-linearly as datasets become longer in time. **(C)** After data repartitioning, each worker has an entire timeseries, and the fluorescence baseline can be estimated and used for normalization. **(D)** A second round of data repartitioning is necessary to convert the distributed collection of timeseries into a distributed collection of images. **(E)** The final result is a distributed collection of baseline-normalized images.

In order to mitigate these problems, we describe a technique, which we call “baseline compression”, that avoids excessive data repartitioning in distributed functional imaging preprocessing workflows by exploiting the slow temporal structure of the fluorescence baseline. Instead of estimating the baseline fluorescence for every time point, we instead estimate the baseline for a sparse, evenly-distributed subset of time points, and then save this down sampled baseline to disk. For subsequent baseline normalization, the baseline for every time point can be estimated independently by interpolating the compressed baseline, which practically entails loading a few images from disk. Thus, via baseline compression, we can avoid the inter-image dependencies and concomitant data repartitioning present in the simple parallel preprocessing workflow presented above. The result is faster preprocessing of functional imaging data, but this comes at the expense of accuracy.

Results

Baseline compression of single pixels

The parallel preprocessing workflow illustrated in Figure 4.2 is inherently limited in terms of performance and scalability. To address these issues, we were motivated to find a way to dynamically perform baseline normalization without extensive data repartitioning,

i.e. we wanted a way to perform baseline normalization independently for each image. A conceptually simple solution would be to compute the full baseline once, save the resulting baseline images to disk—i.e., complete the computational graph shown in Figure 4.2—then load the baseline images as needed for subsequent normalization. However, in practice this approach would demand extensive data duplication, which may be undesirable—for each image, the baseline of that image would need to be saved to disk, thereby doubling (at a minimum) the storage footprint of the dataset. For datasets that routinely measure over half a terabyte, data duplication must be minimized. However, if we could generate a *compressed* version of the fluorescence baseline and save it to disk, one could then use this compressed baseline to generate reconstructed individual baseline images when needed without duplicating the entire dataset. These reconstructed baseline images could then be used for normalizing the corresponding raw fluorescence images. How could one compress the baseline? The fluorescence baseline varies slowly in time, as the chief drivers of baseline fluctuations are photobleaching and changes in cell state, both of which occur at a relatively slow timescale. With this in mind, it should be possible to represent the dynamics of the full baseline by downsampling and interpolating between a relatively small number of time points. Thus, we decided to test the following procedure: first, for each pixel, calculate the baseline fluorescence at a small set of evenly distributed time points, and save these points as well as the subsampled baseline to disk in a file format that allows fast reading from arbitrary array regions (e.g., raw binary or hdf5). Then, to convert a raw image from time index t to a baseline-normalized image, we load the baseline images i

and *i + 1,* where *i* denotes the index of the subsampled time point that precedes time index *t.* To linearly interpolate, a weighted average of the two baseline images is computed based on the relative position of raw image time index *t* in the interval *(i, i + 1)*. The resulting reconstructed baseline image is then used to divisively normalize the raw image.

This plan would fail if compressing the fluorescence baseline by downsampling could not generated a usable reconstructed baseline. So, my first tests concerned whether the fluorescence baseline could be compressed via downsampling and reconstructed. Working with a test dataset, we compared the full fluorescence baseline, estimated using a sliding window percentile filter, with a compressed baseline, estimated by downsampling the full baseline by a factor of 250, i.e. 1 sample every 150 s. We made this comparison for a few sample pixels from a light sheet microscopy dataset wherein the whole brain of a larval zebrafish was imaged at 1.7 Hz (Figure 4.3A). Single pixels are the smallest and noisiest elements in a light sheet imaging dataset, and any downstream analysis pipeline of light sheet data will involve aggregation of data across many pixels; therefore, any large systematic errors observed at this stage would be a clear sign that we could not proceed further with our method. Fortunately, this initial diagnostic indicates that the full baseline and the downsampled baselines are qualitatively very similar, without large systematic errors, regardless of whether the pixels collected fluorescence emitted from an active cell or inactive tissue (Figure 4.3B,C). The full baselines are very slowly varying, likely due to the very low rates of

photobleaching in by light sheet microscopy. Because the baselines vary so slowly, a relatively small number of points is sufficient for a veridical reconstruction.

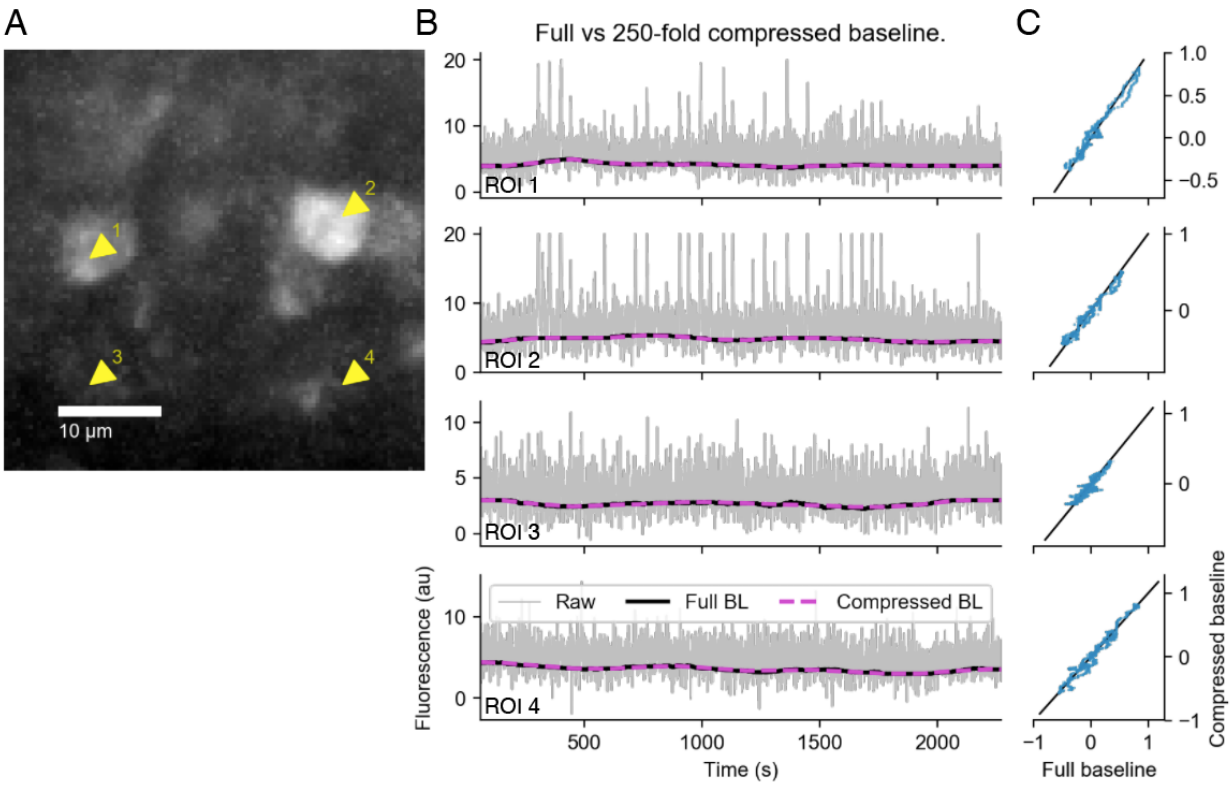

Figure 4.3. The fluorescence baseline from individual pixels in a light sheet microscopy dataset can be approximated by downsampling and linear interpolation. Fluorescence data was recorded from a Tg(*elavl3:GCaMP6f;gfap:jRGECO1b*) fish. Data shown are from the neuronal channel of the raw data. The full baseline, estimated with a windowed percentile filter over a five-minute window, was compared to the compressed baseline, which was constructed by downsampling the full baseline by a factor of 250 and linearly interpolating to obtain intermediated values. **(A)** Four pixels are chosen as ROI from a single plane in a volumetric light sheet dataset. **(B)** For each of the four ROI indicated in (A), the timeseries of that ROI is plotted in gray; the full baseline is plotted in black, and the reconstructed compressed baseline is plotted in magenta. **(C)** For each ROI in (A), the full baseline and the compressed baseline are mean-subtracted and plotted against one another. In both (B) and (C), the full baseline appears qualitatively similar to the compressed baseline.

Baseline compression of a small region of interest

Continuing the qualitative evaluation, we next considered every pixel in the ROI that contained the four pixels displayed in Figure 4.3. It would not be possible to display the full baseline and the downsampled baseline for thousands of pixels, so instead we performed baseline normalization using the full baseline and the compressed baseline for every pixel in the ROI and examined a sample frame, the maximum intensity over time, and the minimum intensity over time (Fig. 4.4). For all these image-domain diagnostics, the baseline-normalized images look qualitatively identical regardless of whether the full or downsampled baseline was used for normalization. This again suggests that the compressed baseline, once reconstructed, is a workable approximation of the full sliding window baseline.

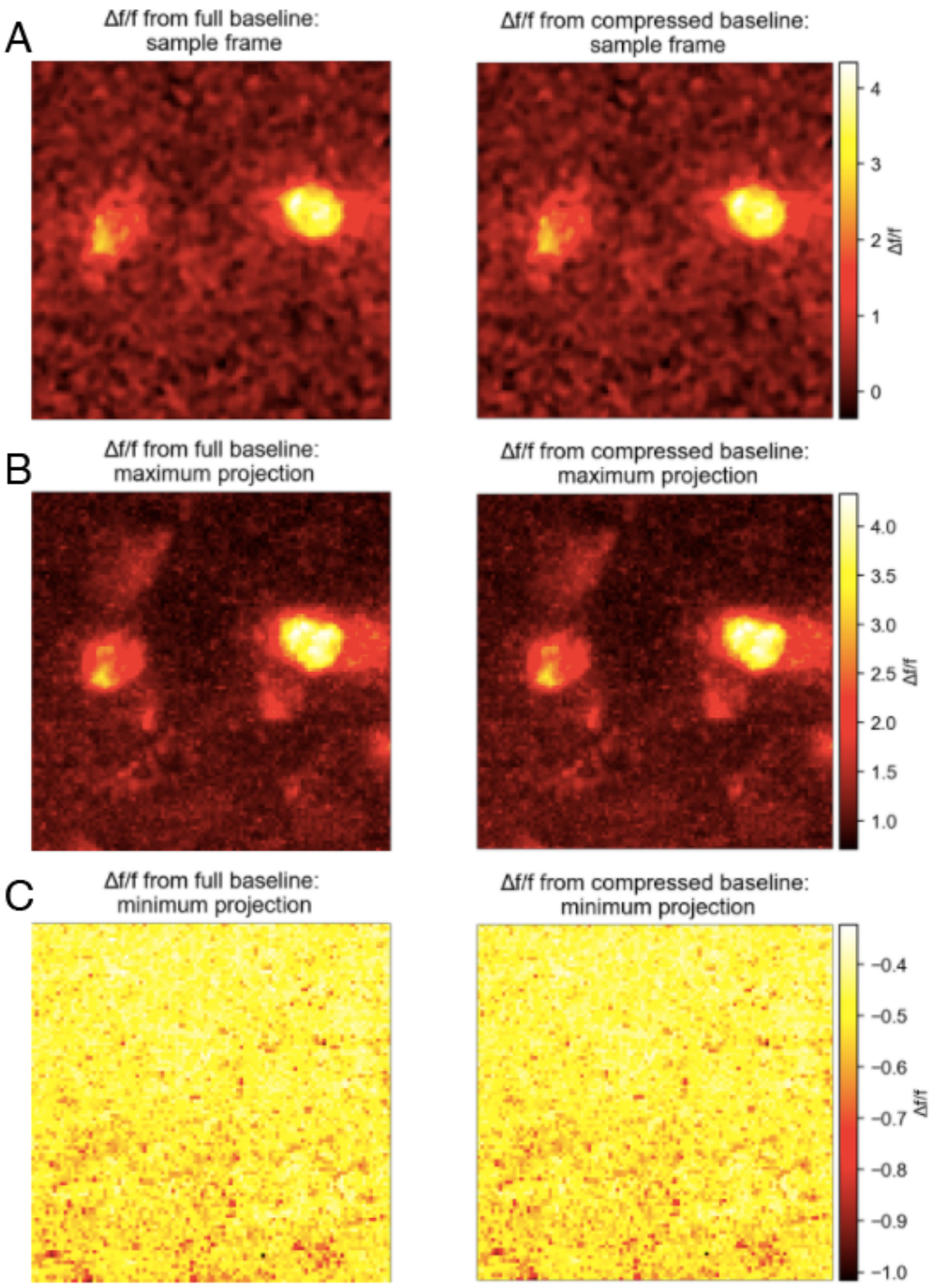

Figure 4.4. Baseline-normalized images obtained using the compressed baseline are qualitatively identical to the baseline-normalized images obtained using the full baseline. The ROI used here is the same as that used in Figure 4.3 **(A)** A sample baseline-normalized image, generated using both methods. **(B)** The maximum intensity projections over time. **(C)** The minimum intensity projections over time.

Baseline compression of full images

Having demonstrated on small datasets that the fluorescence baseline can be compressed through downsampling, the next step was to scale up the procedure to larger datasets and consider the reconstruction error across a large number of pixels. For these tests, calculating the full sliding window baseline for each pixel and then variably downsampling it (as we did in Figure 4.4) would be cumbersome and inefficient, so we devised a scalable technique for calculating the downsampled baseline directly through windowed percentile filters applied on a subset of the timeseries of each pixel. This fast, scalable approach allowed me to generate diagnostics for evaluating the downsampled baseline technique on large datasets.

To demonstrate the generality of the baseline compression approach, we tested it on two functional light sheet microscopy datasets, containing data from three different cell types: zebrafish neurons and zebrafish astroglia, imaged simultaneously in the same animal using two different calcium indicators; and fruit fly (*drosophila melanogaster*) neurons imaged in an explanted brain. The two source datasets are volumetric, but we only analyze a single plane from each dataset in order to generate results which can be easily visualized with a 2D representation. For each cell type, we sought to answer several questions, all of which would be relevant for an experimenter or analyst deciding how to use the baseline compression technique: what range of downsampling values should be used for baseline compression? How does the average and worst-case reconstruction error vary with the extent of downsampling? Is there spatial structure to the average and worst-case errors? For all these diagnostics, we quantify error as the

difference between the full baseline and the reconstructed baseline, normalized by the full baseline. Normalized error is appropriate here because ultimately, a data analyst needs to know how the choice of baseline compression will influence the final baseline-normalized data, and a normalized change in the baseline is directly interpretable as a corresponding change in the baseline-normalized final result.

First, in order to rapidly estimate a useful range of downsampling factors for each dataset, we computed the space-average of the entire dataset and estimated the full baseline of that time series, yielding the average baseline of the entire dataset (Figures 4.5A, 4.6A, 4.7A). This procedure is computationally scalable, since no motion correction is needed and each image can be averaged independently. The resulting mean baseline represents the average slow trend across all pixels. we then downsampled this average baseline with a range of downsampling factors and plotted the normalized error between the full baseline and each downsampled baseline (Figure 4.5B, 4.6B, 4.7B). By examining these plots, one can make an informed, yet computationally cheap, decision about how to balance compression with reconstruction error for the full dataset. For example, in the zebrafish datasets (Figure 4.5A, 4.6A), one can see that the normalized error is low and stable for baseline sampling intervals less than ~180 seconds, while for the fruit fly dataset (Figure 4.7A), which has a comparatively variable baseline, the normalized error stabilizes only for baseline sampling intervals below 8s.

I used these mean-baseline plots to generate a candidate range of downsampling factors, which we then used to create reconstructed baselines. Across these

downsampling factors, we computed the normalized error between each timepoint in the full sliding-window baseline and the reconstructed baseline. This yielded a timeseries of errors for each pixel, which we then summarized by taking the maximum absolute value across time (i.e., the worst-case normalized error) and the mean across time (i.e., the average normalized error). For each level of baseline downsampling, we visualized the average normalized error and the maximum normalized error as histograms (Panel B in Figures 4.5-4.7). For all three cell types, these histograms show that both the mean error shrinks with increasing baseline sampling (as expected). For all datasets, the centers of the mean error distributions were marginally higher than 0; this bias is likely a consequence of applying linear interpolation to the convex baseline timeseries. The maximum error distributions for the two fish datasets (Figures 4.5B and 4.6B, top) also show that the worst-case error shrinks with increased baseline sampling, to below 5% for almost all pixels at the densest level of baseline sampling shown. Because the compressibility of a timeseries depends in part on how noisy it is, pixels from the background of will have noisier timeseries and thus be much less compressible. This can be seen in the spatial maps of mean and maximum errors, which were made using the densest level of baseline sampling for each dataset (Panel C in Figures 4.5-4.7). These spatial error maps reveal that the errors induced by baseline compression are not uniformly distributed in space—in particular, in the zebrafish neuronal error maps, cell-shaped regions of high (~10%) maximum reconstruction error can be seen (Figure 4.5C, middle row), and in the fruit fly error maps, a neurite bundle and a few cell bodies also have relatively high maximum reconstruction error. In both cases, these are

regions where there is uncorrected local tissue motion, and so the baseline appears to change much more rapidly at these pixels than in regions of the image where there was no sample motion. The signals from such regions would not be interpretable after baseline normalization, so the clustered errors here are not troubling. Overall, the conclusion of these diagnostics is that, across a wide range of downsampling values, the reconstructed baselines have sufficiently low error relative to the full baseline that using a compressed baseline is a viable alternative to computing a full baseline.

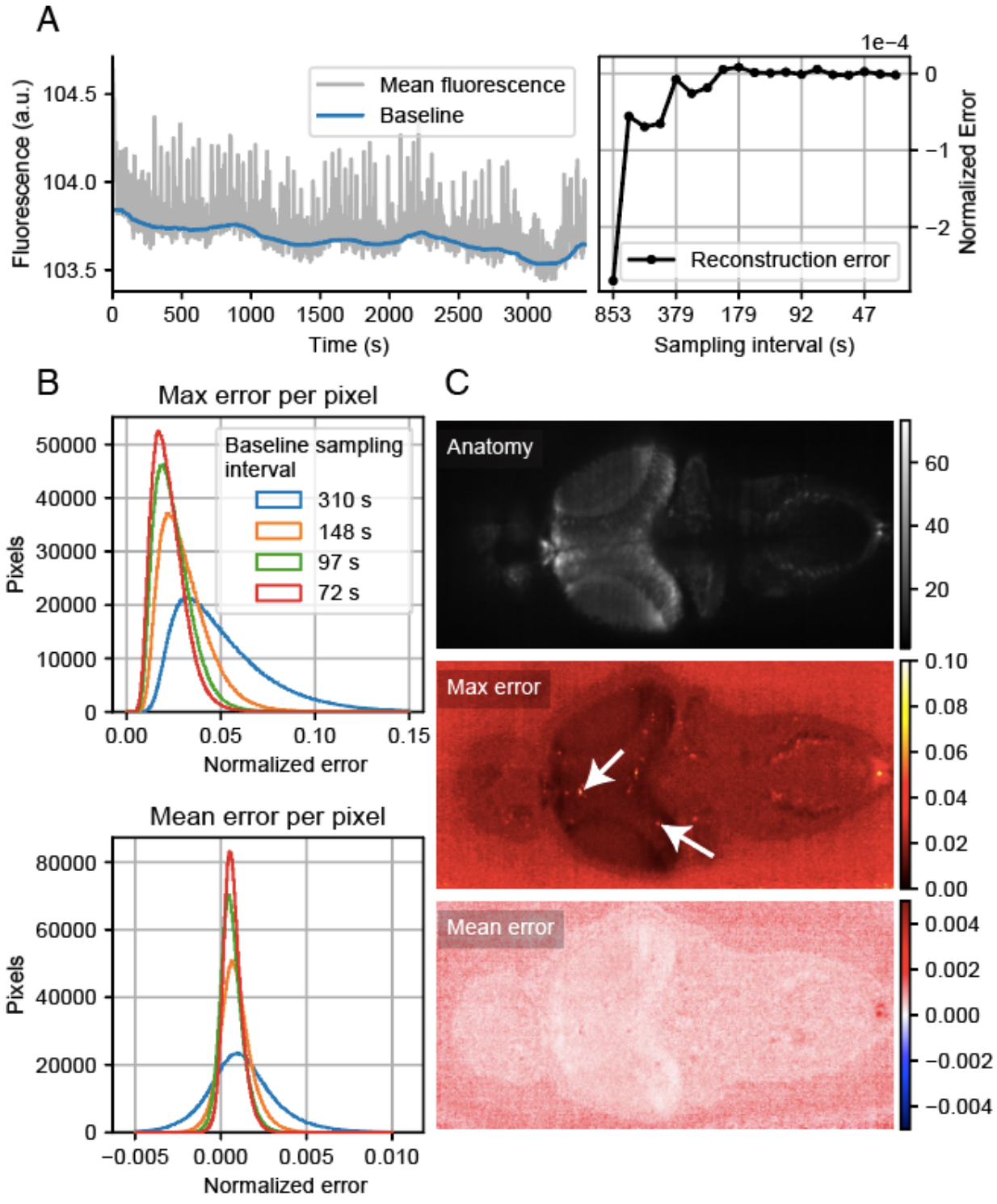

Figure 4.5. Baseline compression applied to functional imaging of neurons in larval zebrafish.
The data are a single plane from a volumetric recording of calcium activity in a Tg(*gfap:GCaMP6f;elavl3:jRGECO1b*) fish. This dataset contains the green channel of the original recording, and thus is only neurons. **(A)** Left: the mean of all pixels, and the

Figure 4.5 (continued) full baseline estimated from that timeseries. Right: the normalized error of reconstructed baselines decreases with increased baseline sampling density. Below 180 seconds the error appears to flatline. **(B)** Histograms of maximum normalized error and mean normalized error for a range of baseline sampling intervals. Both the maximum and mean error distributions shrink as the sampling interval decreases. Below ~90s, the worst-case error is almost entirely less that 5%, and the mean error distribution is almost entirely less than .05% **(C)** Top: a sample image from the baseline, indicating the anatomical structure of the sample. Middle and bottom: spatial maps of the maximum and mean normalized error for the reconstructed baseline using a 72s sampling interval. Arrows in the maximum error map indicate somata that move locally during the imaging session; this movement of single cells induces relatively rapid changes in the fluorescence baseline estimate; these changes are poorly approximated by the reconstructed baseline.

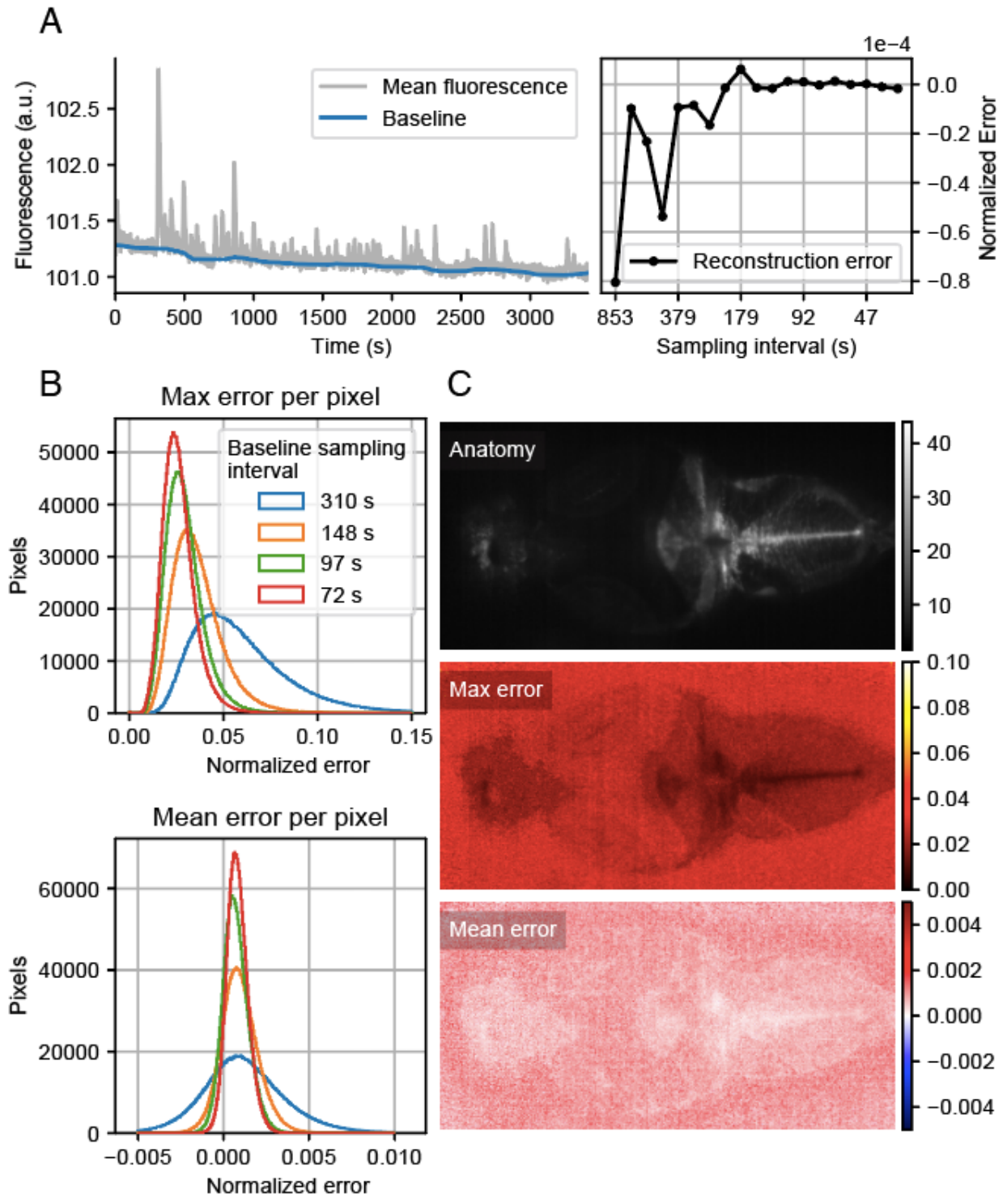

Figure 4.6. Baseline compression applied to functional imaging of astroglia in larval zebrafish.
The data are a single plane from a volumetric recording of calcium activity in a Tg(*gfap:GCaMP6f;elavl3:jRGECO1b*) fish. This dataset contains the red channel of the original recording, and thus is only astroglia. **(A)** Left: the mean of all pixels, and the full

Figure 4.6 (continued) baseline estimated from that timeseries. Right: the normalized error of reconstructed baselines decreases with increased baseline sampling density. Below 180 seconds the error appears to flatline. **(B)** Histograms of maximum normalized error and mean normalized error for a range of baseline sampling intervals. Similar to the neuronal dataset, both the maximum and mean error distributions shrink as the sampling interval decreases. Below ~90s, the worst-case error is almost entirely less that 5%, and the mean error distribution is almost entirely less than .05% **(C)** Top: a sample image from the baseline, indicating the anatomical structure of the sample. Middle and bottom: spatial maps of the maximum and mean normalized error for the reconstructed baseline using a 72s sampling interval. In this dataset, there were no moving cells, so the approximation was uniformly low-error across the high-signal regions of the image.

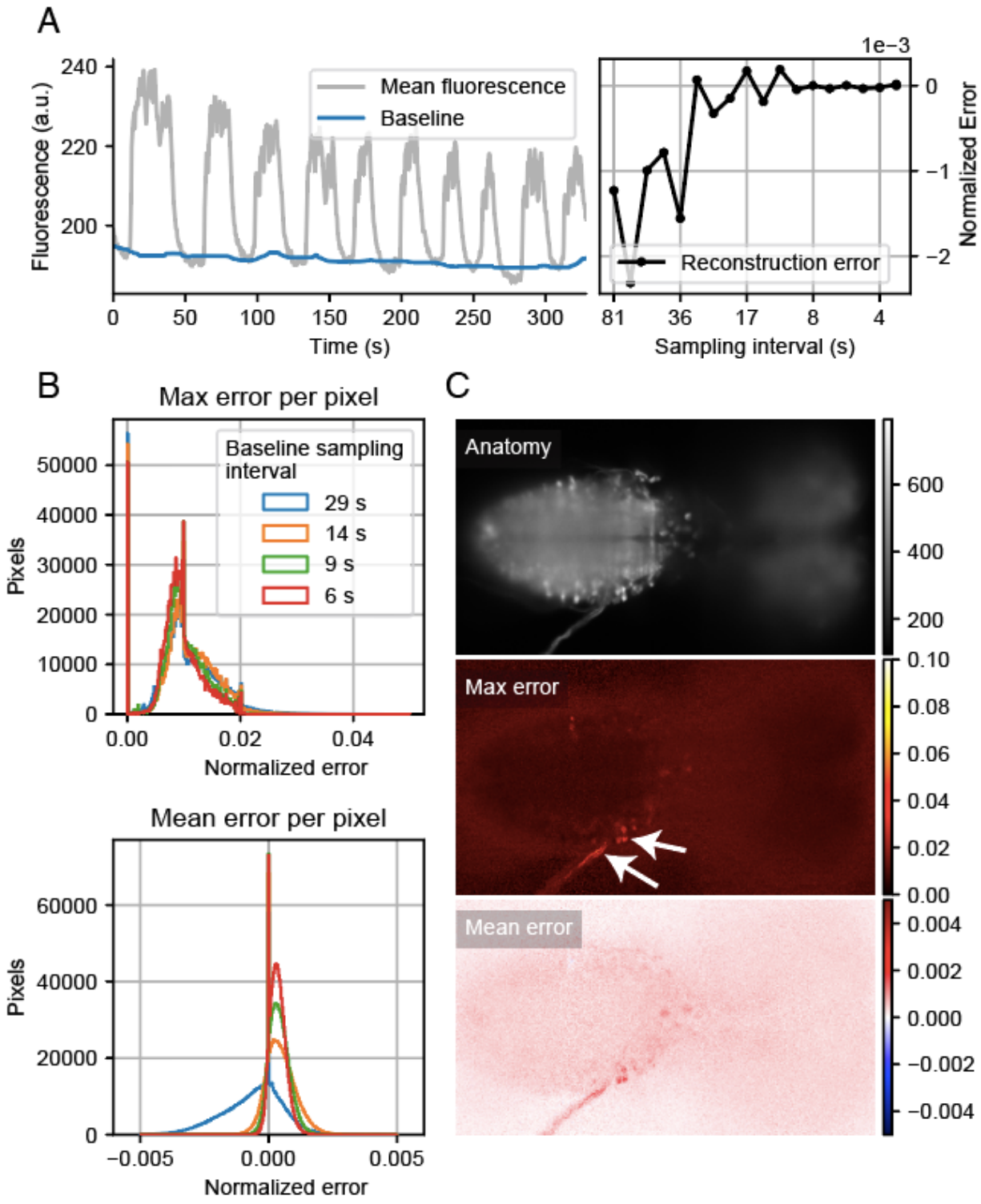

Figure 4.7. Baseline compression applied to functional imaging of a larval drosophila CNS explant.
The data are a single plane from a volumetric recording of calcium activity in a third instar larval CNS from a Tg(*57C10:GAL4,UAS:GCaMP6s*) animal. **(A)** Left: the mean of all pixels, and the full baseline estimated from that timeseries. Right: the normalized

Figure 4.7 (continued) error of reconstructed baselines decreases with increased baseline sampling density. Below 8 seconds the error appears to flatline. The sampling required for the error to stabilize is much denser than for the zebrafish data. **(B)** Histograms of maximum normalized error and mean normalized error for a range of baseline sampling intervals. For this dataset, the maximum error distributions are robust against denser baseline sampling; we are not sure why this is the case. However, the worst-case error is almost entirely less than 2%, and the mean error distribution is almost entirely less than .0025%. The invariant peaks at 0 error in the mean and maximum error distributions are due to background pixels which have their timeseries set to 0; the timeseries of these pixels can be perfectly reconstructed after downsampling. **(C)** Top: a sample image from the baseline, indicating the anatomical structure of the sample. Middle and bottom: spatial maps of the maximum and mean normalized error for the reconstructed baseline using a 6s sampling interval. In this dataset there was uncorrected sample motion that led to high maximum and average errors in certain parts of the explanted CNS (arrows).

Computation time of baselined normalization using baseline compression

The entire purpose of baseline compression is to accelerate the calculation of the fluorescence baseline without requiring extensive data duplication. To demonstrate that the compressed baseline does offer a speed benefit, we created a fake dataset with the same dimensions of a typical light sheet microscopy dataset (1000 timepoints, 22 “z planes”, 2048 “x pixels” and 2048 “y pixels”) to use for benchmarking the performance of the compressed baseline technique. We created a fake dataset instead of using real data because the fake data can be generated at runtime and thus my profiling results will not include the time required to load raw images from disk. As demonstrated in the schematic workflow of the full baseline calculation in Figure 4.2, the amount of data sent between workers during the data repartitioning step is dependent on the size of each image, and thus the time required for baseline normalization should scale supra-linearly with image size. But with the downsampled baseline approach, since there is no communication between workers, the time for baseline normalization should be at most linearly dependent of the size of the image (because of time required for reading

baseline data from hard drives). To test this prediction, we sliced the fake dataset into increasingly sized chunks and tested the time required to perform baseline normalization on these chunks of data. As predicted, using the compressed baseline, the time required to generate a single baseline normalized image was sub-linear with "image" size, while the time required with the full baseline (which requires repartitioning the data) grew supra-linearly with "image" size (Figure 4.8). This shows the promise of the baseline compression approach: at the price of controllable, predictable error, a fundamental preprocessing step can be accelerated by over two orders of magnitude (1000s for the full baseline vs. 7s for the downsampled baseline at maximum image size).

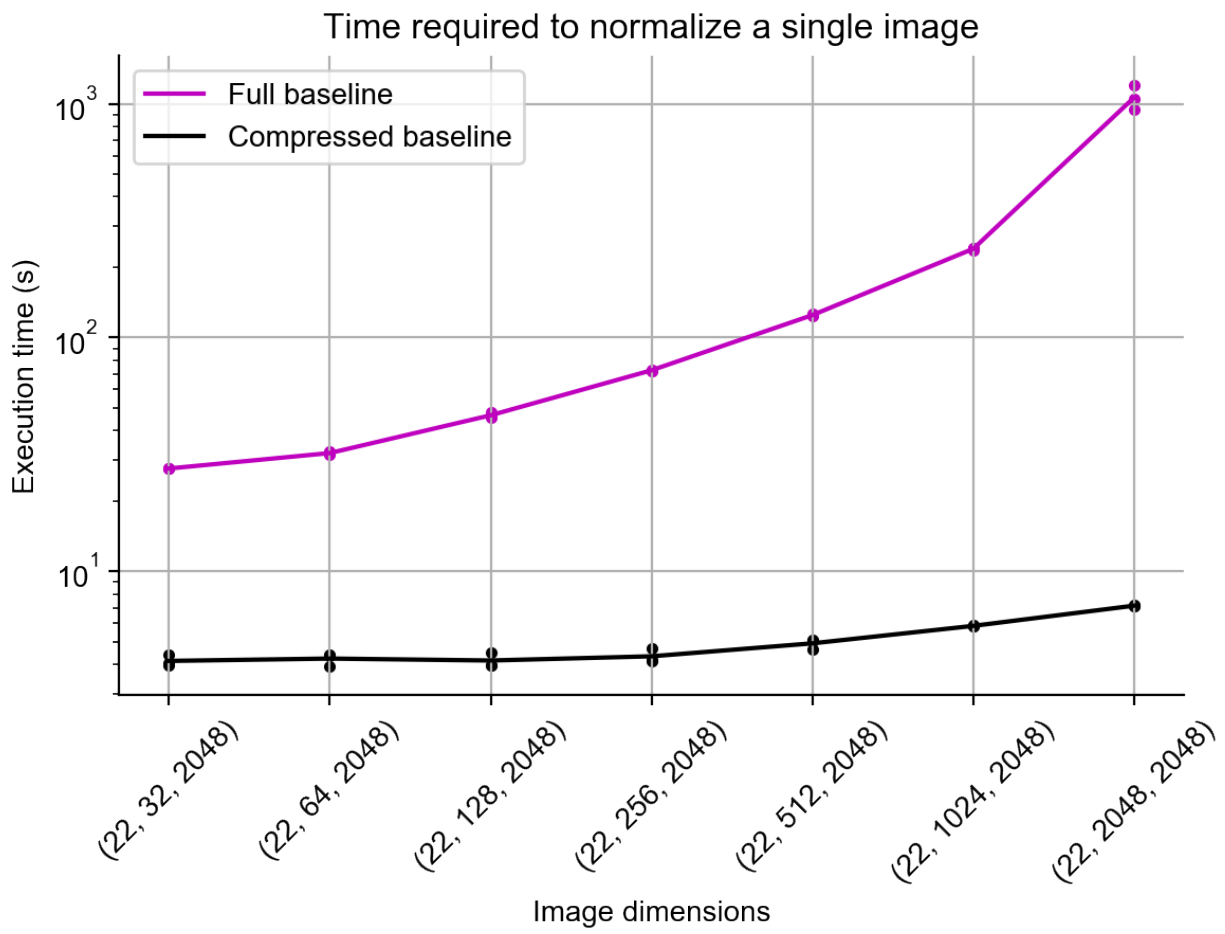

Figure 4.8. Comparing the execution time of baseline normalization using a full baseline vs. baseline normalization using a compressed baseline.
The "images" for this experiment came from a random array with shape (1000, 22, 2048, 2048) that was distributed along the first axis. An array with this size and arrangement emulates a typical light sheet microscopy dataset. This experiment used a previously computed compressed baseline with a 1:80 compression ratio. The dataset was then sliced into sub-arrays of increasing size, and the time required to perform baseline normalization on each sub-array was recorded. Three trials were performed for each image size. Computation was performed on 40 cores on the Janelia Compute Cluster, although this was mainly to accelerate the full baseline calculation, as generating a single baseline-normalized image using the compressed baseline is so fast that we did not invest in making it parallelizable.

Discussion

We have demonstrated a technique for rapid, scalable baseline normalization for large

functional imaging datasets. We leveraged the assumption that the fluorescence

baseline varies slowly to enable a significantly accelerated baseline normalization workflow, at the cost of some controllable error in the final result. There is nothing technically sophisticated about this technique—we simply use linear interpolation for pointwise, lossy, reconstruction of the downsampled fluorescence baseline. That such a naive approach can already promising results suggests that there is ample opportunity for more sophisticated techniques, e.g. methods that could produce lower reconstruction error with the same or better compression. An immediate improvement over the implementation I have described here would be downsampling the baseline with uneven intervals to allow denser sampling of epochs where the baseline is changing rapidly. Thinking further,cubic spline interpolation instead of linear interpolation for reconstruction would ensure that the reconstructed baseline is differentiable and likely reduce reconstruction error, at the expense of greater computational complexity in reconstruction and a larger file size for the compressed baseline. Temporal downsampling as a compression technique is quite crude compared to standard time series compression methods. Higher compression ratios with lower reconstruction errors are likely attainable by using frequency-domain techniques like Fourier-domain or wavelet-based compression schemes (Ahmed et al. 1974; Hilton 1997), although performant random access to individual baseline image would likely require a much more complicated data structure than the one we designed for temporal downsampling compression.

Error is inevitable in any approximation, and the technique presented here is no exception. In this particular case, the downsampled baseline technique allows a data

analyst to trade off error for speed. Although the error rate attained via the downsampled baseline was quite low across all three datasets, even a 1% error may be too high for some analyses. I do not claim that the lossy compression scheme presented here is a complete substitute for a baseline estimate that uses all available temporal information. What the downsampled baseline technique offers, however, is an accelerated path through the intermediate phase of a research project, between raw data and a final result. The compressed baseline technique enables a researcher to rapidly home in on cells or regions of interest in a dataset, and then potentially study those areas with the increased accuracy of the full baseline, which can be easily calculated for small chunks of data. Functional imaging with a light sheet microscope can comprehensively record activity from large populations of excitable cells over a long period of time. Light sheet microscopy became possible through extensive development of data acquisition hardware; similar efforts, such as those presented in this chapter, are needed in the area of analysis before light sheet microscopy can reach its full promise.

Materials and Methods

Data acquisition

Light sheet data of larval zebrafish were collected on a custom-built light sheet microscope (Vladimirov et al. 2014). Imaging data of *Drosophila melanogaster* larval nervous system explant were collected on a separate custom-built light sheet microscope and preprocessed as described in Lemon et al. 2015. Distributed computing was performed using the high performance compute cluster at Janelia Research

Campus via the Dask distributed computing framework (Rocklin 2018). Raw images were filtered and motion-corrected as described in Chapter 2.

Chapter 5: Concluding remarks

The goal of this thesis was to investigate the structural and functional properties of astroglial cells in larval zebrafish, and to contribute a strategy for accelerating this investigation. The first part of Chapter 2 used structural fluorescence imaging to detail the anatomy of zebrafish astroglia, individually and in bulk, across the larval zebrafish brain; the latter part of Chapter 2 used functional imaging to describe multiple scales of calcium activity in larval zebrafish astroglia. In Chapter 3, we combined functional imaging in behaving larval zebrafish with a range of cellular perturbations to elucidate a link between astroglial calcium activity and a behavioral state switch. In Chapter 4, I describe a strategy for accelerating a crucial preprocessing step for functional imaging datasets. In the following sections, I will review and contextualize the results from each of these chapters and highlight directions for future work.

Chapter 2

The earliest studies of the cellular structure of the nervous system were undertaken through the optical methods of histopathology (Virchow 1846). The neuroanatomists who performed these studies observed both neurons and glia in the nervous systems of many different organisms, and with this expansive perspective they postulated theories of brain function that attributed fundamental dynamical roles to both types of cells (Somjen 1988). However, as cellular neuroscience became mechanistic with the advent of electrophysiology, the originally pluralistic view of the nervous system was replaced by a neuron-centric (and increasingly mammal-centric) perspective. Neurons fire spikes, and glia do not; this gave electrophysiologists little reason to insert electrodes into glia.

Although neuroscientists knew that glia were important for the nervous system, the role of glia was described in passive terms, e.g. “supporting” neurons, since, by virtue of their electrical silence, glial cells were viewed as “passive”. This view remained unchallenged until the advent of calcium imaging, which revealed that many mammalian glial cells have calcium-mediated excitability, and that these excitable glia can respond rapidly to changes in the extracellular space, including changes induced by neuronal activity. The function of calcium excitability in glial cells is still the subject of debate (Bazargani and Attwell 2016), but the notion that glial cells are “passive” is no longer dogma in systems neuroscience. These studies of excitable glia have almost exclusively examined astroglia (astrocytes, Müller glia, and Bergmann glia) in adult rodents (with a few exceptions: see (Ma et al. 2016; Sild et al. 2016)), which means that there is an opportunity to generalize our understanding of excitable glia by examining these cells in other organisms.

With this broader goal in mind, I sought to describe in Chapter 2 the basic properties of astroglial cells in larval zebrafish. To this end, we created several transgenic zebrafish using the GFAP promoter to drive expression fluorescent proteins in astroglial cells. We then used structural and functional fluorescence imaging to describe astroglial cells in larval zebrafish. We found that these cells are highly polarized, yet they also densely ramify in neuropil and around cell bodies in the ventral and lateral aspects of the brain. In mammals, astroglia are known to tightly surround neuronal cell bodies and synapses, which gives astroglia the potential to respond to activity-related changes in the extracellular space (Iino et al. 2001). We characterized larval zebrafish astroglia with

light microscopy, which has insufficient spatial resolution to reveal how the fine processes of these cells relate to neurons and synapses. Electron microscopy is currently the only technique with the nanometer-scale resolution required to observe such structures, so this technique would be a natural choice for following up our anatomical observations at the high resolution needed to compare fine astroglial processes in fish with those in mammals.

Our functional imaging revealed a level of complexity we were not prepared for. With our lab's background in calcium imaging of neurons, we approached astroglial calcium activity with the invalid assumption that we would observe familiar phenomena. We were wrong: while neuronal calcium activity in a single cell is relatively fast and spatially coherent, astroglial calcium activity is relatively slow and could often be seen propagating within single cells. We also observed that calcium activity could spread between adjacent astroglia. We could only provide examples of these phenomena, as we lacked the proper analysis tools for quantifying these events. But such quantification should be done, in large part because the astroglial calcium activity we observed is quite puzzling: We observed calcium events within single cells that were restricted to a single compartment in the cell, but also calcium events that would spread across compartments within a cell. Some of these events, in turn, could apparently recruit calcium responses in adjacent cells. The spatial propagation we observed strongly suggests these calcium events are regenerative, but these events must also be gated somehow, because some calcium events fail to spread within a cell, or across cells.

Beyond the new techniques needed for analyzing functional imaging data, the study of

the molecular logic of these calcium events will likely require careful genetic and pharmacological dissection of the relevant signaling pathways.

We also could not address in this study the function of the calcium events we observed. Since the larval zebrafish brain is neurogenic, it is possible that there is some link between the spontaneous calcium activity we observed in astroglia and the proliferation of newborn neurons, as has been observed in radial glia in the developing mouse brain (Weissman et al. 2004; Rash et al. 2016). Finding evidence for such a link in the larval zebrafish would be straightforward with long-term structural and functional imaging during development.

Undertaking such long-term imaging experiments from a neurodevelopmental perspective would also add clarity to another issue we noticed: the large quantity of GFAP+ cells in our transgenic animals that, based on morphological and anatomical considerations, we did not believe to be astroglia. Instead, we suspected that these cells are recently born neurons that inherited a fluorophore-laden cytosol from their mother cell. It would be simple to test this hypothesis by performing time-lapse volumetric fluorescence imaging of transgenic animals and tracking individual cells; We would predict that this dataset would reveal asymmetric cell divisions of astroglia that would produce a mother cell and a migrating daughter cell with slowly decaying fluorescence. Documenting the spatial distribution of these anomalous GFAP+ cells and the temporal stability of their retention of the exogenous protein will be very important for the interpretation of any future studies that may seek to apply population-wide perturbation to astroglia.

Chapter 3

The use of sensory feedback to stabilize motor behavior is well documented (Lackner and Dizio 2017; Shadmehr and Mussa-Ivaldi 2018). In this model, an agent engaging in a targeted action is thwarted by perturbations that cause the action to miss its target. By observing the outcome of the action and comparing this result to an internal model, the agent can generate an updated action that compensates for the perturbation and thereby reduces the mismatch between the action's outcome and the intended outcome. But this strategy only works when the feedback signal can be used to update actions in a manner that reduces the mismatch. Animals moving through adverse environments do not always have control over their actions, and can end up stuck. What strategy might a stuck animal employ? In the first part of Chapter 3 we presented a virtual reality (VR) behavioral paradigm for larval zebrafish that allows us to approach an answer to this question. By varying the gain parameter of our VR while fish engaged in the optomotor response, we found that fish responded to inexorable optic flow by alternating between active and passive behavioral states, which we interpret as a strategic response. Our behavioral paradigm is simple and experimentally tractable, but that simplicity comes at a cost: rather than observing naturalistic behavior, we observed "fictive behavior", i.e. behavior *attempts* inferred from electrophysiological recordings. Although fictive behavior is a standard technique for studies of motor circuits in the spinal cord and hindbrain of larval zebrafish, these studies typically examine the contribution of specific neurons to a specific motor pattern. Whereas, in the case of the work we present in Chapter 3, we are describing behavior at a more abstract level –

active vs passive states– and it is unclear how our conceptualization of fictive behavior maps to the space of naturalistic fish behavior. For example, in Chapter 3 we quantify fictive fish behavior in terms of bout power and frequency, but actual fish behavior lies in a space much richer than what can be described by these two parameters. Thus, it would be very illuminating to validate and extend our behavioral model with a paradigm that evokes naturalistic behavior. This would this allow us to define “active” and “passive” states in richer terms, and potentially set the stage for examining this behavioral phenomenon in older zebrafish and other model organisms.

The second part of Chapter 3 concerns the cellular basis of the transition from active to passive behavioral states. We use volumetric imaging to search the fish brain for neurons and astroglia with significant calcium responses at the transition between active and passive states. Unfortunately, the design of our behavioral experiments did not allow us to perform data analysis in the most intuitive way. Ideally, we would have designed the behavioral assay such that our analysis would be as simple as possible. Our goal was to identify cells that satisfied two conditions: these cells should be active when the animal stopped swimming due to lack of visual feedback, and less active or inactive when the animal stopped swimming due to external factors (e.g., the abatement of the visual stimulus). Such cells would be detected by a very simple analysis: the difference between mean activity triggered on internally-driven passivity and mean activity triggered on externally-driven passivity, assuming that the animal’s behavior was similar in both cases. This approach, which is called a “contrast”, is standard in functional magnetic resonance imaging (fMRI) data analysis, but we could not apply it in

our data because we did not have the required trial structure (attempts were made to design a trial-structured experiment, but the throughput was deemed too low to be useful). Instead, we adopted an analysis approach based on multiple rounds of clustering and matrix factorization. These analyses succeeded in detecting astroglial projections to the L-MO, but they failed to detect the noradrenergic neurons that excite the L-MO astroglia. It is possible that a simpler regression-based analysis could have revealed a more complete picture of the cellular basis of the behavior earlier in our project. Generally, the analysis of volumetric imaging data in larval zebrafish would benefit heavily by borrowing techniques from the fMRI community, which has been grappling for decades with the same problems we are newly facing.

After we concluded that astroglial calcium activity in the L-MO was highly correlated with the transition from active to passive behavioral states, we used a series of perturbation experiments which added weight to our belief that astroglial calcium activity in the L-MO was necessary and sufficient for the onset of passivity. For exciting astroglia, we were fortunate in that we could use tools that had been developed for exciting neurons; but we had no reason to believe that tools for inhibiting neurons would work on astroglia, since neuronal inhibition is typically accomplished by hyperpolarization of the membrane potential, and astroglial excitability is not a simple function of the membrane potential. So, for inhibiting astroglial activity we used ablations and pharmacology. Compared to optogenetic excitation, neither of these perturbations is subtle, cell-type specific or temporally precise. In light of these limitations, the ideal tool for suppressing astroglial calcium activity would be a genetically encoded (for cell-type specificity), light-

activated (for spatiotemporal precision) blockade of either the extracellular mechanisms that induce astroglial excitability, or the intracellular mechanisms that sustain it. The former strategy might be difficult if multiple ligands can drive astroglial calcium responses, but for the latter strategy, an optogenetic calcium pump might be sufficient, provided a pump can overcome the intense concentration gradient that favors calcium influx into astroglial cytosol. Such tools would address a major need in mechanistic studies of astroglia.

Our study did not reveal the mechanism by which astroglial calcium activity in the L-MO induces a change in neuronal activity that ultimately drives behavioral passivity. With the confusion and controversy surrounding the debate on glia-neuron interactions (Fiacco and McCarthy 2018; Savtchouk and Volterra 2018), it may not be clear which potential mechanisms to investigate. However, there is relatively compelling evidence that glia can release ATP that inhibits neurons via purinergic receptors (Gourine et al. 2010; Irwin et al. 2013; Ma et al. 2016). We have preliminary data (not shown here) which indicates that a population of GABAergic neurons in the L-MO may be *excited* as a consequence of astroglial excitation. Perhaps L-MO astroglia release ATP that inhibits inhibitory inputs to these GABAergic cells, thereby acting as excitation. This is an active area of investigation.

Overall, I hope that the experiments and analyses we presented in Chapter 3 will receive the attention of researchers in a position to follow up on our claims, as there are many other exciting directions which we could not pursue. The ease of functional

imaging in larval zebrafish will hopefully ensure that our study can inspire further research on astroglia in this model system.

Chapter 4

In Chapter 4 I described a simple approach for vastly accelerating baseline normalization of large functional imaging datasets, such as those generated by light sheet microscopes. Existing approaches for baseline normalization demand extensive data duplication and lengthy, expensive computation. The approach I described trades off accuracy for speed, but in percentage terms the speed gains are vastly larger than the loss in accuracy, so I think this approach will be very attractive for early discovery-driven phases of data analysis, where a little error is tolerable. It should be noted that the concept of "error" that we use is somewhat contrived—we treat the result of a particular filter (a windowed percentile filter) as ground truth, when in fact that filter is merely an attempt to estimate a biological quantity. It would be interesting to explore ways of estimating the biological quantity directly. Besides enabling a better definition of "error" for the purposes of Chapter 4, knowing the true fluorescence baseline would allow the development of more accurate filters. Indeed, based on my work in Chapter 4, it seems highly unlikely to me that the windowed percentile filter is optimal: for the fruit fly explant data shown in Figure 4.7, We had to carefully hand-tune the parameters of the percentile filter to prevent the strong, rhythmic calcium activity from corrupting the baseline estimate. Gathering more data is the remedy for this kind of problem. One approach would be to image calcium indicators at their design wavelength as well as imaging at a wavelength that matches the isosbestic point of the indicator. At the

isosbestic point, the emission of the calcium indicator is independent of the calcium concentration, and thus imaging at this wavelength allows direct detection of the fluorescence baseline. This property of calcium indicators is used for baseline normalization in fiber photometry (Gunaydin et al. 2014), and it would be relatively simple to adapt this technique for light sheet microscopy. Speaking only for myself, after years working with functional imaging data, I had never carefully examined the fluorescence baseline of my datasets, largely because the computation was so expensive. I suspect many other researchers in this area are equally blind to a basic feature of their data.

After accelerating baseline normalization, there are other areas in the preprocessing workflow to optimize and accelerate. Motion correction requires applying a transformation to each image, computationally speaking, this entails interpolation in three dimensions. On a CPU this can be relatively slow, e.g. several seconds per image, but the same operation should be accelerated by several orders of magnitude running the computation on a graphics processing unit (GPU). GPU computing would also accelerate the process of estimating the transform for each image, although this computation only needs to run once per dataset. If baseline normalization and motion correction can be made fast enough, then it may be possible to preprocess data in real time, as it is acquired by the microscope. This would be the dream of any experimenter, but it is up to software developers and data engineers to make this dream a reality.

References

Abdelfattah AS, **Kawashima T**, **Singh A**, **Novak O**, **Mensh BD**, **Paninski L**, **Macklin JJ**, **Podgorski K**, **Ahrens MB**, **Lavis LD**, **Schreiter ER**. Bright and photostable chemigenetic indicators for extended in vivo voltage imaging. *bioRxiv* (2018). doi: 10.1101/436840.

Adolf B, **Chapouton P**, **Lam CS**, **Topp S**, **Tannhäuser B**, **Strähle U**, **Götz M**, **Bally-Cuif L**. Conserved and acquired features of adult neurogenesis in the zebrafish telencephalon. *Dev Biol* 295: 278–293, 2006.

Agulhon C, **Fiacco TA**, **McCarthy KD**. Hippocampal short- and long-term plasticity are not modulated by astrocyte Ca2+ signaling. *Science (80-)* 327: 1250–1254, 2010.

Ahmed N, **Natarajan T**, **Rao KR**. Discrete Cosine Transform. *IEEE Trans Comput* C–23: 90–93, 1974.

Ahmed Z, **Lewis CA**, **Faber DS**. Glutamate stimulates release of Ca2+ from internal stores in astroglia. *Brain Res* 516: 165–169, 1990.

Ahrens MB, **Li JM**, **Orger MB**, **Robson DN**, **Schier AF**, **Engert F**, **Portugues R**. Brain-wide neuronal dynamics during motor adaptation in zebrafish. *Nature* 485: 471–477, 2012.

Ahrens MB, **Orger MB**, **Robson DN**, **Li JM**, **Keller PJ**. Whole-brain functional imaging at cellular resolution using light-sheet microscopy. *Nat Methods* 10: 413–420, 2013.

Airan RD, **Thompson KR**, **Fenno LE**, **Bernstein H**, **Deisseroth K**. Temporally precise in vivo control of intracellular signalling. *Nature* 458: 1025–1029, 2009.

Alvarez-Buylla A, **Nottebohm F**. Migration of young neurons in adult avian brain. *Nature* 335: 353–354, 1988.

Araque A, **Martín ED**, **Perea G**, **Arellano JI**, **Buño W**. Synaptically released acetylcholine evokes Ca2+ elevations in astrocytes in hippocampal slices. *J. Neurosci.* (2002). doi: 20026212.

Araque A, **Parpura V**, **Sanzgiri RP**, **Haydon PG**. Glutamate-dependent astrocyte modulation of synaptic transmission between cultured hippocampal neurons. *Eur J Neurosci* 10: 2129–2142, 1998.

Aston-Jones G, **Cohen JD**. AN INTEGRATIVE THEORY OF LOCUS COERULEUS-NOREPINEPHRINE FUNCTION: Adaptive Gain and Optimal Performance. *Annu Rev Neurosci* 28: 403–450, 2005.

Avants BB, **Yushkevich P**, **Pluta J**, **Minkoff D**, **Korczykowski M**, **Detre J**, **Gee JC**. The optimal template effect in hippocampus studies of diseased populations. *Neuroimage* 49: 2457–2466, 2010.

Baier H, **Orger MB**, **Smear MC**, **Anstis SM**. Perception of Fourier and non-Fourier motion by larval zebrafish. *Nat Neurosci* 3: 1128–1133, 2000.

Bazargani N, **Attwell D**. Astrocyte calcium signaling: The third wave. *Nat Neurosci* 19: 182–189, 2016.

Bekar LK, **He W**, **Nedergaard M**. Locus coeruleus α-adrenergic-mediated activation of cortical astrocytes in vivo. *Cereb. Cortex* (2008). doi: 10.1093/cercor/bhn040.

Benediktsson AM, **Schachtele SJ**, **Green SH**, **Dailey ME**. Ballistic labeling and dynamic imaging of astrocytes in organotypic hippocampal slice cultures. *J Neurosci Methods* 141: 41–53, 2005.

Bentivoglio M, **Mazzarello P**. The history of radial glia. *Brain Res Bull* 49: 305–315, 1999.

Berry MW, **Browne M**, **Langville AN**, **Pauca VP**, **Plemmons RJ**. Algorithms and applications for approximate nonnegative matrix factorization. *Comput Stat Data Anal* 52: 155–173, 2007.

Bezzi P, **Gundersen V**, **Galbete JL**, **Seifert G**, **Steinhäuser C**, **Pilati E**, **Volterra A**. Astrocytes contain a vesicular compartment that is competent for regulated exocytosis of glutamate. *Nat Neurosci* 7: 613–620, 2004.

Bianco IH, **Kampff AR**, **Engert F**. Prey Capture Behavior Evoked by Simple Visual Stimuli in Larval Zebrafish. *Front Syst Neurosci* 5, 2011.

Borla MA, **Palecek B**, **Budick S**, **O'Malley DM**. Prey capture by larval zebrafish: Evidence for fine axial motor control. *Brain Behav Evol* 60: 207–229, 2002.

Bouret S, **Sara SJ**. Reward expectation, orientation of attention and locus coeruleus-medial frontal cortex interplay during learning. *Eur J Neurosci* 20: 791–802, 2004.

Boutsidis C, **Gallopoulos E**. SVD based initialization: A head start for nonnegative matrix factorization. *Pattern Recognit* 41: 1350–1362, 2008.

Cembrowski MS, **Wang L**, **Sugino K**, **Shields BC**, **Spruston N**. Hipposeq: A comprehensive RNA-seq database of gene expression in hippocampal principal neurons. *Elife* 5, 2016.

Chapouton P, **Skupien P**, **Hesl B**, **Coolen M**, **Moore JC**, **Madelaine R**, **Kremmer E**, **Faus-Kessler T**, **Blader P**, **Lawson ND**, **Bally-Cuif L**. Notch Activity Levels Control the Balance between Quiescence and Recruitment of Adult Neural Stem Cells. *J Neurosci* 30: 7961–7974, 2010.

Chen S, **Chiu CN**, **McArthur KL**, **Fetcho JR**, **Prober DA**. TRP channel mediated neuronal activation and ablation in freely behaving zebrafish. *Nat Methods* 13: 147–150, 2016a.

Chen TW, **Wardill TJ**, **Sun Y**, **Pulver SR**, **Renninger SL**, **Baohan A**, **Schreiter ER**, **Kerr RA**, **Orger MB**, **Jayaraman V**, **Looger LL**, **Svoboda K**, **Kim DS**. Ultrasensitive fluorescent proteins for imaging neuronal activity. *Nature* 499: 295–300, 2013.

Chen X, **Gays D**, **Santoro MM**. Transgenic zebrafish. *Methods Mol Biol* 1464: 107–114, 2016b.

Cho W-H, **Barcelon E**, **Lee SJ**. Optogenetic Glia Manipulation: Possibilities and Future Prospects. *Exp Neurobiol* 25: 197, 2016.

Corish P, **Tyler-Smith C**. Attenuation of green fluorescent protein half-life in mammalian cells. *Protein Eng Des Sel* 12: 1035–1040, 1999.

Cornell-Bell AH, **Finkbeiner SM**, **Cooper MS**, **Smith SJ**. Glutamate induces calcium waves in cultured astrocytes: Long-range glial signaling. *Science (80-)* 247: 470–473, 1990.

Costa MR, **Götz M**, **Berninger B**. What determines neurogenic competence in glia? *Brain Res. Rev.* 63: 47–59, 2010.

Cui Y, **Yang Y**, **Ni Z**, **Dong Y**, **Cai G**, **Foncelle A**, **Ma S**, **Sang K**, **Tang S**, **Li Y**, **Shen Y**, **Berry H**, **Wu S**, **Hu H**. Astroglial Kir4.1 in the lateral habenula drives neuronal bursts in depression. *Nature* 554: 323–327, 2018.

Dana H, **Mohar B**, **Sun Y**, **Narayan S**, **Gordus A**, **Hasseman JP**, **Tsegaye G**, **Holt GT**, **Hu A**, **Walpita D**, **Patel R**, **Macklin JJ**, **Bargmann CI**, **Ahrens MB**, **Schreiter ER**, **Jayaraman V**, **Looger LL**, **Svoboda K**, **Kim DS**. Sensitive red protein calcium indicators for imaging neural activity. *Elife* 5, 2016.

Deemyad T, **Lüthi J**, **Spruston N**. Astrocytes integrate and drive action potential firing in inhibitory subnetworks. *Nat Commun* 9, 2018.

Denk W, **Strickler JH**, **Webb WW**. Two-photon laser scanning fluorescence microscopy. *Science (80-)* 248: 73–76, 1990.

Dombeck DA, **Reiser MB**. Real neuroscience in virtual worlds. *Curr. Opin. Neurobiol.* 22: 3–10, 2012.

Dunn TW, **Mu Y**, **Narayan S**, **Randlett O**, **Naumann EA**, **Yang CT**, **Schier AF**, **Freeman J**, **Engert F**, **Ahrens MB**. Brain-wide mapping of neural activity controlling zebrafish exploratory locomotion. *Elife* 5, 2016.

Easter SS, **Nicola GN**. The development of vision in the zebrafish (Danio rerio). *Dev Biol* 180: 646–663, 1996.

Faber DS, **Fetch JR**, **Korn H**. Neuronal Networks Underlying the Escape Response in Goldfish: General Implications for Motor Control. *Ann N Y Acad Sci* 563: 11–33, 1989.

Farrar MJ, **Kolkman KE**, **Fetcho JR**. Features of the structure, development, and activity of the zebrafish noradrenergic system explored in new CRISPR transgenic lines. *J Comp Neurol* 526: 2493–2508, 2018.

Felzenszwalb PF, **Huttenlocher DP**. Efficient graph-based image segmentation. *Int J Comput Vis* 59: 167–181, 2004.

Fiacco TA, **McCarthy KD**. Multiple Lines of Evidence Indicate That Gliotransmission Does Not Occur under Physiological Conditions. *J Neurosci* 38: 3–13, 2018.

Figueiredo M, **Lane S**, **Stout RF**, **Liu B**, **Parpura V**, **Teschemacher AG**, **Kasparov S**. Comparative analysis of optogenetic actuators in cultured astrocytes. *Cell Calcium* 56: 208–214, 2014.

Fosque BF, **Sun Y**, **Dana H**, **Yang CT**, **Ohyama T**, **Tadross MR**, **Patel R**, **Zlatic M**, **Kim DS**, **Ahrens MB**, **Jayaraman V**, **Looger LL**, **Schreiter ER**. Labeling of active neural circuits in vivo with designed calcium integrators. *Science (80-)* 347: 755–760, 2015.

Freeman MR. Drosophila central nervous system glia. *Cold Spring Harb Perspect Biol* 7, 2015.

Freifeld L, **Odstrcil I**, **Förster D**, **Ramirez A**, **Gagnon JA**, **Randlett O**, **Costa EK**, **Asano S**, **Celiker OT**, **Gao R**, **Martin-Alarcon DA**, **Reginato P**, **Dick C**, **Chen L**, **Schoppik D**, **Engert F**, **Baier H**, **Boyden ES**. Expansion microscopy of zebrafish for neuroscience and developmental biology studies. *Proc Natl Acad Sci* 114: E10799–E10808, 2017.

Gafni J, **Munsch JA**, **Lam TH**, **Catlin MC**, **Costa LG**, **Molinski TF**, **Pessah IN**. Xestospongins: Potent membrane permeable blockers of the inositol 1,4,5-trisphosphate receptor. *Neuron* 19: 723–733, 1997.

Gourine A V., **Kasymov V**, **Marina N**, **Tang F**, **Figueiredo MF**, **Lane S**, **Teschemacher AG**, **Spyer KM**, **Deisseroth K**, **Kasparov S**. Astrocytes control breathing through pH-dependent release of ATP. *Science (80-)* 329: 571–575, 2010.

Green MH, **Ho RK**, **Hale ME**. Movement and function of the pectoral fins of the larval zebrafish (Danio rerio) during slow swimming. *J Exp Biol* 214: 3111–3123, 2011.

Gross-Thebing T, **Paksa A**, **Raz E**. Simultaneous high-resolution detection of multiple transcripts combined with localization of proteins in whole-mount embryos. *BMC Biol* 12, 2014.

Gunaydin LA, **Grosenick L**, **Finkelstein JC**, **Kauvar I V.**, **Fenno LE**, **Adhikari A**, **Lammel S**, **Mirzabekov JJ**, **Airan RD**, **Zalocusky KA**, **Tye KM**, **Anikeeva P**, **Malenka RC**, **Deisseroth K**. Natural neural projection dynamics underlying social behavior. *Cell* 157: 1535–1551, 2014.

Hempel CM, **Sugino K**, **Nelson SB**. A manual method for the purification of fluorescently labeled neurons from the mammalian brain. *Nat Protoc* 2: 2924–2929, 2007.

Hertz L, **Zielke HR**. Astrocytic control of glutamatergic activity: Astrocytes as stars of the show. *Trends Neurosci.* 27: 735–743, 2004.

Higashijima S, **Masino MA**, **Mandel G**, **Fetcho JR**. Imaging Neuronal Activity During Zebrafish Behavior With a Genetically Encoded Calcium Indicator. *J Neurophysiol* 90: 3986–3997, 2006.

Hildebrand DGC, **Cicconet M**, **Torres RM**, **Choi W**, **Quan TM**, **Moon J**, **Wetzel AW**, **Scott Champion A**, **Graham BJ**, **Randlett O**, **Plummer GS**, **Portugues R**, **Bianco IH**, **Saalfeld S**, **Baden AD**, **Lillaney K**, **Burns R**, **Vogelstein JT**, **Schier AF**, **Lee WCA**, **Jeong WK**, **Lichtman JW**, **Engert F**. Whole-brain serial-section electron microscopy in larval zebrafish. *Nature* 545: 345–349, 2017.

Hilton ML. Wavelet and wavelet packet compression of electrocardiograms. *IEEE Trans Biomed Eng* 44: 394–402, 1997.

Holscher C. Rats are able to navigate in virtual environments. *J Exp Biol* 208: 561–569, 2005.

Hoyer PO. Non-negative matrix factorization with sparseness constraints [Online]. *J Mach Learn Res* 5: 1457–1469, 2004. http://arxiv.org/abs/cs/0408058.

Huxley AF, **Stämpfli R**. Effect of potassium and sodium on resting and action potentials of single myelinated nerve fibres. *J Physiol* 112: 496–508, 1951.

Iino M, **Goto K**, **Kakegawa W**, **Okado H**, **Sudo M**, **Ishiuchi S**, **Miwa A**, **Takayasu Y**, **Saito I**, **Tsuzuki K**, **Ozawa S**. Glia-synapse interaction through Ca 2+ -permeable AMPA receptors in Bergmann glia. *Science (80-)* 292: 926–929, 2001.

Irwin MH, **Parameshwaran K**, **Pinkert CA**. Mouse models of mitochondrial comple... [Int J Biochem Cell Biol. 2013] - PubMed - NCBI. *Int J Biochem {&} cell Biol* 45: 34–40, 2013.

Johnson EC. A novel diuretic hormone receptor in Drosophila: evidence for conservation of CGRP signaling. *J Exp Biol* 208: 1239–1246, 2005.

Johnson K, **Barragan J**, **Bashiruddin S**, **Smith CJ**, **Tyrrell C**, **Parsons MJ**, **Doris R**, **Kucenas S**, **Downes GB**, **Velez CM**, **Schneider C**, **Sakai C**, **Pathak N**, **Anderson K**, **Stein R**, **Devoto SH**, **Mumm JS**, **Barresi MJF**. Gfap-positive radial glial cells are an essential progenitor population for later-born neurons and glia in the zebrafish spinal cord. *Glia* 64: 1170–1189, 2016.

Kang J, **Jiang L**, **Goldman SA**, **Nedergaard M**. Astrocyte-mediated potentiation of inhibitory synaptic transmission. *Nat. Neurosci.* (1998). doi: 10.1038/3684.

Kasthuri N, **Hayworth KJ**, **Berger DR**, **Schalek RL**, **Conchello JA**, **Knowles-Barley S**, **Lee D**, **Vázquez-Reina A**, **Kaynig V**, **Jones TR**, **Roberts M**, **Morgan JL**, **Tapia JC**, **Seung HS**, **Roncal WG**, **Vogelstein JT**, **Burns R**, **Sussman DL**, **Priebe CE**, **Pfister H**, **Lichtman JW**. Saturated Reconstruction of a Volume of Neocortex. *Cell* 162: 648–661, 2015.

Keller GB, **Bonhoeffer T**, **Hübener M**. Sensorimotor Mismatch Signals in Primary Visual Cortex of the Behaving Mouse. *Neuron* 74: 809–815, 2012.

Keller PJ, **Schmidt AD**, **Wittbrodt J**, **Stelzer EHK**. Reconstruction of zebrafish early embryonic development by scanned light sheet microscopy. *Science (80-)* 322: 1065–1069, 2008.

Kimura Y, **Hisano Y**, **Kawahara A**, **Higashijima SI**. Efficient generation of knock-in transgenic zebrafish carrying reporter/driver genes by CRISPR/Cas9-mediated genome engineering. *Sci Rep* 4: 6545, 2014.

Klapoetke NC, **Murata Y**, **Kim SS**, **Pulver SR**, **Birdsey-Benson A**, **Cho YK**, **Morimoto TK**, **Chuong AS**, **Carpenter EJ**, **Tian Z**, **Wang J**, **Xie Y**, **Yan Z**, **Zhang Y**, **Chow BY**, **Surek B**, **Melkonian M**, **Jayaraman V**, **Constantine-Paton M**, **Wong GKS**, **Boyden ES**. Independent optical excitation of distinct neural populations. *Nat Methods* 11: 338–346, 2014.

Kralj JM, **Douglass AD**, **Hochbaum DR**, **MacLaurin D**, **Cohen AE**. Optical recording of action potentials in mammalian neurons using a microbial rhodopsin. *Nat Methods* 9: 90–95, 2012.

Kriegstein A, **Alvarez-Buylla A**. The Glial Nature of Embryonic and Adult Neural Stem Cells. *Annu Rev Neurosci* 32: 149–184, 2009.

Krnjević K, **Morris ME**. Extracellular K + Activity and Slow Potential Changes in Spinal Cord and Medulla . *Can J Physiol Pharmacol* 50: 1214–1217, 2011.

Kroehne V, **Freudenreich D**, **Hans S**, **Kaslin J**, **Brand M**. Regeneration of the adult zebrafish brain from neurogenic radial glia-type progenitors. *Development* 138: 4831–4841, 2011.

Kunst M, **Laurell E**, **Mokayes N**, **Kramer A**, **Kubo F**, **Fernandes AM**, **Förster D**, **Dal Maschio M**, **Baier H**. A Cellular-Resolution Atlas of the Larval Zebrafish Brain. *Neuron* 103: 21-38.e5, 2019.

Lackner JR, **Dizio P**. Rapid adaptation to Coriolis force perturbations of arm trajectory. *J Neurophysiol* 72: 299–313, 2017.

Lemon WC, **Pulver SR**, **Höckendorf B**, **McDole K**, **Branson K**, **Freeman J**, **Keller PJ**. Whole-central nervous system functional imaging in larval Drosophila. *Nat Commun* 6, 2015.

Liao JC, **Fetcho JR**. Shared versus Specialized Glycinergic Spinal Interneurons in Axial Motor Circuits of Larval Zebrafish. *J Neurosci* 28: 12982–12992, 2008.

Liu KS, **Fetcho JR**. Laser ablations reveal functional relationships of segmental hindbrain neurons in zebrafish. *Neuron* 23: 325–335, 1999.

Liu TL, **Upadhyayula S**, **Milkie DE**, **Singh V**, **Wang K**, **Swinburne IA**, **Mosaliganti KR**, **Collins ZM**, **Hiscock TW**, **Shea J**, **Kohrman AQ**, **Medwig TN**, **Dambournet D**, **Forster R**, **Cunniff B**, **Ruan Y**, **Yashiro H**, **Scholpp S**, **Meyerowitz EM**, **Hockemeyer D**, **Drubin DG**, **Martin BL**, **Matus DQ**, **Koyama M**, **Megason SG**, **Kirchhausen T**, **Betzig E**. Observing the cell in its native state: Imaging subcellular dynamics in multicellular organisms. *Science (80-)* 360, 2018.

Lopez-Garcia C, **Molowny A**, **Garcia-Verdugo JM**, **Ferrer I**. Delayed postnatal neurogenesis in the cerebral cortex of lizards. *Dev. Brain Res.* (1988). doi: 10.1016/0165-3806(88)90096-X.

Lovett-Barron M, **Andalman AS**, **Allen WE**, **Vesuna S**, **Kauvar I**, **Burns VM**, **Deisseroth K**. Ancestral Circuits for the Coordinated Modulation of Brain State. *Cell* 171: 1411-1423.e17, 2017.

Ma Z, **Stork T**, **Bergles DE**, **Freeman MR**. Neuromodulators signal through astrocytes to alter neural circuit activity and behaviour. *Nature* 539: 428–432, 2016.

Maier SF. Learned helplessness and animal models of depression. *Prog Neuro-Psychopharmacology Biol Psychiatry* 8: 435–446, 1984.

Malatesta P, **Hartfuss E**, **Götz M**. Isolation of radial glial cells by fluorescent-activated cell sorting reveals a neuronal lineage. [Online]. *Development* 127: 5253–63, 2000. http://www.ncbi.nlm.nih.gov/pubmed/11076748.

Martín R, **Bajo-Grañeras R**, **Moratalla R**, **Perea G**, **Araque A**. Circuit-specific signaling in astrocyte-neuron networks in basal ganglia pathways. *Science (80-.).* (2015). doi: 10.1126/science.aaa7945.

Masino MA, **Fetcho JR**. Fictive Swimming Motor Patterns in Wild Type and Mutant Larval Zebrafish. *J Neurophysiol* 93: 3177–3188, 2005.

Morquette P, **Verdier D**, **Kadala A**, **Féthière J**, **Philippe AG**, **Robitaille R**, **Kolta A**. An astrocyte-dependent mechanism for neuronal rhythmogenesis. *Nat Neurosci* 18: 844–854, 2015.

Mu Y, **Bennett D V.**, **Rubinov M**, **Narayan S**, **Yang CT**, **Tanimoto M**, **Mensh BD**, **Looger LL**, **Ahrens MB**. Glia Accumulate Evidence that Actions Are Futile and Suppress Unsuccessful Behavior. *Cell* (2019). doi: 10.1016/j.cell.2019.05.050.

Nedergaard M. Direct signaling from astrocytes to neurons in cultures of mammalian brain cells. *Science (80-)* 263: 1768–1771, 1994.

Newman EA, **Zahs KR**. Calcium waves in retinal glial cells. *Science (80-.).* (1997). doi: 10.1126/science.275.5301.844.

O'Malley DM, **Kao YH**, **Fetcho JR**. Imaging the functional organization of zebrafish hindbrain segments during escape behaviors. *Neuron* 17: 1145–1155, 1996.

Orger MB, **Portugues R**. Correlating whole brain neural activity with behavior in head-fixed larval Zebrafish. In: *Methods in Molecular Biology*. 2016, p. 307–320.

Orkand RK, **Nicholls JG**, **Kuffler SW**. Effect of nerve impulses on the membrane potential of glial cells in the central nervous system of amphibia. *J. Neurophysiol.* (2017). doi: 10.1152/jn.1966.29.4.788.

Palla G, **Derényi I**, **Farkas I**, **Vicsek T**. Uncovering the overlapping community structure of complex networks in nature and society. *Nature* 435: 814–818, 2005.

Panier T, **Romano SA**, **Olive R**, **Pietri T**, **Sumbre G**, **Candelier R**, **Debrégeas G**. Fast functional imaging of multiple brain regions in intact zebrafish larvae using Selective Plane Illumination Microscopy. *Front Neural Circuits* 7, 2013.

Park HC, **Kim CH**, **Bae YK**, **Yeo SY**, **Kim SH**, **Hong SK**, **Shin J**, **Yoo KW**, **Hibi M**, **Hirano T**, **Miki N**, **Chitnis AB**, **Huh TL**. Analysis of upstream elements in the HuC promoter leads to the establishment of transgenic Zebrafish with fluorescent neurons. *Dev Biol* 227: 279–293, 2000.

Parpura V, **Basarsky TA**, **Liu F**, **Jeftinija K**, **Jeftinija S**, **Haydon PG**. Glutamate-mediated astrocyte-neuron signalling. *Nature* 369: 744–747, 1994.

Paton JA, **Nottebohm FN**. Neurons generated in the adult brain are recruited into functional circuits. *Science (80-.).* (1984). doi: 10.1126/science.6474166.

Paukert M, **Agarwal A**, **Cha J**, **Doze VA**, **Kang JU**, **Bergles DE**. Norepinephrine controls astroglial responsiveness to local circuit activity. *Neuron* 82: 1263–1270, 2014.

Petzold GC, **Murthy VN**. Role of astrocytes in neurovascular coupling. *Neuron* 71: 782–797, 2011.

Pinto L, **Koay SA**, **Engelhard B**, **Yoon AM**, **Deverett B**, **Thiberge SY**, **Witten IB**, **Tank DW**, **Brody CD**. An Accumulation-of-Evidence Task Using Visual Pulses for Mice Navigating in Virtual Reality. *Front Behav Neurosci* 12, 2018.

Porsolt RD, **Bertin A**, **Blavet N**, **Deniel M**, **Jalfre M**. Immobility induced by forced swimming in rats: Effects of agents which modify central catecholamine and serotonin activity. *Eur J Pharmacol* 57: 201–210, 1979.

Porter JT, **McCarthy KD**. Hippocampal Astrocytes In Situ Respond to Glutamate Released from Synaptic Terminals . *J. Neurosci.* (2018). doi: 10.1523/jneurosci.16-16-05073.1996.

Portugues R, **Engert F**. Adaptive Locomotor Behavior in Larval Zebrafish. *Front Syst Neurosci* 5, 2011.

Portugues R, **Severi KE**, **Wyart C**, **Ahrens MB**. Optogenetics in a transparent animal: Circuit function in the larval zebrafish. *Curr. Opin. Neurobiol.* 23: 119–126, 2013.

Poskanzer KE, **Yuste R**. Astrocytes regulate cortical state switching in vivo. *Proc Natl Acad Sci* 113: E2675–E2684, 2016.

Rakic P. Mode of cell migration to the superficial layers of fetal monkey neocortex. *J Comp Neurol* 145: 61–83, 1972.

Rakic P. Neuronal migration and contact guidance in the primate telencephalon. *Postgrad. Med. J.* 54: 25-40, 1972.

Rash BG, **Ackman JB**, **Rakic P**. Bidirectional radial Ca2+ activity regulates neurogenesis and migration during early cortical column formation. *Sci Adv* 2: 1–11, 2016.

Rock I, **Smith D**. The optomotor response and induced motion of the self. *Perception* 15: 497–502, 1986.

Rocklin M. Dask: Parallel Computation with Blocked algorithms and Task Scheduling. In: *Proceedings of the 14th Python in Science Conference*. 2018.

Sara SJ. The locus coeruleus and noradrenergic modulation of cognition. *Nat Rev Neurosci* 10: 211–223, 2009.

Satou C, **Kimura Y**, **Hirata H**, **Suster ML**, **Kawakami K**, **Higashijima S -i.** Transgenic tools to characterize neuronal properties of discrete populations of zebrafish neurons. *Development* 140: 3927–3931, 2013.

Savtchouk I, **Volterra A**. Gliotransmission: Beyond Black-and-White. *J Neurosci* 38: 14–25, 2018.

Scemes E, **Giaume C**. Astrocyte calcium waves: What they are and what they do. *Glia* 54: 716–725, 2006.

Schoonheim PJ, **Arrenberg AB**, **Del Bene F**, **Baier H**. Optogenetic Localization and Genetic Perturbation of Saccade-Generating Neurons in Zebrafish. *J. Neurosci.* (2010). doi: 10.1523/jneurosci.5193-09.2010.

Schummers J, **Yu H**, **Sur M**. Tuned responses of astrocytes and their influence on hemodynamic signals in the visual cortex. *Science (80-)* 320: 1638–1643, 2008.

Serrano A. GABAergic Network Activation of Glial Cells Underlies Hippocampal Heterosynaptic Depression. *J Neurosci* 26: 5370–5382, 2006.

Severi KE, **Portugues R**, **Marques JC**, **O'Malley DM**, **Orger MB**, **Engert F**. Neural Control and Modulation of Swimming Speed in the Larval Zebrafish. *Neuron* 83: 692–707, 2014.

Shadlen MN, **Newsome WT**. Neural Basis of a Perceptual Decision in the Parietal Cortex (Area LIP) of the Rhesus Monkey. *J Neurophysiol* 86: 1916–1936, 2017.

Shadmehr R, **Mussa-Ivaldi F**. Adaptive representation of dynamics during learning of a motor task. *J Neurosci* 14: 3208–3224, 2018.

Shi J, **Malik J**. Normalized cuts and image segmentation. *IEEE Trans Pattern Anal Mach Intell* 22: 888–905, 2000.

Shigetomi E, **Bushong EA**, **Haustein MD**, **Tong X**, **Jackson-Weaver O**, **Kracun S**, **Xu J**, **Sofroniew M V.**, **Ellisman MH**, **Khakh BS**. Imaging calcium microdomains within entire astrocyte territories and endfeet with GCaMPs expressed using adeno-associated viruses. *J Gen Physiol* 141: 633–647, 2013a.

Shigetomi E, **Bushong EA**, **Haustein MD**, **Tong X**, **Jackson-Weaver O**, **Kracun S**, **Xu J**, **Sofroniew M V.**, **Ellisman MH**, **Khakh BS**. Imaging calcium microdomains within entire astrocyte territories and endfeet with GCaMPs expressed using adeno-associated viruses. *J Gen Physiol* 141: 633–647, 2013b.

Shigetomi E, **Patel S**, **Khakh BS**. Probing the Complexities of Astrocyte Calcium Signaling. *Trends Cell Biol* 26: 300–312, 2016.

Sild M, **Van Horn MR**, **Schohl A**, **Jia D**, **Ruthazer ES**. Neural Activity-Dependent Regulation of Radial Glial Filopodial Motility Is Mediated by Glial cGMP-Dependent Protein Kinase 1 and Contributes to Synapse Maturation in the Developing Visual System. *J Neurosci* 36: 5279–5288, 2016.

Sild M, **Ruthazer ES**. Radial glia: Progenitor, pathway, and partner. *Neuroscientist* 17: 288–302, 2011.

Simard M, **Nedergaard M**. The neurobiology of glia in the context of water and ion homeostasis. *Neuroscience* 129: 877–896, 2004.

Sloan SA, **Barres BA**. Looks can be deceiving: Reconsidering the evidence for gliotransmission. *Neuron* 84: 1112–1115, 2014.

Somjen GG. Nervenkitt: Notes on the history of the concept of neuroglia. *Glia* 1: 2–9, 1988.

Steru L, **Chermat R**, **Thierry B**, **Simon P**. The tail suspension test: A new method for screening antidepressants in mice. *Psychopharmacology (Berl)* 85: 367–370, 1985.

Strauss R, **Schuster S**, **Götz KG**. Processing of artificial visual feedback in the walking fruit fly Drosophila melanogaster. [Online]. *J Exp Biol* 200: 1281–96, 1997. http://www.ncbi.nlm.nih.gov/pubmed/9172415.

Tasdemir-Yilmaz OE, **Freeman MR**. Astrocytes engage unique molecular programs to engulf pruned neuronal debris from distinct subsets of neurons. *Genes Dev* 28: 20–33, 2014.

Tay TL, **Ronneberger O**, **Ryu S**, **Nitschke R**, **Driever W**. Comprehensive catecholaminergic projectome analysis reveals single-neuron integration of zebrafish ascending and descending dopaminergic systems. *Nat Commun* 2: 171, 2011.

Tervo DGR, **Proskurin M**, **Manakov M**, **Kabra M**, **Vollmer A**, **Branson K**, **Karpova AY**. Behavioral variability through stochastic choice and its gating by anterior cingulate cortex. *Cell* 159: 21–32, 2014.

Than-Trong E, **Bally-Cuif L**. Radial glia and neural progenitors in the adult zebrafish central nervous system. *Glia* 63: 1406–1428, 2015.

Tillberg PW, **Chen F**, **Piatkevich KD**, **Zhao Y**, **Yu CC**, **English BP**, **Gao L**, **Martorell A**, **Suk HJ**, **Yoshida F**, **Degennaro EM**, **Roossien DH**, **Gong G**, **Seneviratne U**, **Tannenbaum SR**, **Desimone R**, **Cai D**, **Boyden ES**. Protein-retention expansion microscopy of cells and tissues labeled using standard fluorescent proteins and antibodies. *Nat Biotechnol* 34: 987–992, 2016.

Tsai PS, **Blinder P**, **Migliori BJ**, **Neev J**, **Jin Y**, **Squier JA**, **Kleinfeld D**. Plasma-mediated ablation: an optical tool for submicrometer surgery on neuronal and vascular systems. *Curr. Opin. Biotechnol.* 20: 90–99, 2009.

Urasaki A, **Kawakami K**. Analysis of genes and genome by the tol2-mediated gene and enhancer trap methods. *Methods Mol Biol* 546: 85–102, 2009.

Verkhratsky A, **Rodríguez JJ**, **Parpura V**. Calcium signalling in astroglia. *Mol Cell Endocrinol* 353: 45–56, 2012.

Virchow R. from the library of Helmut Kettenmann Max Delbrück Center for Molecular Medicine Berlin-Buch. *Allg Zsch Psychiat*. .

Virchow R. Phlogose und Thrombose im Gefasssystem. *Gesammelte Abhandlungen zur Wissenschaftlichen Med. Fankfurt*. .

Vladimirov N, **Mu Y**, **Kawashima T**, **Bennett D V.**, **Yang CT**, **Looger LL**, **Keller PJ**, **Freeman J**, **Ahrens MB**. Light-sheet functional imaging in fictively behaving zebrafish. *Nat Methods* 11: 883–884, 2014.

Vladimirov N, **Wang C**, **Höckendorf B**, **Pujala A**, **Tanimoto M**, **Mu Y**, **Yang CT**, **Wittenbach JD**, **Freeman J**, **Preibisch S**, **Koyama M**, **Keller PJ**, **Ahrens MB**. Brain-wide circuit interrogation at the cellular level guided by online analysis of neuronal function. *Nat Methods* 15: 1117–1125, 2018.

Volterra A, **Liaudet N**, **Savtchouk I**. Astrocyte Ca2+ signalling: An unexpected complexity. *Nat Rev Neurosci* 15: 327–335, 2014.

Walker C, **Streisinger G**. Induction of mutations by γ-rays in pregonial germ cells of zebrafish embryos. *Genetics* 103: 125–136, 1983.

Walz W. Controversy surrounding the existence of discrete functional classes of astrocytes in adult gray matter. *Glia* 31: 95–103, 2000.

Wang F, **Smith NA**, **Xu Q**, **Fujita T**, **Baba A**, **Matsuda T**, **Takano T**, **Bekar L**, **Nedergaard M**. Astrocytes modulate neural network activity by Ca 2+ -dependent uptake of extracellular K +. *Sci Signal* 5: ra26, 2012a.

Wang F, **Xu Q**, **Wang W**, **Takano T**, **Nedergaard M**. Bergmann glia modulate cerebellar Purkinje cell bistability via Ca2+-dependent K+ uptake. *Proc Natl Acad Sci* 109: 7911–7916, 2012b.

Wang HC, **Lin CC**, **Cheung R**, **Zhang-Hooks Y**, **Agarwal A**, **Ellis-Davies G**, **Rock J**, **Bergles DE**. Spontaneous Activity of Cochlear Hair Cells Triggered by Fluid Secretion Mechanism in Adjacent Support Cells. *Cell* 163: 1348–1359, 2015.

Weber B, **Barros LF**. The astrocyte: Powerhouse and recycling center. *Cold Spring Harb Perspect Biol* 7, 2015.

Weissman TA, **Riquelme PA**, **Ivic L**, **Flint AC**, **Kriegstein AR**. Calcium waves propagate through radial glial cells and modulate proliferation in the developing neocortex. *Neuron* 43: 647–661, 2004.

White RM, **Sessa A**, **Burke C**, **Bowman T**, **LeBlanc J**, **Ceol C**, **Bourque C**, **Dovey M**, **Goessling W**, **Burns CE**, **Zon LI**. Transparent Adult Zebrafish as a Tool for In Vivo Transplantation Analysis. *Cell Stem Cell* 2: 183–189, 2008.

Yanes C, **Monzon-Mayor M**, **Ghandour MS**, **De Barry J**, **Gombos G**. Radial glia and astrocytes in developing and adult telencephalon of the lizard Gallotia galloti as revealed by immunohistochemistry with anti-GFAP and anti-vimentin antibodies. *J Comp Neurol* 295: 559–568, 1990.

Zaharia M, **Chowdhury M**, **Franklin MJ**, **Shenker S**, **Stoica I**. Spark : Cluster Computing with Working Sets. *HotCloud'10 Proc. 2nd USENIX Conf. Hot Top. cloud Comput.* (2010). doi: 10.1007/s00256-009-0861-0.

Zhu P, **Fajardo O**, **Shum J**, **Zhang Schärer YP**, **Friedrich RW**. High-resolution optical control of spatiotemporal neuronal activity patterns in zebrafish using a digital micromirror device. *Nat Protoc* 7: 1410–1425, 2012.